Doctoral Thesis

A Study on Common-mode Noise and Artefact Solution for Noninvasive Biopotential Acquisition Circuits

非侵襲式生体信号取得回路における コモンモードノイズ低減手法及び アーティファクト対策に関する研究

December 2020

Minghui Chen

To my mother and my girl friend,
for their support during my life.

Contents

Contents i

List of Figures iv

List of Tables viii

Chapter 1 Introduction 1

1.1 Background 1

1.2 Non-invasive Biopotential Electrodes 3

1.3 CM Noise and artefacts 4

1.3.1 CM Noise 4

1.3.2 Artefacts 6

1.4 Related previous studies from our group 8

1.5 Contents of this thesis 9

Chapter 2 A Circuit Design that Exceeds DRL 11

2.1 Overview 11

2.2 Circuit analysis and evaluation on the influence of EBI imbalance . 13

2.2.1 Circuit analysis on a simple differential amplifying circuit . . 13

2.2.2 Circuit analysis on a DRL circuit 16

2.2.3 Circuit analysis on a pre-amplifying circuit 18

2.2.4 Circuit simulation on effect of EBI imbalance 21

2.2.5 V_{out}/V_{CM} vs. CMRR 23

2.3 Imbalance cancellation design with digiPOTs and Evaluations . . . 24

2.4 Conclusion and our contribution 29

Chapter 3 A Real Value of Our Approach: for Noncontact Biopotential Acquisition 31

3.1 Overview 31

3.2 Circuit analysis 32

3.2.1 Proposal 1: "DTC Series" 32

3.2.2 Proposal 2: "DTC Bypath" 35

3.3 Circuit simulation and results 38

3.3.1 Without the DTCs 38

3.3.2 "DTC Series" 40

3.3.3 "DTC Bypath" 41

3.3.4 Estimating the practical tunability step of the DTCs 43

3.3.5 Signal gain performance 43

3.3.6 Frequency characteristic 48

3.4 DTC design and experimental evaluations 49

3.4.1 Introduction to DTC chips and our design 49

3.4.2 Experimental evaluations 52

3.5 Conclusion and our contribution 57

Chapter 4 EBI Impedance Imbalance Monitoring Strategy 59

4.1 Overview 59

4.2 Related previous studies 60

4.3 Circuit analysis 61

4.4 Wien Bridge Oscillator 62

4.5 DTC controlling scheme in the microcomputer 65

4.6 Experimental evaluation 67

4.7 Conclusion and our contribution 67

Chapter 5 An Advanced Ideology and Application: Imbalance Cancellation based Artefact Solution 69

5.1 Overview 69

5.2 Theoretical analysis using EOG artefacts 70

5.3 Dividing the artefacts 75

5.4 EBI impedance measurement 76

5.5 Artefact monitoring with the test tone 79

5.6 Experimental verification 80

5.7 Conclusion 84

Chapter 6 Summary 86

References 90

Acknowledgements 101

Chapter 7 Publication lists 102

7.1 Paper 102

7.2 International Conference 102

7.3 Oral Presentation 103

List of Figures

1.1 Healthcare application example with BAN [2] 1

1.2 Activity recognition [5] 2

1.3 Non-invasive biopotential electrodes [16] 3

1.4 Conduction models of DM noise and CM noise [26] 5

1.5 CM noise model of biopotential acquisition circuits 6

2.1 Equivalent circuit of a simple wearable ECG 14

2.2 Fig. 2.1 for circuit calculation 14

2.3 A typical DRL circuit 16

2.4 Explanation to the principle of DRL 17

2.5 Actual DRL circuit condition 18

2.6 An acquisition circuit with pre-amplified electrodes 19

2.7 The assumed condition of our circuit simulation. The design in Fig. 2.1, Fig. 2.3 or Fig. 2.6 is employed as the biopotential acquisition circuit respectively during the simulation. 22

2.8 Simulated result of the influence of imbalance in contact resistance. No-cancellation: result of the conventional circuit in Fig. 2.1. DRL: result of the DRL circuit in Fig. 2.3. Buffer: result of the proposed design in Fig. 2.6. 22

2.9 CM equivalent circuit with the digiPOTs. (a) The circuit in Fig. 2.1 with digiPOTs installed. (b) The circuit in Fig. 2.6 with digiPOTs installed. 25

2.10 The result of comparison among the three circuits. "No-cancellation" and "DRL" in (a) and (b): the same as the result in Fig. 2.8. "DigiPOT100K" in (a): TPL0102-100 used in the circuit of Fig. 2.9 (a). "DigiPOT10K" in (b): TPL0202-10 used in the circuit of Fig. 2.9 (a). 27
2.11 The other result to show the performance of the circuit in Fig. 2.9 (b). "No-cancellation" and "DRL": the same as the result in Fig. 2.8. "DigiPOT100K-Buffer": TPL0102-100 used in the circuit of Fig. 2.9 (b). "DigiPOT10K-Buffer": TPL0202-10 used in the circuit of Fig. 2.9 (b). 28

3.1 Assumed acquisition model and conditions of circuit analysis 33
3.2 CM equivalent circuit of "DTC Series" 34
3.3 CM equivalent circuit of "DTC Bypath" 36
3.4 CM equivalent circuit without the DTCs 39
3.5 Simulated result of output voltage normalized to CM noise input for capacitance imbalance −200 pF to 200 pF (Table 3.1's condition). 39
3.6 Simulated result of output voltage normalized to CM noise for "DTC Series" under Table 3.2's condition. 41
3.7 Simulated result of output voltage normalized to CM noise for "DTC Bypath" under Table 3.3's condition. 42
3.8 Signal gain performance comfirming circuit and simulated result of the pre-amplifying circuit 45
3.9 Signal gain performance comfirming circuit and simulated result of "DTC Series" 46
3.10 Signal gain performance comfirming circuit and simulated result of "DTC Bypath" 47
3.11 Simulated result of small signal AC sweep under Table 3.4's condition. 48

3.12 RF tunable MEMS WS1040 [59] 50
3.13 BST device STPTIC-82c4 [60] 50
3.14 PSEMI SOI/SOS tuning device PE64102 [61] 51
3.15 Equivalent circuit of our originally designed DTC 52
3.16 Configuration of the evaluative board with a microcomputer 53
3.17 Evaluation circuit on a universal board. We use two sets of ceramic capacitors to simulate the EBI capacitance. The chip capacitors for constructing the DTC are soldered on the back side of the board. . 54
3.18 Noise reduction efficacy of our approach. The noise source is a 1 V, 60 Hz sine wave. The blue circled line is the CM noise output when the imbalance is forced in the capacitors emulating the EBIs; the red dotted line is the result when the imbalance is overcame by means of appropriate selection of ordinary capacitors (manually). . 55
3.19 Experimental result of noise reduction efficacy using DTCs. ADG512: 4 tunable steps, about 24 pF for each step; MAX335: 8 tunable steps, about 6 to 8 pF for each step. 56

4.1 Injection model of the test tone 62
4.2 Equivalent circuit of the injection model 63
4.3 Comparing the plot of $|V_a - V_b|$ from (4.3) and circuit simulation result of $|V_a - V_b|$ from the original circuit 63
4.4 Wien Bridge Oscillator circuit design 64
4.5 DTC controlling scheme configuration 65
4.6 Flow chart of the imbalance detection and DTC management algorithm 66
4.7 Correlation between the imbalance and the output of the injection signal 68

5.1 EOG acquisition system 71
5.2 Arrangement of electrodes 71

5.3 EOG waveform of saccades (gaze angle: 10°, 20°, 30°, 40°, 50°) . . . 72
5.4 6 subjects' EOG amplitude vs. gaze angle fitting curves 72
5.5 Electrical model of an eyeball 73
5.6 Two EOG artefacts caused by the eyelid muscles. (a) eyelid fatigue, (b) a blink after a saccade. 74
5.7 Electrode arrangement for EOG artefact comparison 74
5.8 Comparison of left and right EOG artefact 75
5.9 Equivalent circuit of the EBI impedance measurement 77
5.10 Places for impedance measurement 77
5.11 Equivalent circuit of imbalance estimation 78
5.12 Equivalent circuit and experimental scenery of artefact monitoring with the test tone 80
5.13 Test tone output change when shaking the arm 81
5.14 Test tone output change when pushing the electrode 81
5.15 Test tone output change when peeling off the electrode 82
5.16 The artefact of stretching and withdrawing of forearm and the metal electrodes 82
5.17 Test tone output voltage change when stretching and withdrawing forearm 83
5.18 Equivalent circuit of the experimental setting for verifying the imbalance cancellation based artefact solution 83

List of Tables

1.1 Difference between our work and [25] 9

2.1 The parameters of the circuit components 21
2.2 The parameters of the digiPOTs TPL0102-100 and TPL0202-10 . . 25

3.1 Parameters of circuit components in Fig. 3.4 40
3.2 Parameters of the simulated circuit components for "DTC series" . 41
3.3 The parameters of the simulated circuit components for "DTC Bypath" 42
3.4 Parameters of the circuit components for the AC sweep 49
3.5 Parameters of ADG512 and MAX335EUG+ 56

5.1 Measured impedance value 76
5.2 Measured imbalance 79
5.3 Experimental results of the verification 84

Chapter 1

Introduction

1.1 Background

As the aging society problem draws great attention, the sensing technology of biosignals has advanced tremendously over the years. Typical biosignals include biopotential signals like electrocardiogram (ECG), electroencephalogram (EEG) or electrooculogram (EOG). As an famous example, the body area network (BAN) [1–3] with wearable sensing technologies can collect these signals as vital data for health-state monitoring, which is considered as an emerging solution to soaring healthcare costs and shortages of medical resources.

The potential of biosignals is still to be exploited when sensing technologies

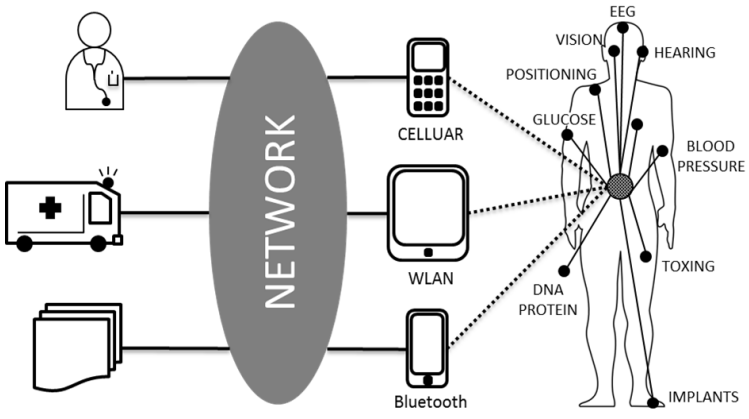

Fig. 1.1. Healthcare application example with BAN [2]

advance further. In addition to medical treatment and healthcare, they could also

be considered as an irreplaceable interface between human body and machines. In the literature, applications like activity recognition [4,5], driving assistance [6,7] or human computer interface [8–10] were mentioned by researchers. Fig. 1.2 shows the concept of activity recognition, which includes recording and analysing the vital data through biosignals, figuring out the activity pattern of users, and then apply the analyzed data for interaction between the human body and machines. The brain-machine interfaces also attract a lot of attentions. Recently Elon Musk et al. had demonstrated their progress on an invasive brain-machine interfaces, which successfully read the brain activity of a pig [15]. In their interface, thousands of invasive probes were employed. It is possible that this kind of brain activity monitoring to be accomplished by new non-invasive detecting measures, because the EEG basically contains same information as the neural spike activity.

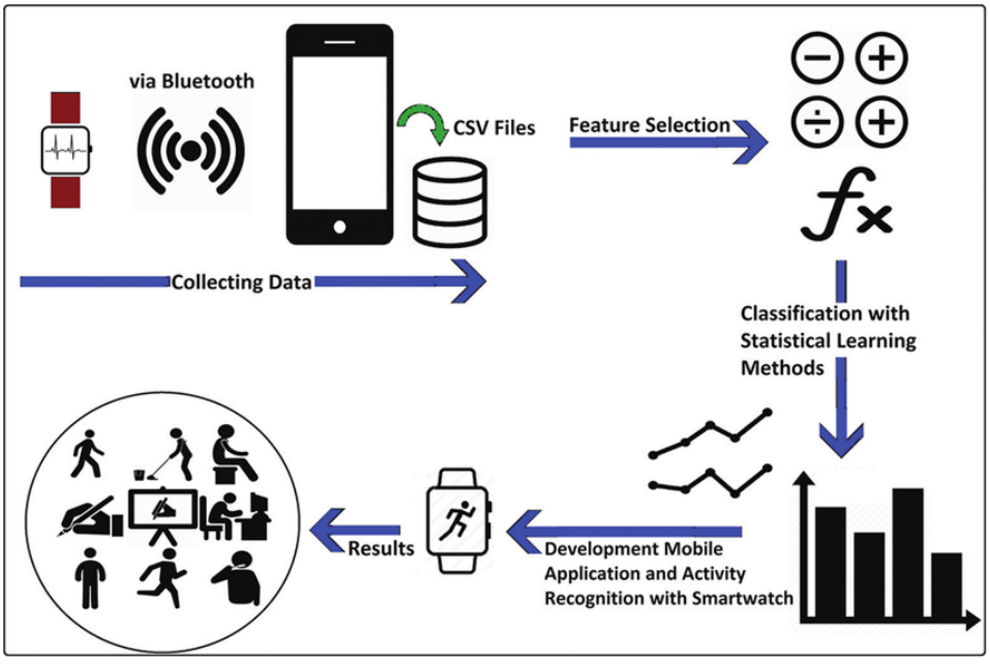

Fig. 1.2. Activity recognition [5]

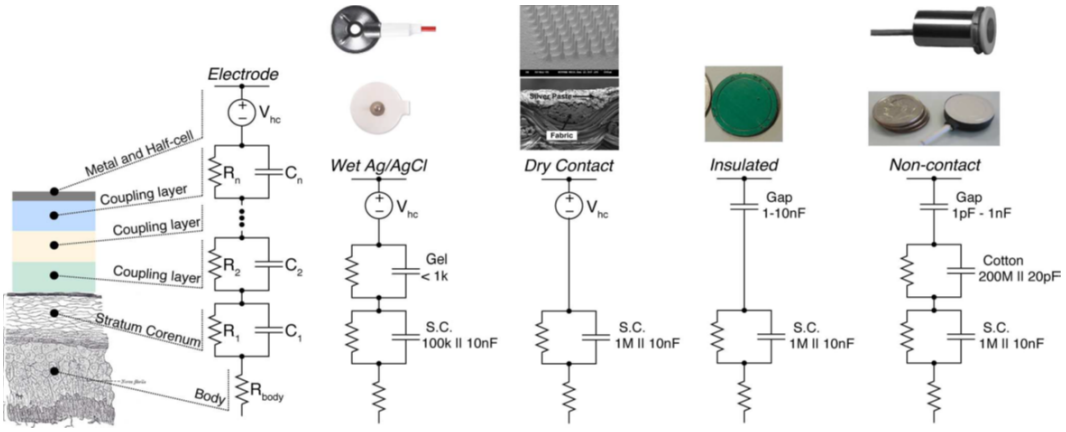

Fig. 1.3. Non-invasive biopotential electrodes [16]

1.2 Non-invasive Biopotential Electrodes

There are mainly three different types (the insulated electrode can be regarded as one type of noncontact electrode) of non-invasive electrodes [16]. Fig. 1.3 shows the types and electrical couplings of them. Wet electrode is the most common type for both clinical and research applications. A typical wet electrode consists of a silver-silver chloride metal that is surrounded by a wet or solid hydrogel, containing chloride. The primary drawbacks with wet electrodes are limited lifetime, discomfort and skin irritations. Wet electrodes degrade as the moisture content evaporates, limiting its useful lifetime to several hours or at most a few days.

Dry contact electrodes operate without the use of wet/gel coupling media. The metal in the electrode directly contacts the skin to couple biopotential signals. However, dry contact electrodes still rely on some degree of moisture. Performance of a dry contact electrode usually increases over time as more moisture permeates the skin-electrode interface.

The final type of electrodes, noncontact, can be thought as a special case of dry electrodes. The noncontact electrode was introduced by Lopez and Richardson in

1967 [17] and further developed in the last decade [11–14]. Noncontact electrodes have certain advantages in biosignal acquisition because they do not need direct skin contact, and they can be integrated in objects like beds or cars for long term biosignal recording. They operate not only without gel, but also through an insulation layer such as clothing. Therefore, they are also called capacitive electrodes. The coupling capacitance can range on the order of tens or hundreds of picofarad [24]. Obtaining acceptable signals requires the use of high input impedance active electrodes. There are also some other technologies that can achieve noncontact sensing of biosignals, like using the Doppler Cardiogram [18] or a radar [19–22]. Recently, Taylor et al. [23] provided a noncontact approach to detect COVID-19.

Impedance at the electrode-body interface (EBI), especially noncontact electrodes, are highly sensitive to environmental conditions such as humidity and the exact insulating material. This property makes the noncontact electrodes induce much more noise than wet electrodes, because the imbalance of the electrode-body interface impedances allows the common-mode (CM) noise converting into a differential-mode (DM) interference voltage [25].

1.3 CM Noise and artefacts

1.3.1 CM Noise

An important task is to classify noises and artefacts in each biopotential signal. Good classification of them helps clarifying the task and aim of our work. Firstly, we give a brief explanation about the DM noise and CM noise. The conduction models of DM noise and CM noise are shown in Fig. 1.4. The DM noise is conducted on the signal (VCC) line and GND line in the opposite direction to each other, while the CM noise is conducted on all lines in the same direction. This

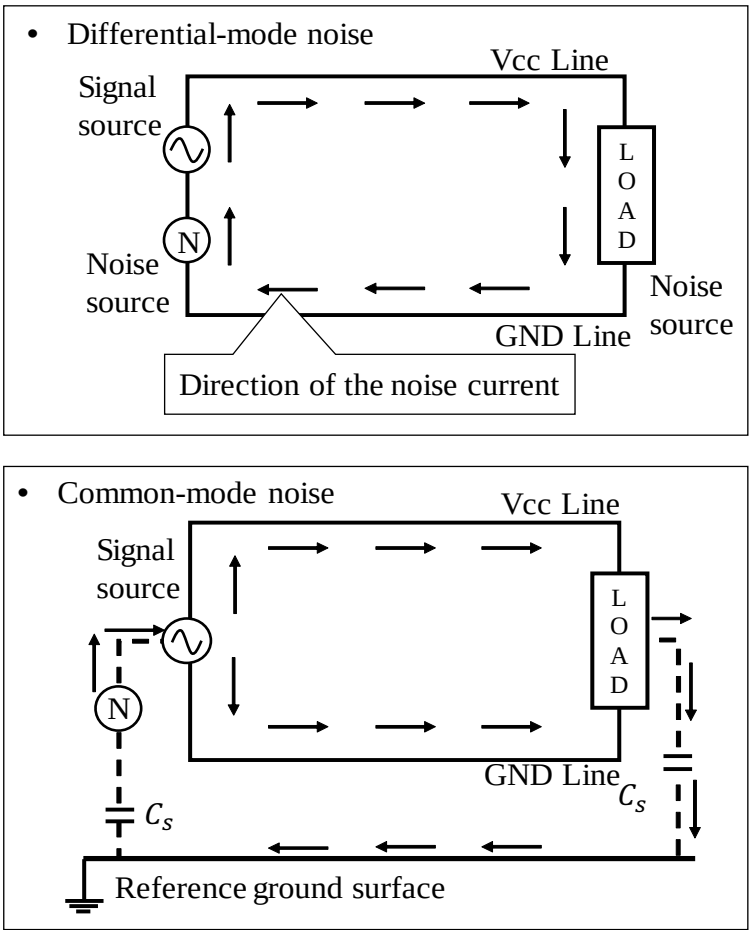

Fig. 1.4. Conduction models of DM noise and CM noise [26]

is because the noise current of CM noise is conducted because of the existence of the stray capacitance. For biopotential acquisition circuit, the stray capacitance always exists between the signal ground and the earth ground, allowing the CM noise source conduct through the whole sensing system. To be exact, the CM noise mentioned in this work always refer to the noise source is between the human body surface and the earth ground, as is shown in Fig. 1.5.

Interferences like the power line noise, the electromagnetic interference (EMI), a wireless power transfer system [28] or any voltage source between the human body surface and the earth ground can be equivalated to the model in Fig. 1.5. The CM noise is a main extrinsic interference to EOG, ECG, EEG and other biopotential

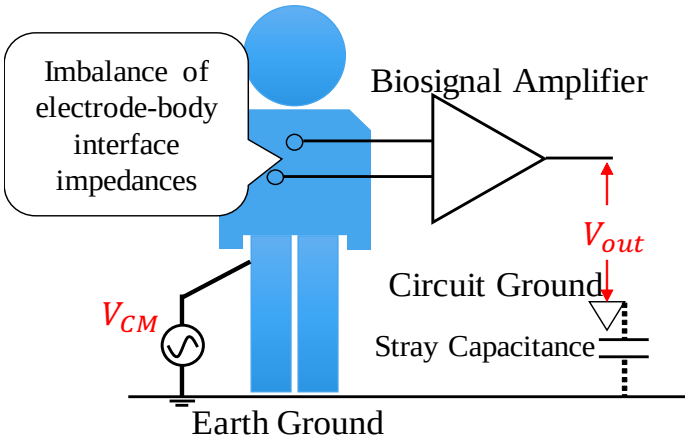

Fig. 1.5. CM noise model of biopotential acquisition circuits

signals. Liao et al. [28] explained to what extent an imbalance in the impedances of EBI could induce CM noise to the circuit. In conclusion, CM noise sources can severely interfere the detection progress.

The CM equivalent circuit for biopotential acquisition is different from equivalent circuit of an antenna. The stray capacitance between the circuit ground and the earth ground allows the CM current flow through the whole acquisition system like is shown in Fig. 1.4. Even if we can eliminate the reactance component like an antenna, the CM current still exists and cause the CM noise. The stray capacitance can hardly be eliminated, while technologies like an active shield [27] can be used to reduce it at the analog-front-end of a biopotential acquisition circuit.

1.3.2 Artefacts

Secondly, we give an overview of the artefacts in EOG, ECG and EEG, such that the concept of an artefact is clarified. The EOG artefacts, or sometimes called as ocular artefacts, is usually accompanied with regular eye movements. Like eyelid fatigue [7], a blink during a saccade [29], or compensatory movements [30], EOG

artefacts basically have large personal difference, and existing solutions are mainly based on adaptive signal processing algorithms.

ECG artefacts are exhaustively explained by researchers because it is commonly used in medical diagnosis [31, 32]. DC (direct current) drifts and motion artefacts are two kinds of significant ECG artefacts that affect the acquisition progress. Some researchers also call the CM noise as one kind of ECG artefact. But in this thesis, we separate the "noises" that always exist from the "artefacts" that are usually caused by artificial reasons or human factors.

EEG artefacts are also widely discussed in the literature. Usually they are sorted into ocular artefacts, muscle artefacts and cardiac artefacts [33]. The ocular artefact is generated by eye blinks and eye movements. Because that EEG voltage is normally in tens of microvolts order, ocular artefacts pose a serious problem to EEG acquisition process. Muscle artefacts and cardio artefacts are caused by muscle activity and ECG respectively. Hence even though EEG electrodes are pasted on the head or ear [34], these potential changes that caused by the other parts of the human body (eye, muscle and heart) can be picked up by the EEG electrodes.

Signal processing methods using algorithms like wavelet transformation [35] are often mentioned as solutions to the artefact problem, but the waveform of the artefacts distributes in wide frequency and usually has unpredictable statistical characteristics. Large differences across subjects is another challenge. In our work, to take measures at the analog circuit part of the acquisition system is the main idea. Even though the artefacts are unpredictable, better sensing scheme and circuit design can help reducing or cancelling the noise output caused by the artefacts.

1.4 Related previous studies from our group

There are some previous studies from our group related with contents of this thesis. In [36], the authors discussed the ECG circuit structure in the HBC (human body communication) based wearable ECG for removing the CM noise when employing noncontact capacitive coupling electrodes. They have shown that the authors' proposed circuit structure with the third electrode directly connected to signal ground can provide an effect on CM noise reduction similar to the usual drive-right-leg circuit, and a sufficiently good acquisition performance of ECG signals. This principle is also strongly connected with the DRL circuit [36] because they share the same principle of driving down the effective impedance of the whole biopotential acquisition circuit. Details about this technology will be discussed in Chapter 2.

In [25], Noro et al. proposed a technology of using the cadmium sulphide (CdS) like a rheostat to cancel the imbalance in the impedance of two sensing electrodes to reject the CM noise. This idea is quite attractive but the CdS has some problems in its adjustable range and resolution, which makes it limited for applications. In Chapter 2, we have combined the idea of driving down the CM voltage and compensating the imbalance in contact resistance, and provide a novel design of biosignal acquisition circuit. A comparison was quantitatively made among a conventional biosignal acquisition circuit (a simple differential amplifier), the DRL circuit and our design. With circuit calculations and computer simulation, we quantitatively show how our approach performs in reducing the CM noise. We conducted circuit simulations for evaluation and the result indicated that our design can work better than the DRL circuit in reducing the interference of CM noise. The differeces between our work and [25] is summarized into Table 1.1. A part of our work could be considered as an expansion of [25], like solving the remained problem about comparing to the DRL and detecting the imbalance with a

better approach. Bringing in new technologies and applying this idea to noncontact electrodes are also novelties of our work.

Table 1.1. Difference between our work and [25]

	Noro et al. 2017 [25]	This wok
Ground electrode usage	No	Yes
Pre-amplifying electrode	No	Yes
DRL comparison	No	Yes
Tunable circuit element	CdS	DigiPOT/DTC
Imbalance detection	Conventional approach	Using test tone
For noncontact electrodes	No	Yes

1.5 Contents of this thesis

In this study, a core idea runs through all our works: EBI impedance imbalance cancellation-based CM noise rejection for biopotential acquisition circuits. We propose circuit designs that employ actual circuit elements, perform simulations and circuit analysis to show their effectiveness in theory. We make a comparison with the most popular conventional solution, i. e., the DRL circuit, under a conventionally recognized condition, and analyze their superiority or inferiority quantitatively. We consider about both contact and noncontact biopotential acquisition circuits, point out the difference of them in EBI impedance imbalance cancellation, and provide different options due to actual needs.

In order to detect and monitor the imbalance change at the EBI, we proposed a novel method to accomplish this job using a microcomputer and an injection signal. The injection signal is produced with an originally designed Wien Bridge Oscillator in the circuit board.

Except for the external CM interference voltage from outside the acquisition circuit, we investigate the relation between the imbalance change at EBI and the artefacts. Because that some types of artefacts have direct relation with EBI

impedance change, our EBI impedance imbalance cancellation can reduce noise output caused by them.

Chapter 1 is the introduction to this thesis.

Chapter 2 discusses EBI impedance imbalance cancellation-based CM noise rejection for contact biopotential acquisition circuits. Circuit analyzation and simulation evaluations were performed to make a comparison among three different circuits. Through this comparison, we propose a circuit design that can exceed the DRL circuit.

Chapter 3 is about EBI impedance imbalance cancellation-based CM noise rejection for noncontact biopotential acquisition circuit. Circuit analyzation and simulation evaluations were also performed, while this time we proposed two different circuit designs at the first place. After that, we chose the one with better performance, build an evaluative circuit on a board, and do experimental evaluations on it to evaluate its efficacy.

Chapter 4 proposes an EBI impedance imbalance monitoring method. Circuit analysis was performed to explain the mechanism. Implementation of our approach was also conducted utilizing a circuit board and a microcomputer. Experiments are performed to verify its effectiveness.

Chapter 5 discusses about the relation between the EBI impedance and a couple of artefacts. Theoretically we analyze why they could be considered as a part of CM noise source and reduce the total Common-Mode Rejection Ratio (CMRR) of the biopotential acquisition circuit. Several experiments are performed to verify our idea. Based on the fact we mentioned, a novel idea about rejecting the artefacts through EBI imbalance cancellation is proposed, and its potential in rejecting specific types of artefacts was shown with experimental results.

Chapter 6 is a summary of the thesis.

Chapter 2

A Circuit Design that Exceeds DRL

2.1 Overview

In this chapter, we propose a novel design of biopotential acquisition circuit with contact electrodes and make a comparison with the DRL circuit on CM noise rejection performance. The performance of our design can exceed the DRL, proving the significance of the EBI imbalance cancellation technology.

Contact biopotential acquisition circuit has one certain property about its change in EBI impedance. Because of the direct contact to the skin, the resistance component is dominant at the EBI. In Chapter 1, we have introduced the conduction model of wet and dry contact electrodes. There are also many other previous studies that investigated the impedance change of contact EBI. T. Degen et al. [53] showed that when a sinusoidal force is applied to the electrode, the measurement reveals a strong relation between the resistance change and the applied force. Talhouet et al. [54] investigated the resistance change caused by scotch tape skin stripping, revealing that linear resistance change happens when the stratum corneum is peeled. These two previous studies proved that for contact electrodes, a linearly tunable resistor, like a rheostat or digital potentiometer (DigiPOT), can be used to cancel the resistance change, such that the CM noise output is suppressed. Another property of contact electrode is that frequency change brings less impedance change than noncontact ones.

DRL circuit is a conventional solution for CM noise during ECG acquisition. It can drive down the CM noise by means of reducing the effective impedance of the acquisition circuit. Further application of DRL, like using the seat as a right leg electrode to realize the Driven-Seat-Ground was proposed in [56] by Kim et al. However, the DRL technology has certain problem with its stability. Besides, even DRL technology does not always provide enough improvement in CMRR when noncontact electrodes are employed. Because that DRL circuit is a popular choice for medical applications, a novel CM noise reduction design which exceeds its performance could offer an innovative solution.

Pre-amplifying technology, or sometimes called as active electrode technology, is a common measure to improve CMRR of biopotential amplifiers nowadays. It uses two or more buffers, i. e., voltage followers, at the analog-front-end of acquisition circuit to insure high input impedance of the amplifier. In order to make a fair comparison with the DRL circuit, we will show that it is necessary to employ pre-amplified electrodes in our imbalance cacelling circuit.

We combine the idea of driving down the CM voltage with buffers (like how DRL circuit works) and cancelling imbalance of EBI resistances using DigiPOTs, such that we can provide a novel design of biopotential acquisition circuit. After comparing three conventional CM noise reduction technologies for theoretical analysis, we let the DRL compare with our imbalance cancelling design. Theoretically, we show how our approach performs in reducing the CM noise. We conduct circuit simulations for evaluation and the result indicates that our design can work better than the DRL circuit in reducing the interference of CM noise.

2.2 Circuit analysis and evaluation on the influence of EBI imbalance

2.2.1 Circuit analysis on a simple differential amplifying circuit

At this part, we analyze three circuits and evaluate how much noise the CM voltage will cause when there is an imbalance in electrode contact resistance. The circuit analyzations lead out the purpose of our design: to propose a circuit that can exceed the performance of the DRL, by means of combining EBI imbalance cancellation and pre-amplifying technology.

Fig. 2.1 shows a simple CM equivalent circuit of the wearable ECG. It has two sensing electrodes and one ground electrode. The ECG signals are acquired from the two sensing electrodes, and then differentially amplified with an operational amplifier (OP-AMP). The interference voltage V_{CM} is between the human body and the earth ground. The impedance of the two sensing electrodes are denoted as Z_{ea} or Z_{eb} respectively. Usually they are unbalanced due to the different attachment conditions. In addition, the impedance between the human body and the ground is denoted as Z_{eg}.

For the convenience of doing some circuit calculations on this circuit, we denote some notes and voltages, such that Fig. 2.1 can be redrawn as Fig. 2.2. In the circuit of Fig. 2.2, we can write down the current flow at the three notes denoted with circled numbers in this figure. By the Kirchhoff's Current Law, we can write down the current flow at note 1 (the negative input of amplifier) as

$$\frac{V_{in} - V_1}{Z_{ea} + R_1} + \frac{V_{out1} - V_1}{R_2} = 0 \tag{2.1}$$

V_{in} is the CM input voltage to the signal ground (circuit ground). For note 2 (the positive input of the amplifier), we can write down the current flow as

$$\frac{V_{in} - V_1}{Z_{eb} + R_1} = \frac{V_1 - 0}{R_2} \tag{2.2}$$

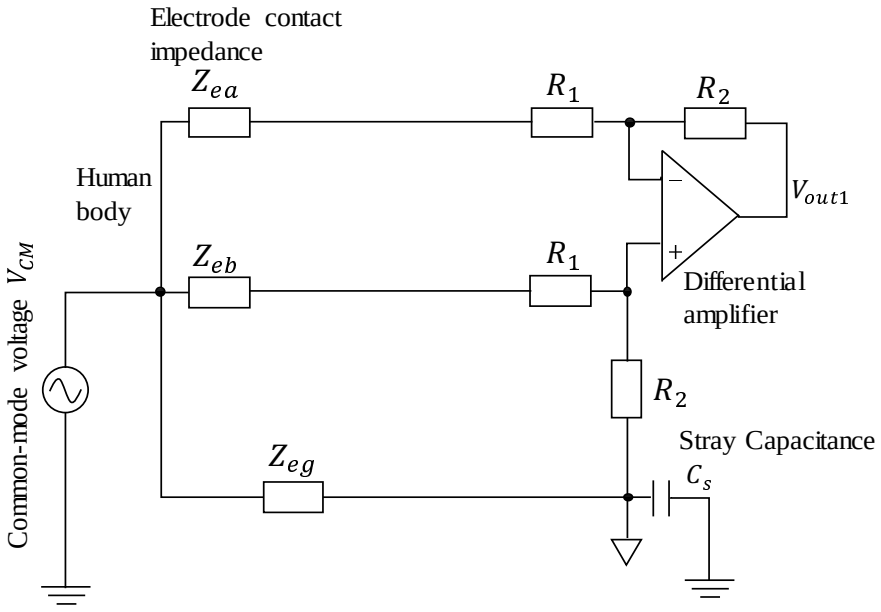

Fig. 2.1. Equivalent circuit of a simple wearable ECG

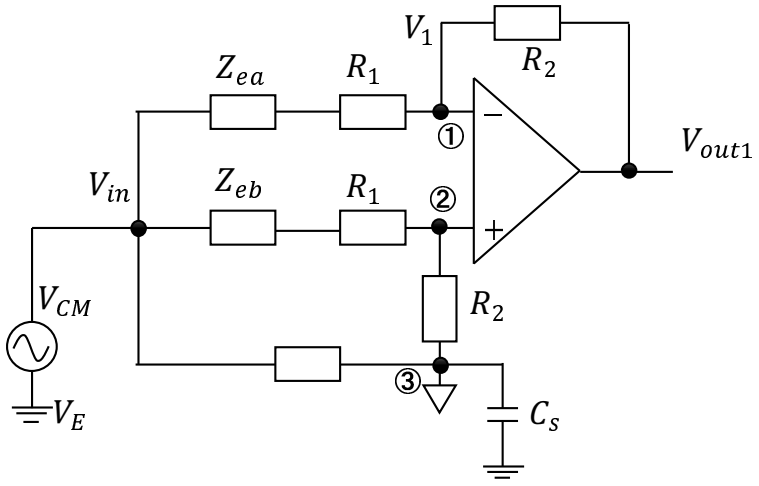

Fig. 2.2. Fig. 2.1 for circuit calculation

For note 3, at the signal ground of the acquisition circuit, we can write down the current flow as

$$\frac{V_{in}-0}{Z_{eg}}+\frac{V_1-0}{R_2}=(0-V_E)j\omega C_s \tag{2.3}$$

Besides, we also have

$$V_{in} - V_E = V_{CM} \tag{2.4}$$

where V_E is the potential of the earth ground in refer to the circuit ground. With some transformation, (2.2) can be written as

$$V_{in} = V_1(\frac{Z_{eb} + R_1}{R_2} + 1) \tag{2.5}$$

And (2.3) can be transformed to

$$V_{in} = \frac{j\omega C Z_{eg} V_{CM} - \frac{Z_{eg}}{R_2} V_1}{1 + j\omega C Z_{eg}} \tag{2.6}$$

By combining (2.5) and (2.6), V_{in} is eliminated, and we can get

$$V_1 = \frac{R_2 j\omega C Z_{eg} V_{CM}}{(Z_{eb} + R_1 + R_2)(1 + j\omega C Z_{eg}) + Z_{eg}} \tag{2.7}$$

On the other hand, the relation between V_1 and V_{out1} can be derived by combining (2.1) and (2.2), which is

$$V_{out1}(Z_{eb} + R_1) = V_1(Z_{ea} - Z_{eb}) \tag{2.8}$$

By bring (2.8) into (2.7), V_{out1} divided by V_{CM} can be written as

$$\frac{V_{out1}}{V_{CM}} = \frac{j\omega C_s R_2 Z_{eg}(Z_{ea} - Z_{eb})}{\alpha + \beta + \gamma} \tag{2.9}$$

where

$$\alpha = (Z_{ea} + Z_{eb} + 2R_1)Z_{eg} \tag{2.10}$$

$$\beta = (Z_{ea} + R_1)(Z_{eb} + R_1 + R_2) \tag{2.11}$$

$$\gamma = j\omega C_s(Z_{ea} + R_1)(Z_{eb} + R_1 + R_2)Z_{eg} \tag{2.12}$$

From (2.9) we can see that if the imbalance between the two sensing electrodes is cancelled, the CM voltage V_{CM} could not be converted into DM output voltage. This fact happens to all differential amplifying circuits, as the stray capacitance C_s always exists. The problem we would like to point out is that the system in Fig. 2.1 receives more influence from the imbalance between Z_{ea} and Z_{eb} than the other designs we are about to mention. We will show this problem quantitatively later in this chapter.

2.2.2 Circuit analysis on a DRL circuit

The second circuit that we use for this comparison is a typical DRL Circuit shown in Fig. 2.3. The mechanism of the DRL Circuit [55] is well-known and Fig.

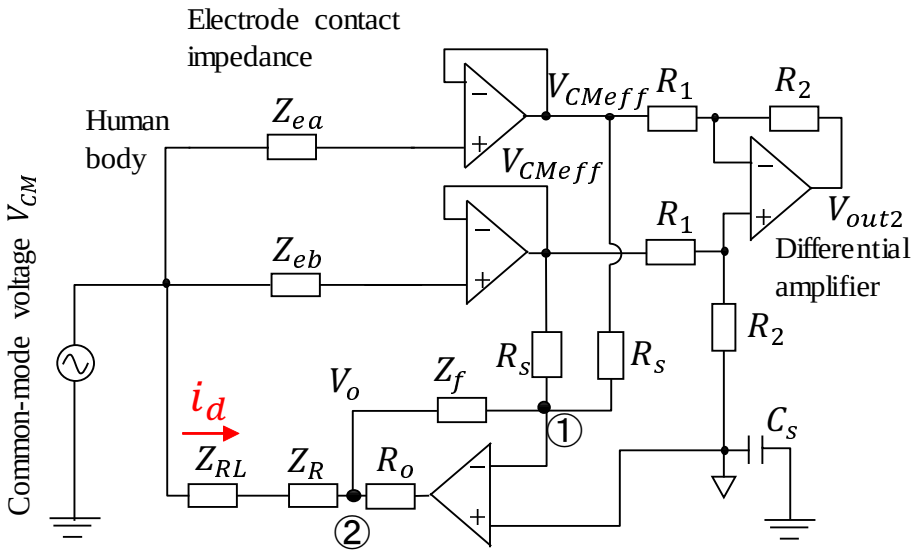

Fig. 2.3. A typical DRL circuit

2.3 could be considered as using the DRL technology in the same circumstances as Fig. 2.1. At this part we also do some calculations on this circuit. In the circuit of Fig. 2.3, again we apply the Kirchhoff's Circuit Laws. Assuming that the effective CM voltage at the output of the buffer are the same value (it is also applicable when they are not the same), we can write the current flow at note 1, denoted in the figure by a circled 1, as the following equation

$$\frac{2(V_{CMeff} - 0)}{R_s} = \frac{0 - V_o}{R_f} \tag{2.13}$$

For the note 2 denoted in Fig. 2.3, we can write the voltage as

$$V_{CMeff} - i_d(Z_{RL} + Z_R) = V_o \tag{2.14}$$

where i_d is the current flowing into the DRL part. In this calculation, we used an approximate condition that the current flow in a DRL circuit is mainly at the

DRL part. This is because the input impedance at the sensing electrode part are far larger, insured by the two buffers in front of the two sensing electrodes. From (2.13) and (2.14), we can get

$$V_{CMeff} = \frac{(Z_{RL} + Z_R)}{(1 + 2\frac{R_f}{R_s})} i_d \tag{2.15}$$

This equation reveals that the DRL part works by driving down the effective impedance of the whole biopotential acquisition circuit, because the CM noise current flow can be drawn as a simple model shown in Fig. 2.4, where Z_S stands for the stay impedance including C_S, which is the impedance that serially connected with the effective impedance of the acquisition part Z_{eff}. DRL circuit drives down the value of Z_{eff} such that less voltage of effective CM noise V_{CMeff} is superimposed on the acquisition part.

It should be noticed that the performance of the DRL circuit depends on the

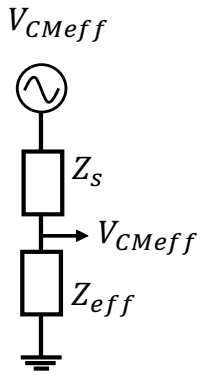

Fig. 2.4. Explanation to the principle of DRL

value of impedances at the feedback part (Z_R and Z_f). This fact could be derived from (2.15). In our simulated circuit, Z_R is 10 kΩ and Z_f is 1 MΩ, which is a usual combination for actual use. Asides, the stability of DRL is always a problem. Fig. 2.5 shows one kind of actual condition for a DRL circuit. Because of the stay capacitance caused by the cable and the capacitance at the electrode coupling part, feedback could change largely when frequency changes. In this work, we

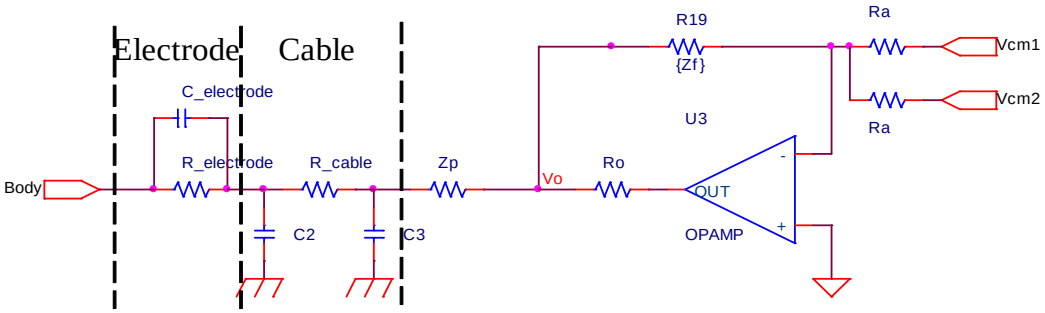

Fig. 2.5. Actual DRL circuit condition

assume that the DRL circuit for comparison always work stably, meaning that the capacitances at the electrode part and the cable part do not affect the results.

2.2.3 Circuit analysis on a pre-amplifying circuit

In the overview, we have given a brief introduction about the pre-amplifying technology. A famous application is the instrumentation amplifier (INA) [57], which connects the pre-amplified electrode with the differential amplifier, not only increasing the input impedance, but also improving the gain of it. The third circuit with pre-amplifying for our comparison is the design shown in Fig. 2.6. Because that DRL circuit also utilized two buffers at the front end, it is important to figure out how much this design helps in a DRL circuit quantitatively. In this circuit, we use two OP-AMPs as buffers to reduce the CM noise basing on the circuit in Fig. 2.1. The two OP-AMPs are considered to be non-ideal because if they are, the currents i_{b1} and i_{b2} become zero and the CM noise would not affect this circuit. Due to that the input resistance of an OP-AMP could be as large as $10^9 \sim 10^{12}$ Ω, the currents i_{b1} and i_{b2} in Fig. 2.6 are approximately the same. Besides, the input offset voltages of the buffers are supposed to be very low such that the input and output voltages of them can be seen as equal. Under these assumed preconditions, we also denote some notes in this circuit and write down

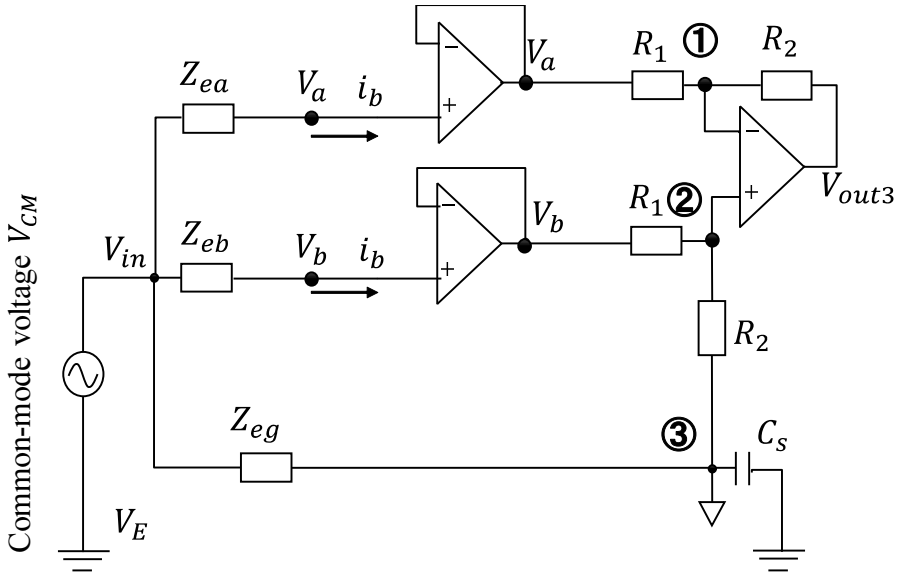

Fig. 2.6. An acquisition circuit with pre-amplified electrodes

the current flows according to Kirchhoff's Current Law.

Let $i_b = i_{b1} = i_{b2}$, at the notes denoted as 1, 2 and 3, we have the following equations

$$\frac{V_a - V_1}{R_1} + \frac{V_{out3} - V_1}{R_2} = 0 \tag{2.16}$$

$$\frac{V_b - V_1}{R_1} = \frac{V_1 - 0}{R_2} \tag{2.17}$$

$$\frac{V_1 - 0}{R_2} + \frac{V_{in} - 0}{Z_{eg}} = (0 - V_E)j\omega C_s \tag{2.18}$$

Asides, according to Ohm's Law we have

$$V_{in} - V_a = i_b Z_{ea} \tag{2.19}$$

$$V_{in} - V_b = i_b Z_{eb} \tag{2.20}$$

Additionally, it is clearly that

$$V_{in} - V_E = V_{CM} \tag{2.21}$$

Bring (2.21) into (2.18), we can get

$$V_{in} = \frac{j\omega C_s Z_{eg} V_{CM} - \frac{Z_{eg}}{R_2} V_1}{1 + j\omega C_s Z_{eg}} \tag{2.22}$$

And we can get the following equation by bringing (2.20) into (2.17)

$$V_{in} - i_b Z_{eb} = V_1(\frac{R_1}{R_2} + 1) \tag{2.23}$$

Using (2.22) and (2.23), we can get

$$V_1 = \frac{j\omega C_s Z_{eg} R_2 V_{CM} - i_b R_2 Z_{eb}(1 + j\omega C_s Z_{eg})}{(1 + j\omega C_s Z_{eg})(R_1 + R_2) + Z_{eg}} \tag{2.24}$$

Bring (2.19) into (2.16), there is

$$\frac{V_{in} - i_b Z_{ea}}{R_1} + \frac{V_{out3}}{R_2} = V_1(\frac{1}{R_1} + \frac{1}{R_2}) \tag{2.25}$$

Use (2.17) to eliminate V_{in} in (2.25), with some transformation, we can get

$$V_{out3} = i_b \frac{R_2}{R_1}(Z_{ea} - Z_{eb}) \tag{2.26}$$

(2.26) indicates that if we use proper OP-AMPs with high input resistance which could reduce the i_b, then V_{out3} will be reduced as well (of course parameters like the offset voltage are also critical for actual circuit design issue). From (2.24) and (2.26) we can see that if we solve V_1 and i_b, we can get the relation between V_{out3} and V_{CM}. Use (2.22) and the following equation

$$i_b = \frac{V_{in}}{Z_{ea} + Z_{in}} \tag{2.27}$$

which comes from using the ohm's law at the input of the buffer, we can eliminate V_1, i_b and V_{in}. Finally, V_{out3} divided by V_{CM} in Fig. 2.6 can be written as

$$\frac{V_{out3}}{V_{CM}} = \frac{j\omega C_s R_1 Z_{eg}(R_1 + R_2)(Z_{eg} + Z_{in})(Z_{ea} - Z_{eb})}{R_2(Z_{ea} + Z_{in})\Pi} \tag{2.28}$$

where

$$\Pi = (1 + j\omega C_s Z_{eg})(R_1 + R_2)(Z_{eg} + Z_{in}) + Z_{eg}(Z_{ea} - Z_{eb} + Z_{in}) \tag{2.29}$$

2.2.4 Circuit simulation on effect of EBI imbalance

The evaluation was conducted using SPICE (Simulation Program with Integrated Circuit Emphasis). Fig.4 shows the assumed condition of our circuit simulation. It is an one-channel EOG acquisition circuit with three electrodes (two biopotential electrodes and one earth/Right-Leg electrode) coupled with the CM noise. The AC main operating at 60 Hz is assumed to be the primary CM voltage source V_{CM}. It couples to the human body through coupling capacitor C_1. Three electrodes are attached to human body same as Fig. 2.1, Fig. 2.3 or Fig. 2.6. Capacitance C_s is coupled between earth ground and the ground of the biopotential acquisition circuit. Primary imbalance between the Z_{ea} and Z_{eb} is assumed to be a difference in resistance. The parameters of the circuit components are shown in Table 2.1. The OP-AMPs used as buffers are all simulated with the model of OP-07 made by ANALOG DEVICE, which has high CM input resistance and very low offset voltage. The OP-AMPs for the DRL feedback and the differential amplifier are ideal because their influences are not our concern in this evaluation.

The simulated result is shown in Fig. 2.8. The horizontal axis is the imbalance

Table 2.1. The parameters of the circuit components

Parameter	Value	Parameter	Value
Frequency	60 Hz	V_{CM}	20 V V_{pp}
Z_{ea}	1 Ω ∼ 200 kΩ	R_1	10 kΩ
Z_{eb}	100 kΩ	R_2	10 MΩ
Z_{eg}	10 kΩ	R_o	10 kΩ
Z_f	1 MΩ	R_s	10 kΩ
Z_{RL}	100 kΩ	C_s	200 pF
C_1	100 pF		

and the vertical axis is the ratio of V_{out} and V_{CM} in decibel (dB). Calculation of the imbalance is given by

$$Imbalance = \frac{\delta R}{R} \times 100\% \tag{2.30}$$

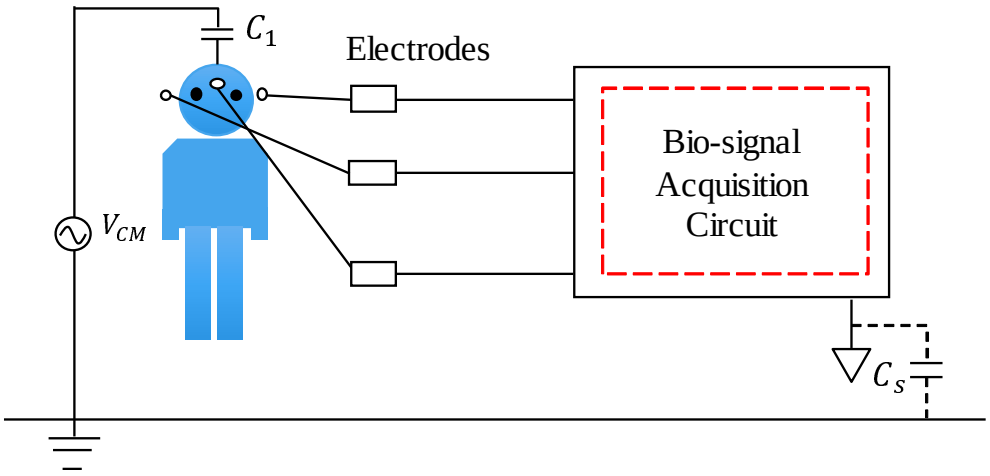

Fig. 2.7. The assumed condition of our circuit simulation. The design in Fig. 2.1, Fig. 2.3 or Fig. 2.6 is employed as the biopotential acquisition circuit respectively during the simulation.

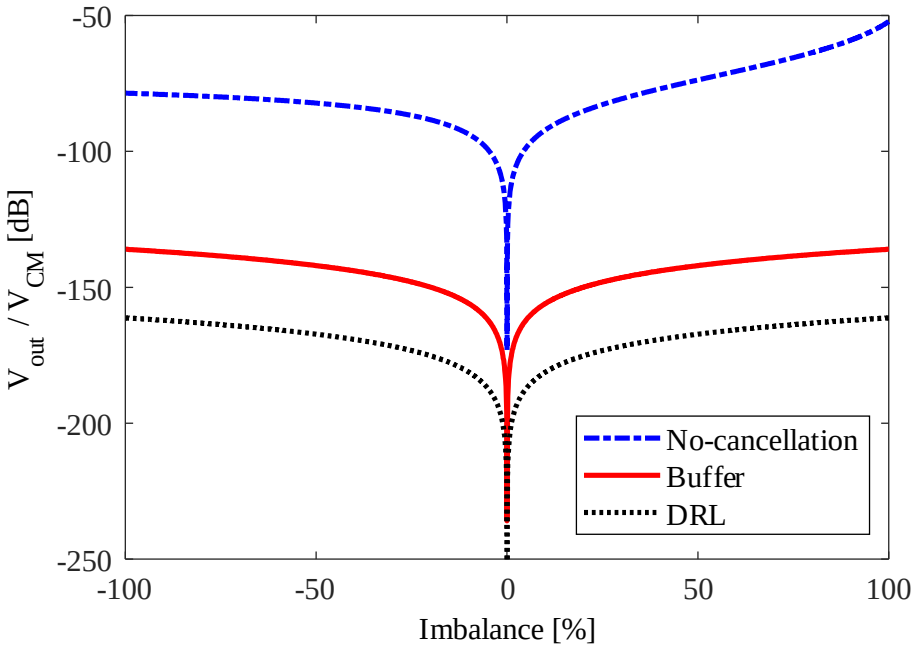

Fig. 2.8. Simulated result of the influence of imbalance in contact resistance. No-cancellation: result of the conventional circuit in Fig. 2.1. DRL: result of the DRL circuit in Fig. 2.3. Buffer: result of the proposed design in Fig. 2.6.

For example, if the Z_{ea} is 110 kΩ and the Z_{eb} is 100 kΩ, then the imbalance is

10%. We can see that the V_{out}/V_{CM} can increase to as high as -50 dB when there is no proper cancelling measure. This fact implies that the system in Fig. 2.1 (simple differential amplifier) can hardly work when there is an imbalance bigger than about 2% between Z_{ea} and Z_{eb}. By comparing the three plots in Fig. 2.8, it is obvious that the DRL circuit receives least interference and our design is better than the one in Fig. 2.1. The reason is that the buffers in Fig. 2.3 and Fig. 2.6 reduces the CM currents flow through the acquisition circuit, and the negative feedback in DRL drives down the effective impedance of the whole acquisition circuit better than a single resistance Z_{eg} like in Fig. 2.6. In addition, the CM noise level becomes extremely low when the imbalance is near to zero.

In actual circuit conditions, there is a possibility that the type of OP-AMP used at the feedback part of the DRL circuit could affect the performance of DRL. However, because that the environment of DRL operation is quite stable, type of OP-AMP employed for the DRL feedback part does not affect the simulation result.

2.2.5 V_{out}/V_{CM} vs. CMRR

V_{out}/V_{CM} is a simple parameter we use in this work to evaluate how much noise could be converted from an external interference CM voltage. V_{out} is with respect to the circuit ground and V_{CM} is with respect to the earth ground. It can be converted to the CMRR by using the following equations:

$$CMRR = 20log(\frac{A_{DM}}{A_{CM}}) \tag{2.31}$$

In our simulation conditions, the effective CM voltage (with respect to the circuit ground) V_{CMeff} and V_{CM} has the following relation (when V_{CM} is 1 V at 60 Hz):

$$20log(\frac{V_{CMeff}}{V_{CM}}) \approx -6 \; to \; -15 \text{ dB} \tag{2.32}$$

Moreover, the common mode gain A_{CM} in CMRR can be written as:

$$A_{CM} = \frac{V_{out}}{V_{CMeff}} \tag{2.33}$$

Differential mode gain A_{DM} is normally a fixed value 60 dB, which almost does not change in the simulation due to the high input impedance. Thus, we can obtain

$$CMRR \approx 60 + 20log(\frac{V_{CMeff}}{V_{CM}}) - 20log\frac{V_{out}}{V_{CM}} \tag{2.34}$$

For example, when V_{out}/V_{CM} is -150 dB, CMRR is about 195 to 204 dB. Generally, practival value of the CMRR could be about 100 dB or higher for an instrumentation amplifier at 60 Hz, considering influences of the errors in circuit elements and noises. We use V_{out}/V_{CM} as our main benchmark in this thesis for evaluting how well the CM noise could be rejected as an external interference.

2.3 Imbalance cancellation design with digiPOTs and Evaluations

In Section 3.2, we showed to what extend an imbalance in the contact resistance can affect the three circuits. In this section, we exhibit the design that use digiPOTs to reduce the imbalance in the contact resistance, such that the CM noise is reduced further and give a better performance than DRL. In [25], a design using CdS as a variable resistor, or a rheostat, to compensate the imbalance in contact resistance was proposed. In our design, we choose the digiPOTs as alternative because it not only can be well adjusted through a digital controlling circuit, but it also has bigger end-to-end resistance and better resolution of resistance. The models we have chosen are the TPL0102-100 and TPL0202-10 of Texas Instruments. Table 2.2 shows the main parameters of them.

When the digiPOTs are installed, the equivalent circuits in Fig. 2.1 and Fig. 2.6 becomes what are shown in Fig. 2.9.

Table 2.2. The parameters of the digiPOTs TPL0102-100 and TPL0202-10

	TPL0102-100	TPL0202-10
Number of Steps	256	256
Number of Channels	2	2
End to end resistance	100 kΩ	10 kΩ
Resolution	≈ 390 Ω	≈ 39 Ω

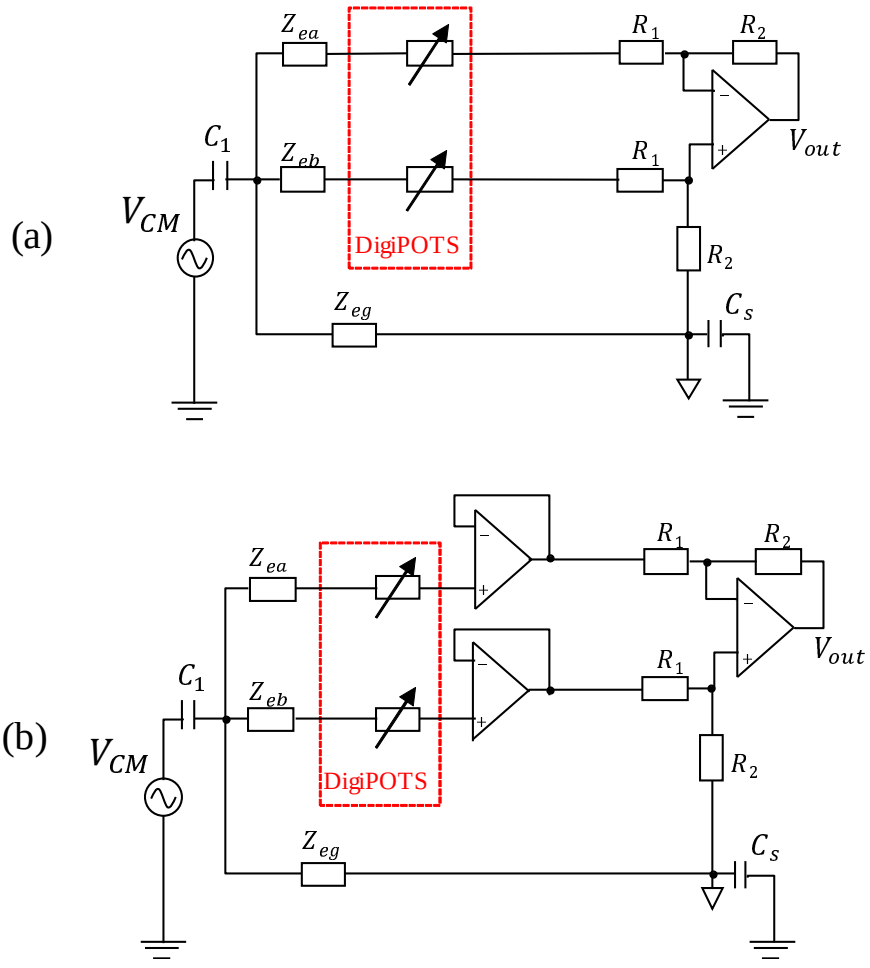

Fig. 2.9. CM equivalent circuit with the digiPOTs. (a) The circuit in Fig. 2.1 with digiPOTs installed. (b) The circuit in Fig. 2.6 with digiPOTs installed.

For each channel, the end-to-end resistance of the TPL0102-100 is 100 kΩ with 256 taps and its resolution is about 390.6 Ω. Thus, if we use this digiPOT to cancel the imbalance, it can be adjusted to no more than about 390.6 Ω, in the

range of $0 \sim 100$ kΩ. In the case of the TPL0202-10, the end-to-end resistance is 10 kΩ. It also has 2 channels and 256 taps with a resolution of about 39.1 Ω. As a result, the range that it could function becomes smaller ($0 \sim 10$ kΩ), but it can make the imbalance be compensated to no more than 39.1 Ω.

With the circuits shown in Fig. 2.9 simulated in SPICE, we can evaluate how well does the digiPOTs work in reducing the CM noise by cancelling the imbalance in resistance. Fig. 2.10 is the result of a comparison among the circuits in Fig. 2.1 (No-cancellation), Fig. 2.3 (DRL) and Fig. 2.9(a) (Digipt100K). The parameters are mostly the same as is shown in Table 2.1. The results of using a TPL0102-100 or TPL0202-10 are shown respectively.

The horizontal axis is the imbalance, whose calculation is given by equation (2.30). As is shown in Fig. 2.8, the influence of a positive imbalance (when Z_{eb} is bigger than Z_{ea}) or a negative imbalance (when Z_{ea} is bigger than Z_{eb}) do not have much difference, especially for the circuit in Fig. 2.3 and Fig. 2.6. Thus, we show the result at the range of from 0 % to 100%. In Fig. 2.10, the imbalance is set to change by every 10 Ω , while the resistance of the digiPOT change by its resolution. As we used the TPL0102-100 in Fig. 2.10 (a), its resistance changed by every 390.6 Ω during the simulation. In Fig. 2.10 (b), the TPL0202-10 is used, and its resistance changed by every 39 Ω. Of course, the range of imbalance becomes 10 kΩ. It should be noticed that in Fig. 2.10 (a) or (b), when the imbalance is compensated to almost the same as 0, the V_{out}/V_{CM} becomes extremely low (about $-$ 270 dB). However, as we cannot ensure that the resistance of actual electrodes change by every 390.6 Ω or 39 Ω, this figure shows frequent fluctuations. The worst case is determined by the resolution of the digiPOT, that is why the "Digipot10K" in Fig. 2.10 (b) shows a better rejecting effect. The best case are also affected by the resolution, but we can see that it does not have too much difference in Fig. 2.10(a) and Fig. 2.10(b).

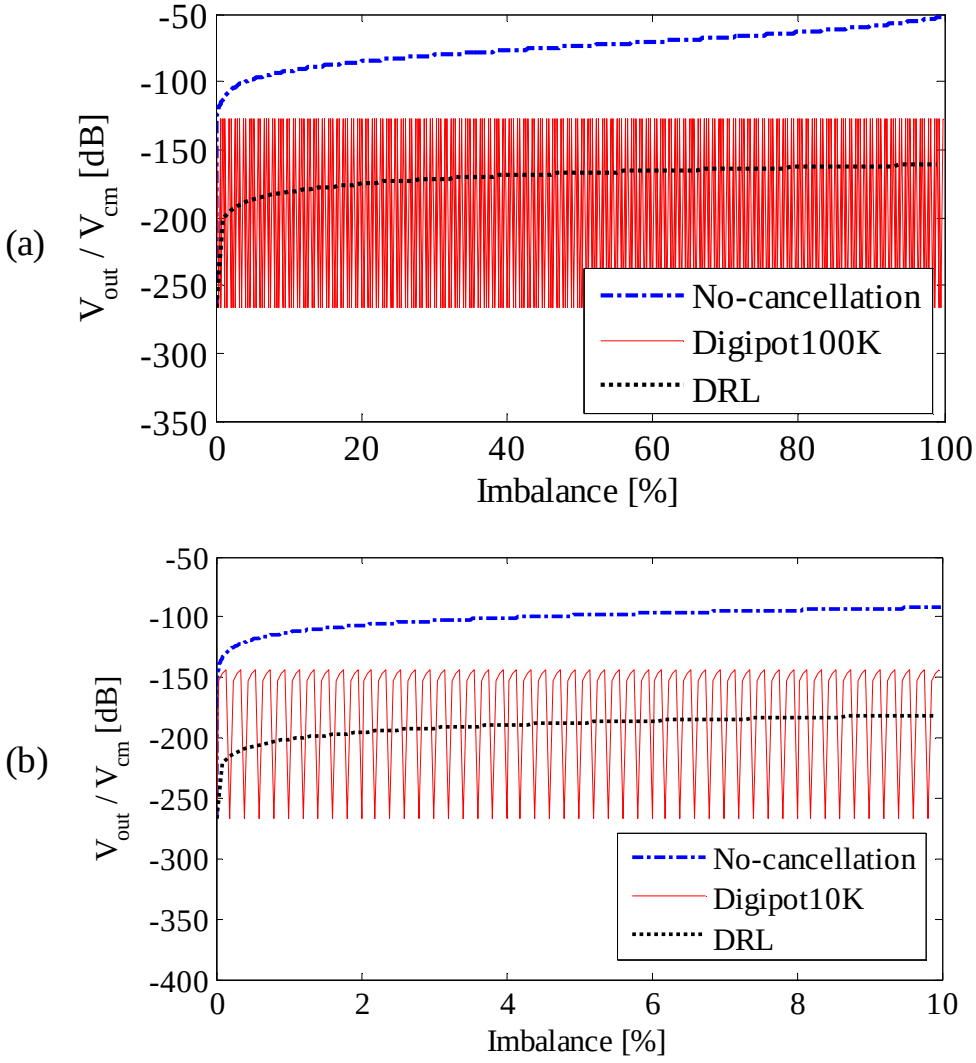

Fig. 2.10. The result of comparison among the three circuits. "No-cancellation" and "DRL" in (a) and (b): the same as the result in Fig. 2.8. "DigiPOT100K" in (a): TPL0102-100 used in the circuit of Fig. 2.9 (a). "DigiPOT10K" in (b): TPL0202-10 used in the circuit of Fig. 2.9 (a).

Indeed, what we are seeking for is a design that can exceed the DRL, while the result in Fig. 2.10 shows that just by applying digiPOTs in the circuit in Fig. 2.1 is not capable of realizing our goal. At most time, the DRL seems to work better in reducing the influence of the CM noise in Fig. 2.10. As we know that our design shown in Fig. 2.6 receives less CM interference than the circuit in Fig. 2.1, there

is a possibility that the circuit in Fig. 2.9 (b) works better than the DRL and Fig. 2.9(a). In order to verify this idea, we conducted a circuit simulation similar to the last one for the circuit of Fig. 2.9 (b). Fig. 2.11 shows the result of this evaluation. From Fig. 2.11, it is obvious that our design generally works better

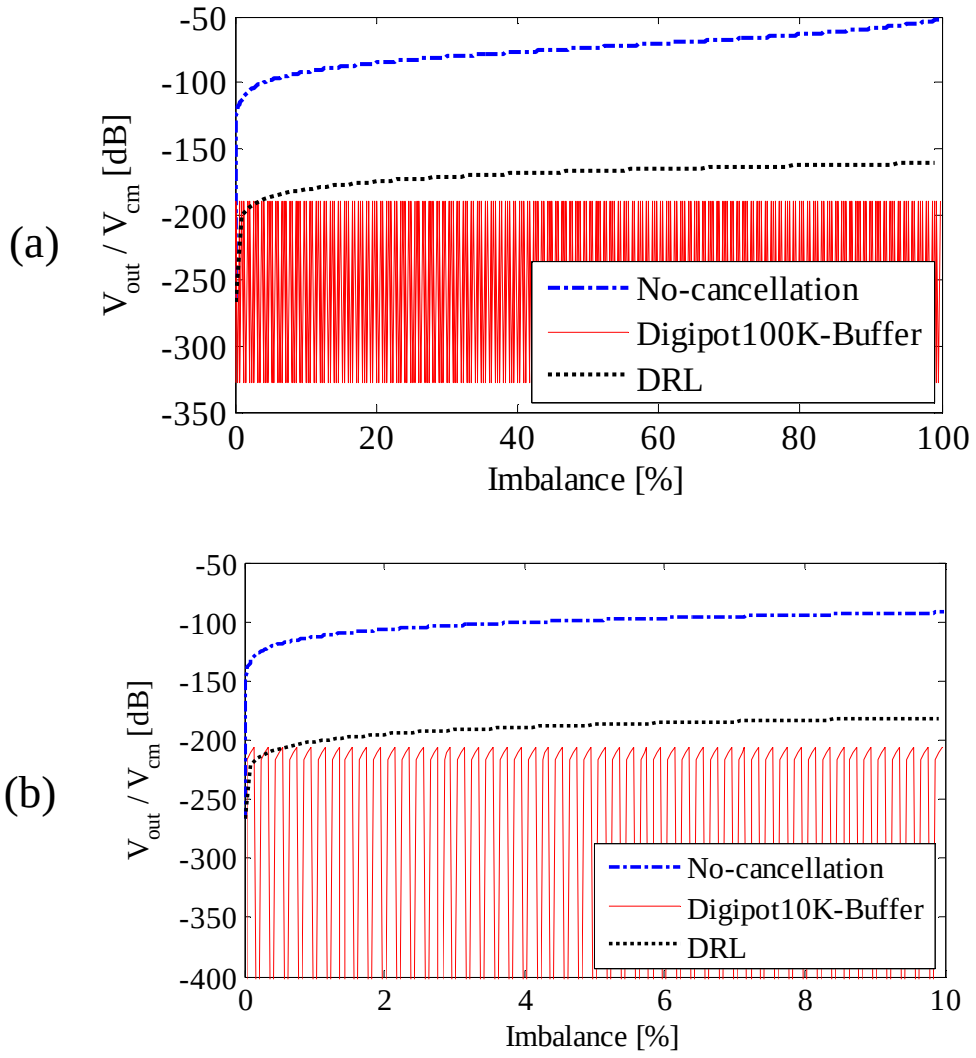

Fig. 2.11. The other result to show the performance of the circuit in Fig. 2.9 (b). "No-cancellation" and "DRL": the same as the result in Fig. 2.8. "DigiPOT100K-Buffer": TPL0102-100 used in the circuit of Fig. 2.9 (b). "DigiPOT10K-Buffer": TPL0202-10 used in the circuit of Fig. 2.9 (b).

than the DRL circuit in rejecting the CM noise. By comparing Fig. 2.11(a) and

Fig. 2.11(b), we can also find that the resolution of the digiPOT still decides the worst case and the best case. In comparison with Fig. 2.10, we can see that the CM noise becomes smaller, and our design could have a better performance that the DRL circuit, especially when there is a large imbalance in the resistance.

2.4 Conclusion and our contribution

The biopotential acquisition play an important role in the healthcare applications, and its accuracy and precision could be affected by the CM noise or EMI. We have clarified how much influence an imbalance in the contact resistance could have for three different kinds of circuits. The evaluation was conducted through circuit simulation, assuming that the three circuits are respectively used as a subsystem in the same acquisition scene. From the result, we know that the buffered design receives less interference from the CM voltage but more than the DRL circuit. One contribution of our work at this part lies in presenting the quantitative comparison of the CM noise reduction for the three different circuits, using the same CM noise model. This contribution provided us the inspiration about how to realize the DRL exceeding CM rejection circuit design.

The other contribution of this part's work lies in proposing the novel circuit design which employs the DigiPOTs to reject the CM noise. The performance of this design was evaluated through two circuit simulations respectively. Results implied that the design we proposed in can make it possible to exceed DRL. It was shown that our design can accomplish a V_{out}/V_{CM} of lower than $-$ 180 dB, which is about 20 $\sim$ 40 dB better than the average performance of DRL, depending on the resolution of the digiPOT and the amount of imbalance. It is possible that the actual performance of our design becomes worse than the simulation, because the imbalance could have a capacitance part and comes not only from the attachment of electrodes. However, it should be noticed that the DRL circuit has always

been accompanied with its problem of stability, while our design does not rely on any negative feedback like the DRL. The imbalance value can also affect the performance of the DRL significantly, while it does not have any influence in our approach because we make efforts to keep it at the same level.

Chapter 3

A Real Value of Our Approach: for Noncontact Biopotential Acquisition

3.1 Overview

Noncontact electrode is a promising alternative to achieve more comfortable and long term biopotential signal recordings than contact electrode. However, it could pick up significantly higher level of CM noise than contact one, and this problem is hardly solved with passive filtering. This chapter discusses about EBI impedance imbalance cancellation-based CM noise rejection approach for noncontact biopotential acquisition circuit.

The biopotential acquisition circuits with noncontact electrodes has some certain difference from those with contact electrodes. Because of the capacitive coupling at EBI, noncontact electrode has larger order of EBI impedance. The biopotential signal gain becomes harder to acquire, and more CM noise could interfere the acquisition circuit. Besides, the correlation between the EBI impedance imbalance and noise output becomes non-linear, making it more difficult to cancel the imbalance.

In order to show the difference in CM rejection for contact and noncontact biopotential acquisition circuits, we first introduce the relation between CMRR and EBI impedance imbalance. Chi et al. [58] expressed the CMRR in the following

shape:

$$CMRR \approx \frac{Z_i}{|Z_1 - Z_2|} \tag{3.1}$$

where Z_1 and Z_2 are the EBI impedances, Z_i is the input impedance of the biopotential amplifier. At low frequencies like 50 or 60 Hz, the impedances of noncontact EBIs are primarily capacitive and the expression simplifies to

$$CMRR \approx \frac{C_1 C_2}{C_i |C_1 - C_2|} \tag{3.2}$$

From (3.2) we can see that for noncontact or capacitive electrodes, an imbalance of picofarads can reduce the CMRR more severely than contact ones, whose imbalance is usually in the order of kiloohms. This fact is the reason why a capacitive sensing scheme is so sensitive to impedance variations.

In this chapter, we present two novel CM noise reduction circuit designs using digitally tunable capacitor (DTC). The designs are based on EBI impedance imbalance cancellation. We perform circuit analysis and circuit simulations to explain the principles of both the two circuits. In order to implement our design, we propose an original design of DTC that can meet the terms for circuit evaluation. Evaluative circuit board was built for experimental evaluation. The results revealed the validity and feasibility of the approach.

3.2 Circuit analysis

3.2.1 Proposal 1: "DTC Series"

In this section, we present our two biopotential acquisition circuit design proposals and analyze how they work in reducing the CM noise. The assumed acquisition model and the conditions of our circuit analysis are shown in Fig. 3.1. There are two noncontact sensing electrodes and one ground electrode. The biopotential signals are acquired from the two sensing electrodes. The EBI capacitance is denoted as C_{ea} or C_{eb}. Usually they are unbalanced due to the different attachment

conditions. C_{eg} denotes the impedance of the ground electrode. In addition, the stray capacity between the circuit ground and the earth ground is denoted as C_s. The interference voltage V_{CM} is between the human body and the earth ground. The same as our discussion on contact biopotential sensing circuit in Chapter 2, this model could be considered as a usual one for single channel ECG, EEG, EOG, etc. Theoretically a 2-wired sensing circuit can also be employed to acquire one channel of biopotential, but a ground electrode or a driven-right-leg (DRL) electrode is generally necessary to reject noise and reduce errors.

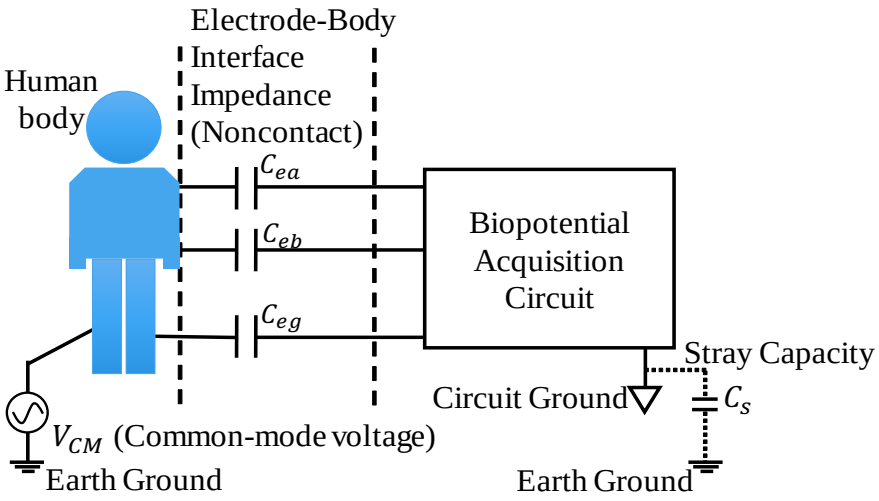

Fig. 3.1. Assumed acquisition model and conditions of circuit analysis

Fig. 3.2 shows the CM equivalent circuit of our first proposal, which we call it as "DTC Series". It is based on the noncontact 3-wired single channel biopotential acquisition model shown in Fig. 3.1. Two buffer amplifiers are used to provide high input impedance. There are two grounds for the circuits in Fig. 3.2 and the other circuits we handle. One is the circuit ground for differential mode voltage. The operational amplifier (OP-AMP)'s ground is this ground and the OP-AMP circuit thus works normally. The other ground is the earth ground for common mode voltage. This ground is floating, and the floating is difficult to be solved by

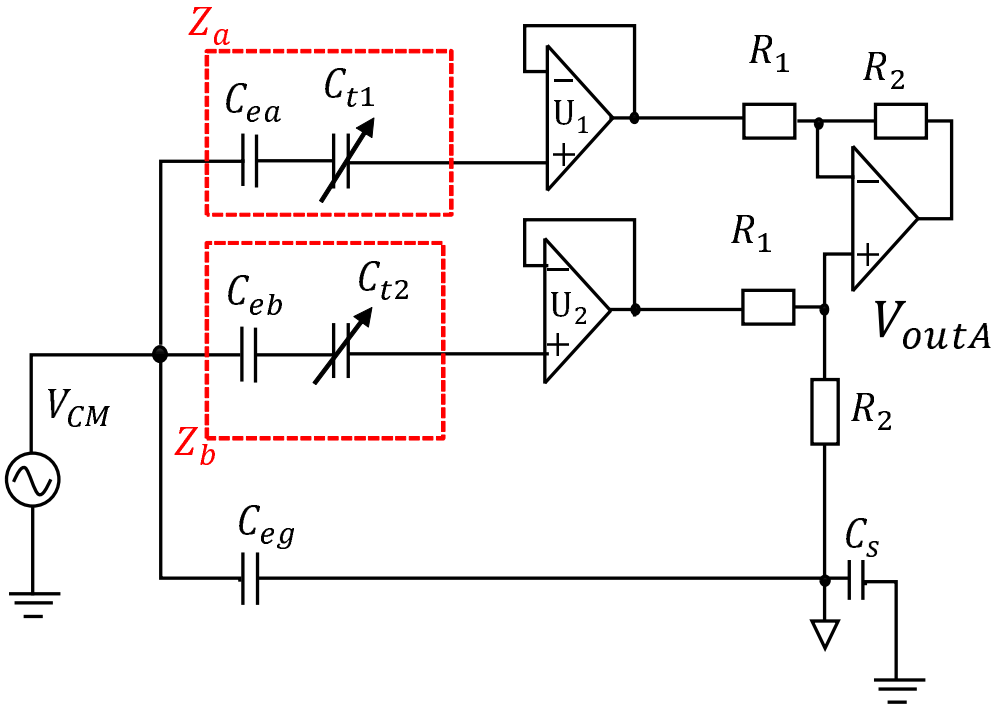

Fig. 3.2. CM equivalent circuit of "DTC Series"

autozero or a similar mechanism because it is the earth. The input to the OP-AMP contains both the differential mode voltage and the common mode voltage, and the common mode voltage is converted into a differential voltage as a noise at the OP-AMP output. Between the electrodes and the buffers, two DTC elements C_{t1} and C_{t2} are installed in series to the input impedance of the buffer. The biopotential signals are differentially amplified with an operational amplifier (OP-AMP). The OP-AMPs are non-ideal because if they are, the currents i_a and i_b in Fig. 3.2 become zero and the CM noise would not affect this circuit. The input offset voltages of the buffers are designed to be very low such that the input and output voltages of them are assumed to be equal.

We also perform some circuit analysis and calculations on the equivalent circuit in Fig. 3.2. This circuit is basically the same as the pre-amplified circuit shown in Chapter 2. Change the EBI impedance part to Z_a and Z_b shown in Fig. 3.2, and

change Z_{eg} to $1/(j\omega C_{eg})$, V_{outA} can be written as

$$V_{outA} = \frac{j\omega C_s Z_{eg} R_1 (R_1 + R_2)(Z_{eg} + Z_{in})(Z_a - Z_b) V_{CM}}{R_2 (Z_{ea} + Z_{in})[(1 + j\omega C Z_{eg})(R_1 + R_2)(Z_{eg} + Z_{in}) + Z_{eg}(Z_a - Z_b + Z_{in})]} \tag{3.3}$$

where

$$Z_a - Z_b = (\frac{C_{ea} - C_{eb}}{j\omega C_{ea} C_{eb}} + \frac{C_{t1} - C_{t2}}{j\omega C_{t1} C_{t2}}) \tag{3.4}$$

and Z_{in} is the input impedance (with respect to the circuit ground) of the amplifier U1 or U2. From (3.3), we can know that if $(Z_a - Z_b)$ is zero, then the output of CM noise V_{outA} also becomes zero. Therefore, we can adjust the capacitance of C_{t1} and C_{t2} to cancel the imbalance between C_{ea} and C_{eb} such that the CM noise is reduced. Besides, this imbalance cancellation is independent to the frequency, which means that theoretically we can drive down the CM noise of all frequencies to extremely low level once C_{t1} and C_{t2} are exactly adjusted.

3.2.2 Proposal 2: "DTC Bypath"

There is another circuit design to achieve capacitive imbalance cancellation. Its CM equivalent circuit is shown in Fig. 3.3. This design tries to make the voltage at V_a and V_b to be equal, like the famous Wheatstone bridge. We call this proposal as the "DTC Bypath".

Now we try to write down the relation between V_{outB} and V_{CM} in Fig. 3.3 as we did on the other circuits. At the circuit notes 1, 2 and 3 denoted in the figure, we can use the Kirchhoff's Current Law again and get the following three equations

$$\frac{V_a - V_1}{R_1} + \frac{V_{outB} - V_1}{R_2} = 0 \tag{3.5}$$

$$\frac{V_b - V_1}{R_1} = \frac{V_1 - 0}{R_2} \tag{3.6}$$

$$\frac{V_1 - 0}{R_2} + \frac{V_{in} - 0}{\frac{1}{j\omega C_{eg}}} = (0 - V_E) j\omega C_s \tag{3.7}$$

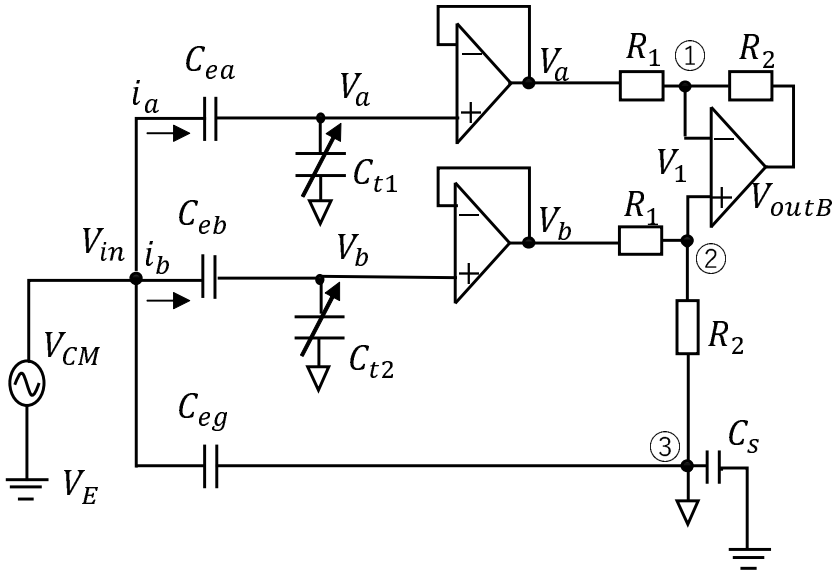

Fig. 3.3. CM equivalent circuit of "DTC Bypath"

On the other hand, according to Ohm's Law, at the part of C_{ea} and C_{eb}, it is clear that

$$V_{in} - V_a = \frac{i_a}{j\omega C_{ea}} \tag{3.8}$$

$$V_{in} - V_b = \frac{i_b}{j\omega C_{eb}} \tag{3.9}$$

For the noise source V_{CM}, we have

$$V_{in} - V_E = V_{CM} \tag{3.10}$$

Bisides, by using Ohm's Law again, i_a and i_b can be written as following shape

$$i_a = \frac{V_{in}}{\frac{1}{j\omega C_{ea}} + C_{t1}//Z_{in}} \tag{3.11}$$

$$i_b = \frac{V_{in}}{\frac{1}{j\omega C_{eb}} + C_{t2}//Z_{in}} \tag{3.12}$$

where "//" stands for parallel connection. This is because that the input impedance of the buffer is equivalently connected with C_{t1} or C_{t2} in parallel. Combine (3.8) and (3.11), we can get the relation between V_a and V_{in}

$$V_{in} - V_a = \frac{V_{in}}{1 + j\omega C_{ea}(\frac{1}{j\omega C_{t1}} + \frac{1}{Z_{in}})} \tag{3.13}$$

Also the relation between V_b and V_{in} is in the same shape

$$V_{in} - V_b = \frac{V_{in}}{1 + j\omega C_{eb}(\frac{1}{j\omega C_{t2}} + \frac{1}{Z_{in}})} \tag{3.14}$$

Use (3.6) and (3.14), we can get the relation of V_1 and V_{in}

$$V_{in} - V_1(1 + \frac{R_1}{R_2}) = \frac{V_{in}}{1 + j\omega C_{eb}(\frac{1}{j\omega C_{t2}} + \frac{1}{Z_{in}})} \tag{3.15}$$

(3.15) can be deformed into

$$V_1 = V_{in} \times \frac{R_2}{R_1 + R_2} \times \frac{j\omega C_{eb} Z_{in}}{j\omega(C_{t2} + C_{eb})Z_{in} + 1} \tag{3.16}$$

From (3.5), (3.11) and (3.16), we can use V_{in} to stand for V_{outB}, which is written as

$$V_{outB} = \frac{R_2}{R_1} \times V_{in} \times [\frac{j\omega C_{eb} Z_{in}}{j\omega(C_{t2} + C_{eb})Z_{in} + 1} - \frac{j\omega C_{ea} Z_{in}}{j\omega(C_{t1} + C_{ea})Z_{in} + 1}] \tag{3.17}$$

From (3.17) we can see that the relation between V_{outB} and V_{CM} can be derived if we can present V_{CM} with V_{in}. This mission can be accomplished by using (3.7) and (3.10) to get the following equation

$$V_{in} = \frac{V_{CM} j\omega C_S - \frac{V_1}{R_1}}{j\omega(C_{eg} + C_s)} \tag{3.18}$$

Form (3.18), we eliminate V_1 by using (3.16), and bring the result into (3.17), finally V_{outB} can be written as

$$V_{outB} = \Psi \cdot \frac{\Gamma}{\Pi} \cdot V_{CM} \tag{3.19}$$

where

$$\Gamma = \omega^2 Z_{in}(C_{ea}C_{t2} - C_{eb}C_{t1}) + j\omega(C_{eb} - C_{ea}) \tag{3.20}$$

Ψ and Π are coefficients given by

$$\Psi = \frac{j\omega C_s(R_1 + R_2)[j\omega(C_{eb} + C_{t2})Z_{in} + 1]}{R_2 j\omega(C_{eb}Z_{in} + j\omega(C_{eg} + C_s)[j\omega(C_{eb} + C_{t2})Z_{in} + 1](R_1 + R_2)} \tag{3.21}$$

$$\Pi = -\omega^2 Z_{in}^2(C_{eb} + C_{t2})(C_{ea} + C_{t1}) + j\omega(C_{ea} + C_{t1} + C_{eb} + C_{t2}) \tag{3.22}$$

If we want V_{outB} to be zero, which can be derived by letting $\Gamma = 0$, we can get

$$\frac{C_{ea}}{C_{eb}} = \frac{j\omega C_{t1} Z_{in} + 1}{j\omega C_{t2} Z_{in} + 1} \tag{3.23}$$

This equation can also be derived by letting $V_a = V_b$, where V_a and V_b are the input voltages of the buffers denoted in Fig. 3.3. From this equation, we can see that the CM noise can be reduced by adjusting the C_{t1} and C_{t2}. It should be noted that (3.23) is affected by frequency, and if ωZ_{in} is large enough, (3.23) becomes

$$\frac{C_{ea}}{C_{eb}} = \frac{C_{t1}}{C_{t2}} \tag{3.24}$$

It reveals that by employing "DTC Bypath" we can reduce the CM noise through matching $C_{ea}/\ C_{eb}$ and C_{t1}/C_{t2}.

3.3 Circuit simulation and results

3.3.1 Without the DTCs

In this section, we use the SPICE (Simulation Program with Integrated Circuit Emphasis) to show simulation results of our proposal, in comparison with a circuit without the DTCs.

Fig. 3.4 shows the CM equivalent circuit for biopotential acquisition without the DTCs. Parameters of the simulated circuit components are shown in Table 3.1. All the OP-AMPs in the circuit are simulated with the model of OP07 (Analog Devices), because we would like to employ its advantages as a bipolar junction transistor to drive down the offset voltage. Fig. 3.5 shows the simulated result

of output voltage normalized to CM noise for capacitance imbalance (-200 pF to 200 pF), i. e., the value of $(C_{ea} - C_{eb})$ in Fig. 3.4. It should be noted that when using a noncontact circular electrode, the capacitance can be calculated from

$$C = \varepsilon_r \varepsilon_0 \frac{\pi r^2}{d} \tag{3.25}$$

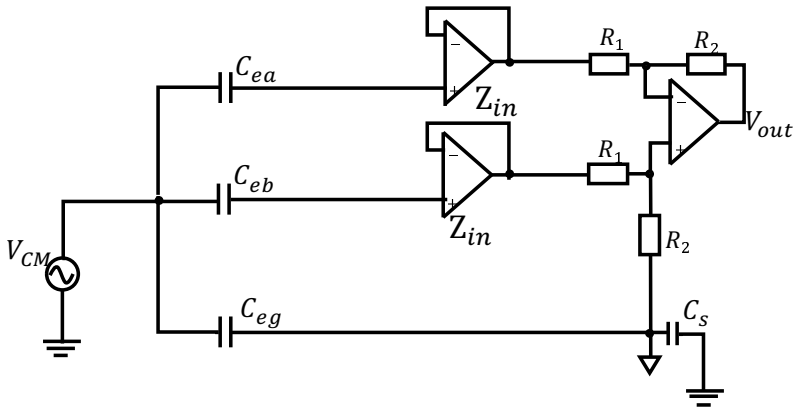

Fig. 3.4. CM equivalent circuit without the DTCs

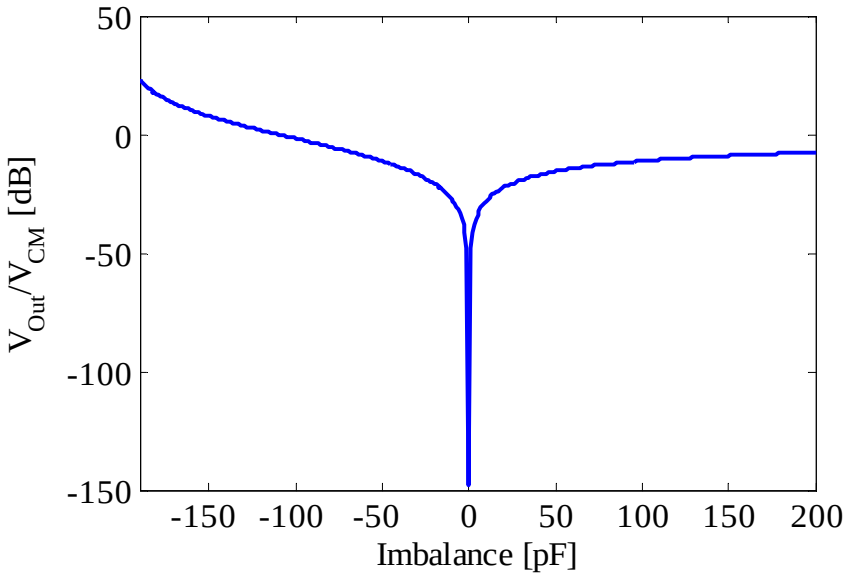

Fig. 3.5. Simulated result of output voltage normalized to CM noise input for capacitance imbalance −200 pF to 200 pF (Table 3.1's condition).

Suppose that we have a stiff plate ECG noncontact electrode with a radius r of 2 cm, and the relative permittivity ε_r of clothes is about 5 to 10. The thickness d between the human body and the electrode could be about 0.1 to 0.5 mm, depending on the clothes. With these parameters, the EBI capacitance could be 100 to 200 pF. Therefore, we assume that the capacitance of C_{ea} and C_{eb} are in

Table 3.1. Parameters of circuit components in Fig. 3.4

Parameter	Value	Parameter	Value
Frequency	60 Hz	V_{CM}	1 V
C_{ea}	1 pF to 400 pF	R_1	10 kΩ
C_{eb}	200 pF	R_2	10 MΩ
C_{eg}	200 pF	C_s	200 pF

hundred picofarad order. Ha et al. [24] also mentioned the approximate value of noncontact electrodes' coupling capacitance as 1 pF to 10 nF, depending on their type and attachment conditions. From Fig. 3.5 it can be seen that when the absolute value of imbalance increases, the noise output becomes larger. If C_{ea} is near to 0 (which means that the attachment to human body is near to open), the CM noise increases severely. If the capacitance of C_{ea} and C_{eb} are matched exactly, V_{outA}/V_{CM} becomes $-$ 150 dB, which implies that the noise output is near to zero when there is no imbalance. Generally, the imbalance of noncontact EBI capacitance is tens of picofarads or larger [53], V_{outA}/V_{CM} can be 0 to -10 dB in usual case.

3.3.2 "DTC Series"

Next we perform another simulation to confirm the effectiveness of our proposal "DTC Series". Table 3.2 shows the parameters we used to simulate the circuit elements in Fig. 3.2. The other parameters are the same as we have shown in Table 3.1. C_{t1} is tuned from 300 pF to 500 pF, and we can see that V_{outB}/V_{CM} becomes -150 dB when C_{t1} is 400 pF. At this point, capacitances of C_{t1} and C_{t2} compensate the imbalance between C_{ea} and C_{eb} exactly, such that the CM noise is extremely reduced. Comparing this result with Fig. 3.5, this circuit can drive down the V_{CM} by more than 20 dB if the imbalance is cancelled to below 20 pF.

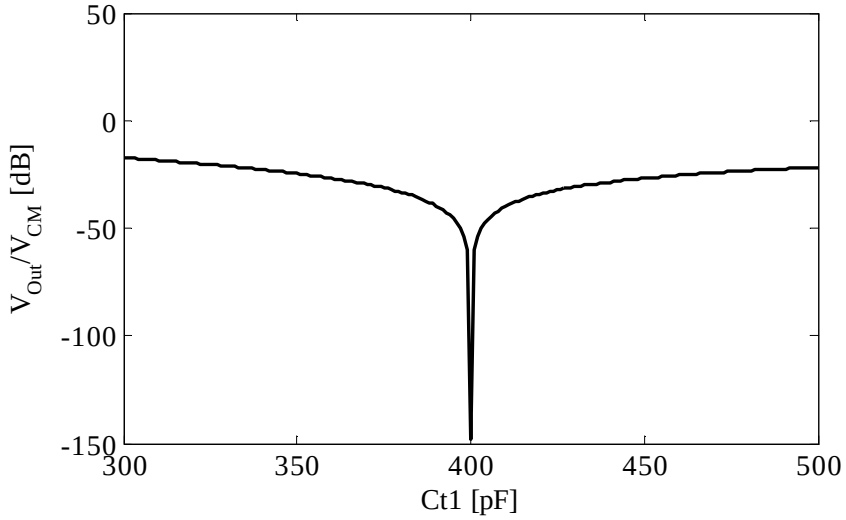

Fig. 3.6. Simulated result of output voltage normalized to CM noise for "DTC Series" under Table 3.2's condition.

Table 3.2. Parameters of the simulated circuit components for "DTC series"

Parameter	Value	Parameter	Value
Frequency	60 Hz	V_{CM}	1 V
C_{ea}	200 pF	C_{t1}	300 pF to 500 pF
C_{eb}	400 pF	C_{t2}	200 pF

3.3.3 "DTC Bypath"

We performed a simulation in almost the same way on "DTC Bypath". The parameters of the circuit components in this simulation are shown in Table 3, and the results are shown in Fig. 3.7. Because C_{t2} is 400 pF, by calculation we can know that C_{t1} should be about 199.5 pF to meet the relation in (3.23), which matches the simulated result in Fig. 3.7. At its lowest point, V_{outB}/V_{CM} becomes about -70 dB. By comparing the two results in Fig. 3.6 and Fig. 3.7 we can see that generally "DTC Series" works better than "DTC Bypath" in the same conditions. One reason why "DTC Bypath" design does not work as good as the previous one is shown by our previous circuit calculation, especially, (3.19) and (3.23).

Because this design accomplishes the noise rejection job through approximately matching the equation in (3.23), it is hard to get perfect imbalance cancellation in this design. However this disadvantage can still be compensated with its merit: it does not have to fix the value of the DTC, its effectiveness could be realized by approximately matching (3.23), as long as the order of DTC C_{t1} and C_{t2} is not smaller than the impedance of EBI. The reason is that this design increases current flow at the input, especially when the DTCs are not well adjusted.

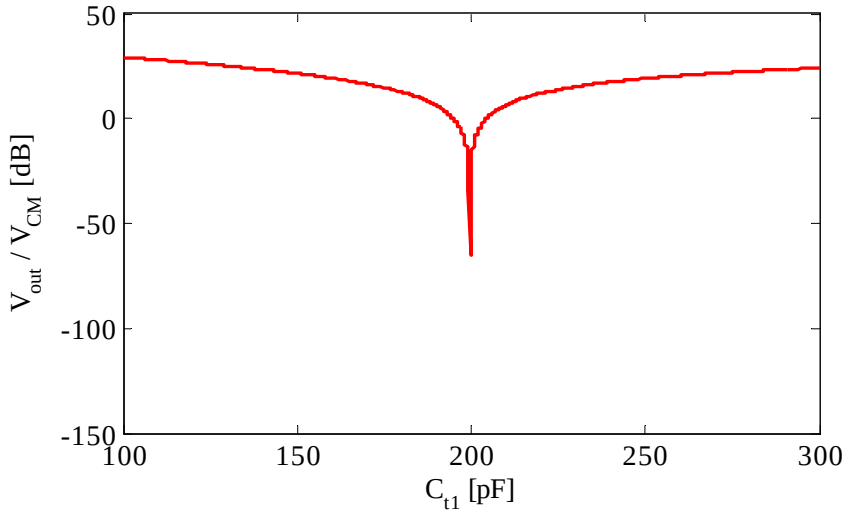

Fig. 3.7. Simulated result of output voltage normalized to CM noise for "DTC Bypath" under Table 3.3's condition.

Table 3.3. The parameters of the simulated circuit components for "DTC Bypath"

Parameter	Value	Parameter	Value
Frequency	60 Hz	V_{CM}	1 V
C_{ea}	200 pF	C_{t1}	100 pF to 300 pF
C_{eb}	400 pF	C_{t2}	400 pF

3.3.4 Estimating the practical tunability step of the DTCs

In this section, we used rounded values for C_{ea} and C_{eb}. In a realistic case, these capacitances could take any value in a certain range. This may cause a gap between the simulated result and the actual performance. However, there are some facts that can help us estimate the tunability step of the DTCs, such that we can fill this gap.

The first fact is that the capacitance of a noncontact electrode generally varies in hundreds or tens of picofarad order, less than 1 nF. In this range, the two EBI capacitances are generally in the same order, such that the noise rejection is determined by the absolute value of the imbalance between them. From (3.3), we can also know this fact by using the actual factors: the input impedance Z_{in} is high enough to eliminate the influence of C_{ea} or C_{eb} in the denominator, and the output voltage be determined by the absolute value of the imbalance. Because of this fact, our simulation at the rounded point can be persuasive.

The second fact is that the actual accuracy of the adjustable capacitance step can be limited by many other factors. In our idea, basically the precision of the DTC cannot be higher than picofarads order. Stray capacitances and other factors can bring varies of errors to the circuit, which is also about several picofarads. Because of the errors, it is not very practical to use large C_{t1} and C_{t2} to match equation (3.23), making the reasonable tunability step of "DTC Bypath" also stay in picofarads order.

Considering these two facts above, we can know that the reasonable tunability step of the DTCs is in picofarads order.

3.3.5 Signal gain performance

This part shows the signal gain performance of both the two proposed circuit designs. Pseudo signal source (sine wave) was used together with a sine wave CM

noise source to examine the total CMRR of both the two circuits.

We inject the pseudo biopotential signal $Signal\_L$ and $Signal\_R$ at the EBI, and the CM noise source V_{CM} as we did in other simulations, between the human body and the earth ground. The pseudo biopotential signals are 500 μV, 5 Hz sine waves. V_{CM} is also a sine wave whose amplitude is 1 V and frequency is 60 Hz. The simulation circuit and FFT of voltage outputs are shown in Fig. 3.8, Fig. 3.9 and Fig. 3.10. From the results, we can see that both the two proposals can reject the noise at 60 Hz to low level, but in "DTC Bypath" the biopotential has some loss of signal level at 5 Hz, which is about -10 dB worse than the other two circuits.

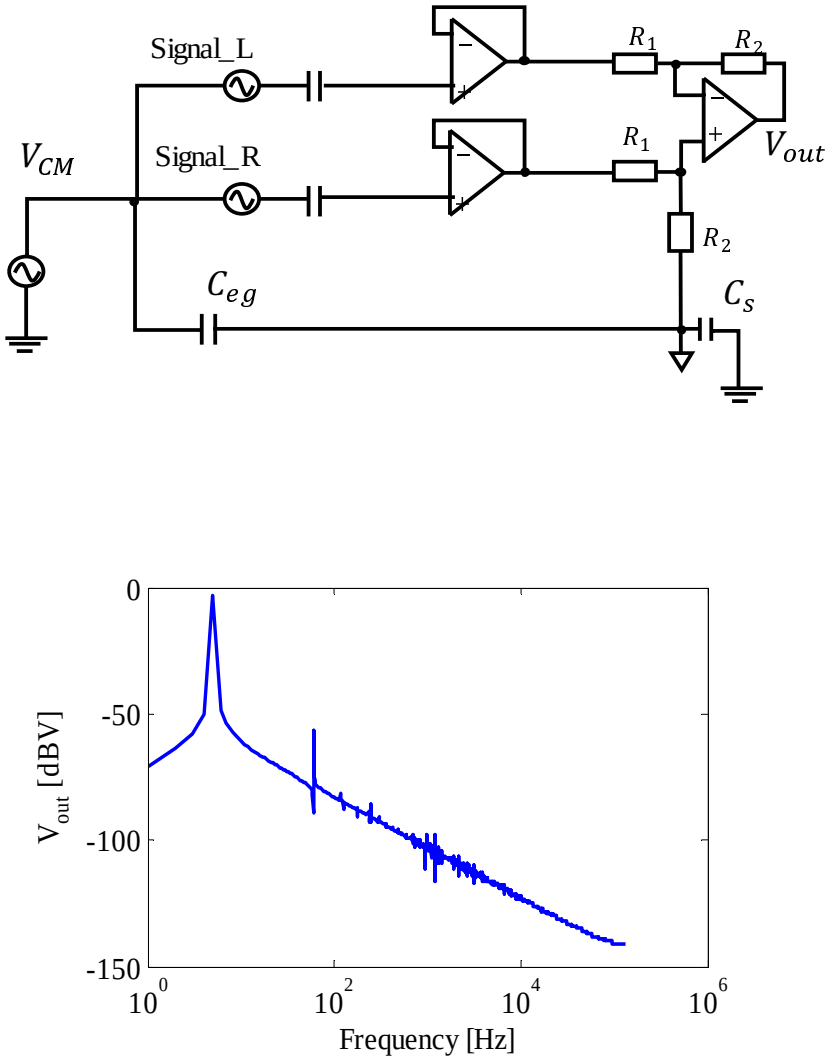

Fig. 3.8. Signal gain performance comfirming circuit and simulated result of the pre-amplifying circuit

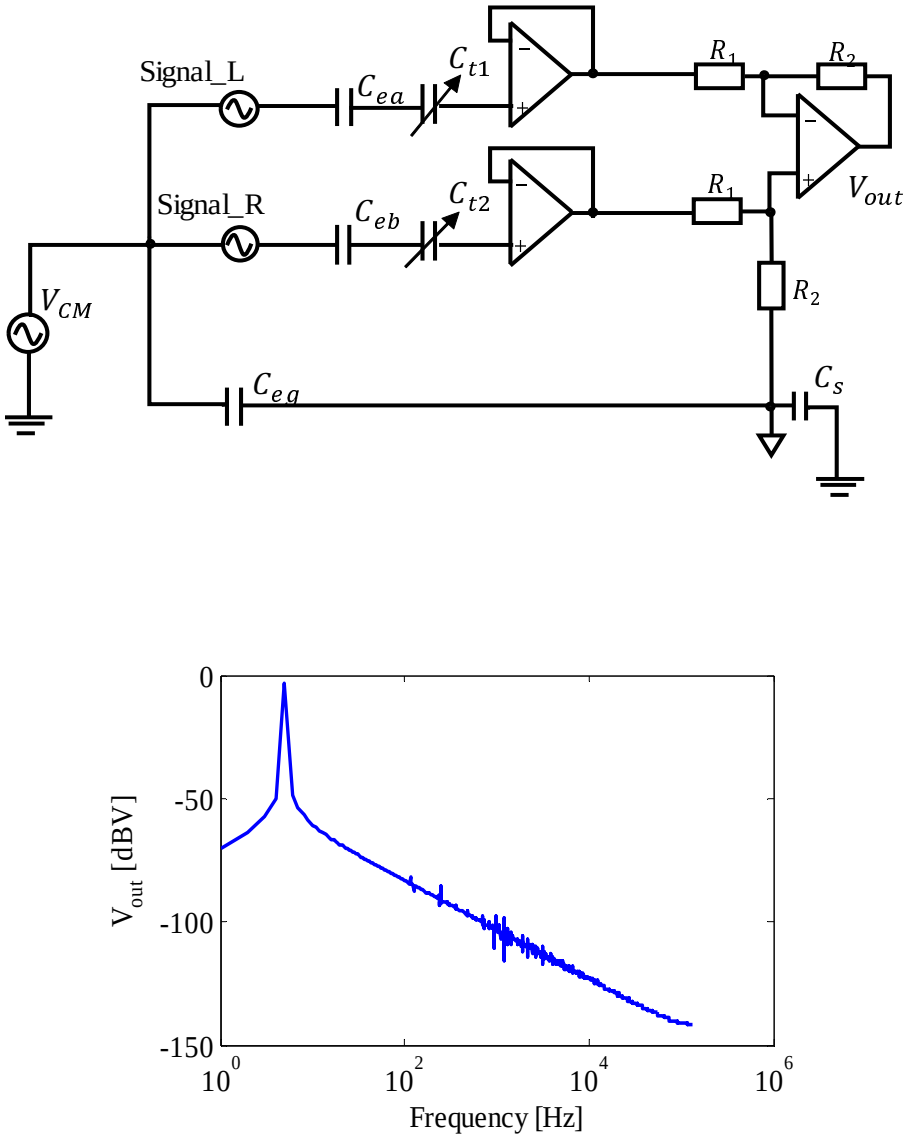

Fig. 3.9. Signal gain performance comfirming circuit and simulated result of "DTC Series"

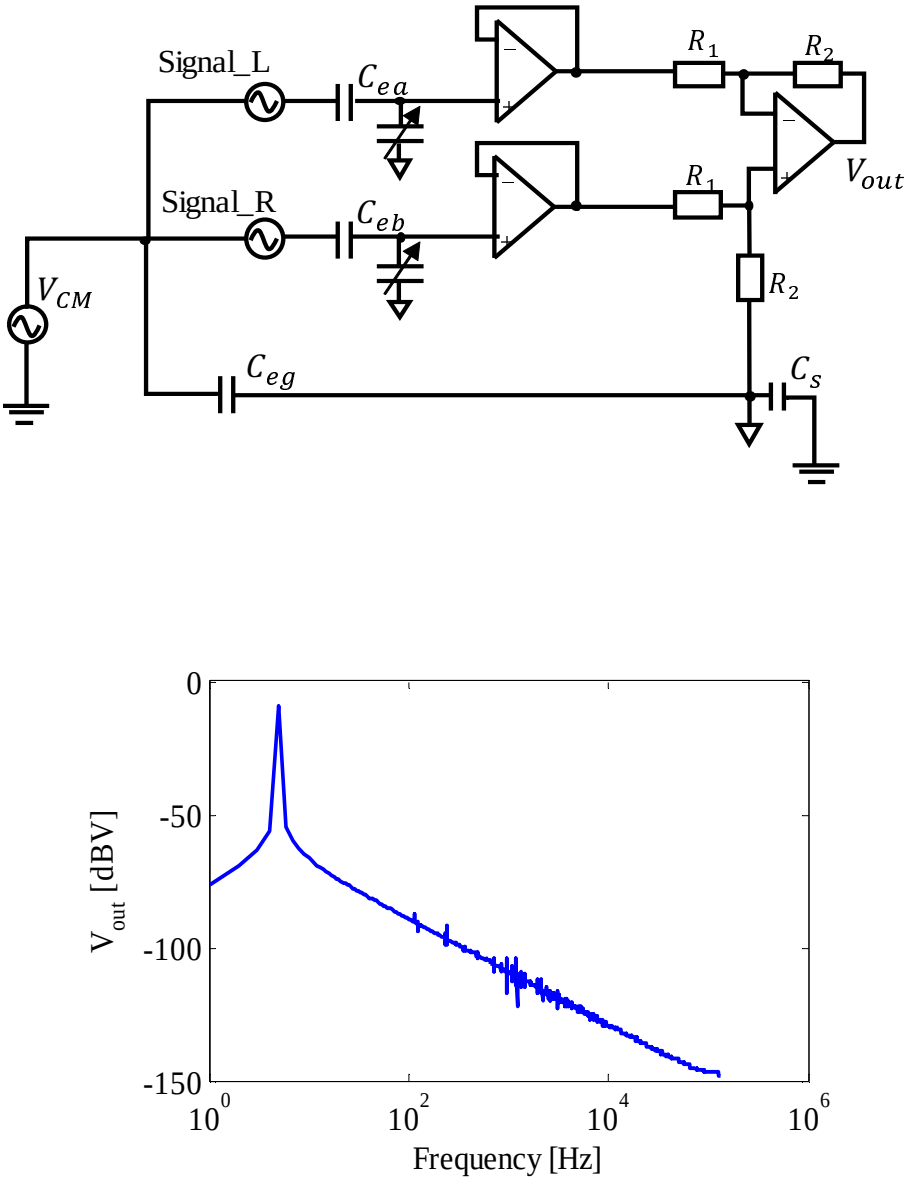

Fig. 3.10. Signal gain performance comfirming circuit and simulated result of "DTC Bypath"

3.3.6 Frequency characteristic

In order to investigate the frequency characteristic of each design, small signal AC (Alternating current) sweep was conducted and the results are shown in Fig. 3.11. The frequency ranges from 0.01 Hz to 10 KHz. The imbalance between C_{ea} and C_{eb} was set to 100 pF. Parameters of the simulated circuit components are shown in Table 3.4. C_{t1} and C_{t2} in "DTC Series" and "DTC Bypath" were exactly adjusted perfectly such that they show the best result of CM noise reduction. From Fig. 3.11, We can see that V_{out}/V_{CM} of "DTC Bypath" remained at high level when the frequency was lower than 1 Hz, which was not a good performance. On the other hand, the noise reduction effect of "DTC Series" performed better than "DTC Bypath" by more than 100 dB. When the frequency increased, the noise reduction effect of "DTC Series" becomes worse, but still better than the other design. Most artifacts are at low frequency (below 100 Hz). In conclusion, the "DTC Series" generally works better than "DTC Bypath" in the frequency range of biopotential signals. Besides, it should be noted that the frequency response of an actual biosignal acquisition circuit can affect the result.

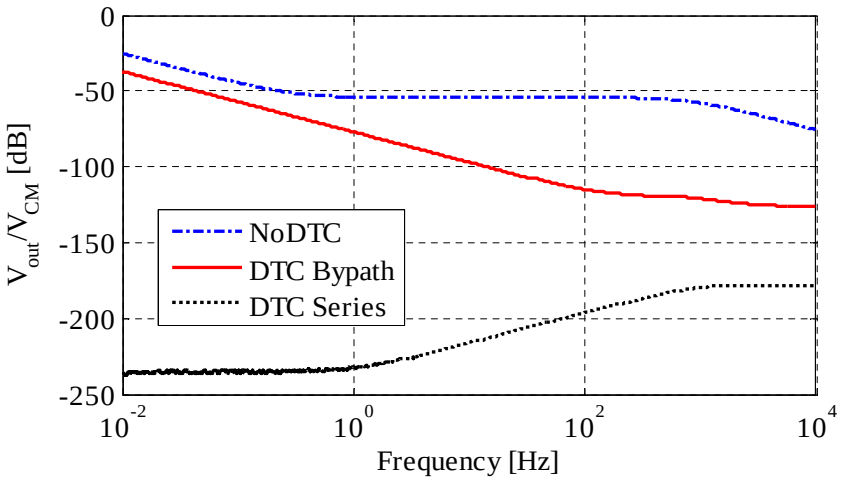

Fig. 3.11. Simulated result of small signal AC sweep under Table 3.4's condition.

Table 3.4. Parameters of the circuit components for the AC sweep

Parameter	Value
C_{ea}	200 pF
C_{eb}	100 pF
C_{t1} ("DTC Series")	100 pF
C_{t2} ("DTC Series")	200 pF
C_{t1} ("DTC Bypath")	201 pF
C_{t2} ("DTC Bypath")	100 pF

3.4 DTC design and experimental evaluations

3.4.1 Introduction to DTC chips and our design

In the last part we have shown that "DTC Series" had a better performance, thus we choose this design and perform experimental evaluations on it. In this section, we first give a introduction to the existing DTCs and explain our originally designed DTC. After that, we present our experimental evaluation on CM noise reduction effect.

There are mainly three different kinds of digitally tunable capacitors. MEMS devices have the highest quality factor and are highly linear, and therefore are suitable for antenna aperture tuning, dynamic impedance matching, power amplifier load matching and adjustable filters. RF tuning Micro-Electro-Mechanical System (MEMS) contains four individually controllable series capacitors. Fig. 3.12 shows the picture and fuctional block diagram of a RF tuning MEMS sample [59]. There are two reasons why the RF tuning MEMS cannot support our application: too small tuning range and too high operating frequency.

The second type of DTC that we introduce is the BST device (Fig. 3.13). A sample of this kind of device is the STPTIC-82c4 of STMicroelectronics [60]. It can be tuned with a bias voltage, and the effective capacitance of it can range from 2 to 12 pF. However, it also has a problem about its operating frequency for

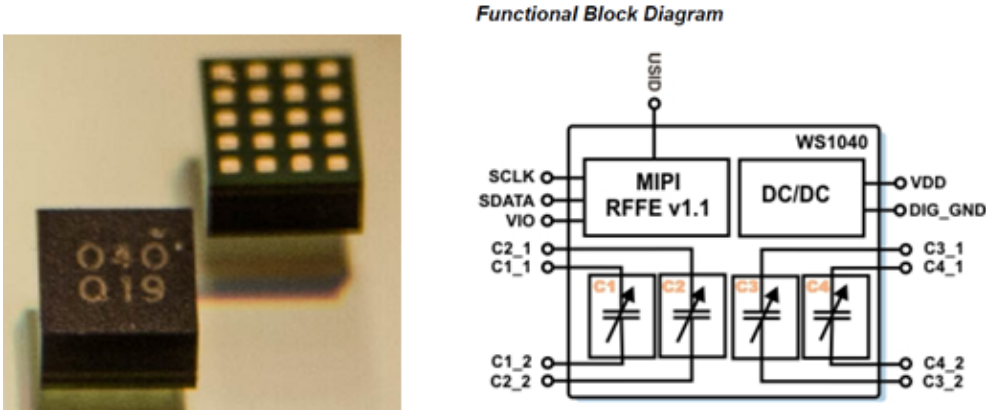

Fig. 3.12. RF tunable MEMS WS1040 [59]

our design. We need a DTC that can function stably at the biopotential frequency range, which could be 0.01 Hz to 1 kHz.

The third type of DTC is the Silicon on isolator (SOI)/silicon on sapphire

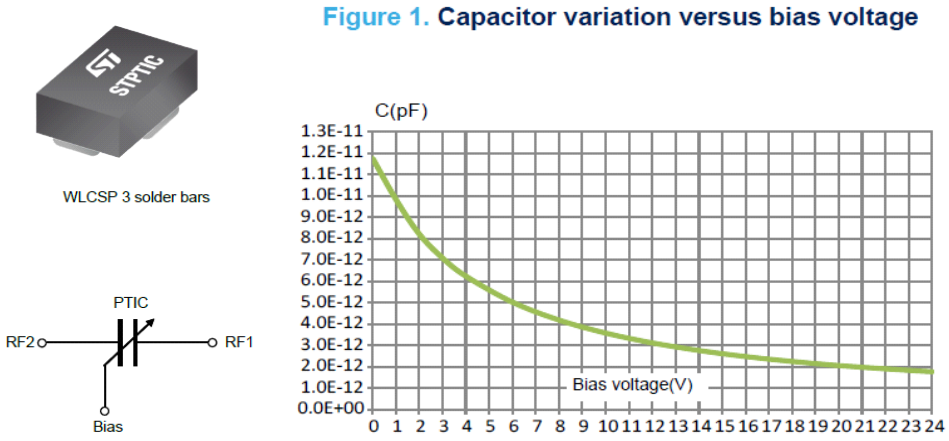

Fig. 3.13. BST device STPTIC-82c4 [60]

(SOS) tuning device. SOI/SOS tuning devices are constructed as solid state FET switches built on insulated CMOS wafers and use metal insulator metal (MIM) caps arranged in binary-weighted values to achieve different capacitance values. A sample of this kind of device, PE64102 [61], is shown in Fig. 3.14. This device has the best end-to-end capacetance and linearity among the three types of devices.

However, operating frequency is still a problem.

The other types of variable capacitors like varicap diode does not have good

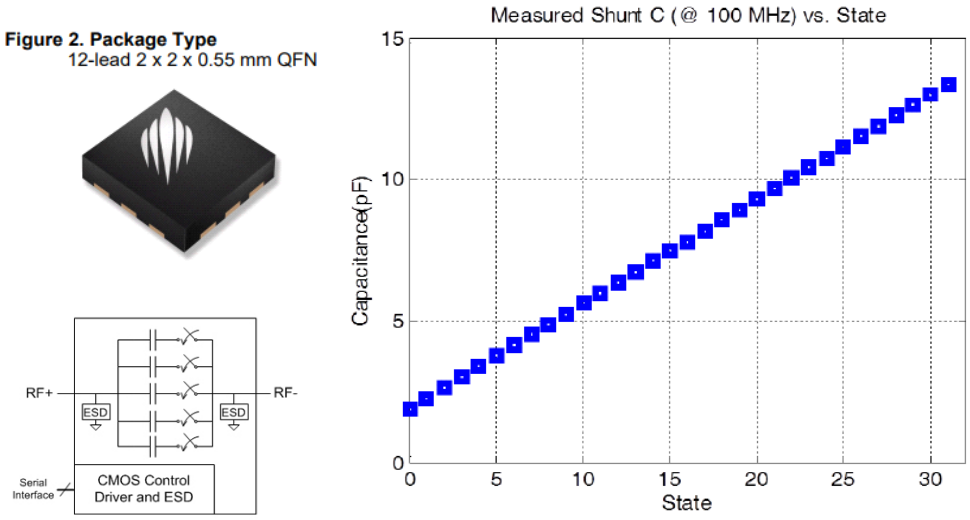

Fig. 3.14. PSEMI SOI/SOS tuning device PE64102 [61]

digital tunability. For our circuit, the DTC device must have availability in biopotential frequency, big tunable range (hundreds of picofarads), good linearity, and digitally tunability. It is true that even if the DTC does not good linearity for tuning, it could still be emplyed to cancell the imbalance. However, for the same end-to-end capacitance, if there is no good linearity, the correlation between the tuning step (resolution) of the DTC and the digital code becomes complecated, which makes the right and precise control of the DTC become very hard. For these reasons, we developed our original DTC.

In Fig. 3.15, the equivalent circuit of our originally designed DTC is presented. It consists of several channels of capacitors connected in parallel, each channel is controlled by one analog switch. For example, in ideal case, if we make the capacitance of each channel to be like 1 pF, 2 pF, 4 pF, 8 pF, 16 pF, ..., 512 pF, then the capacitance value can be binarily tuned in the range of 1 pF to 1 nF, by switching on or off each channel with a digital signal. We employed

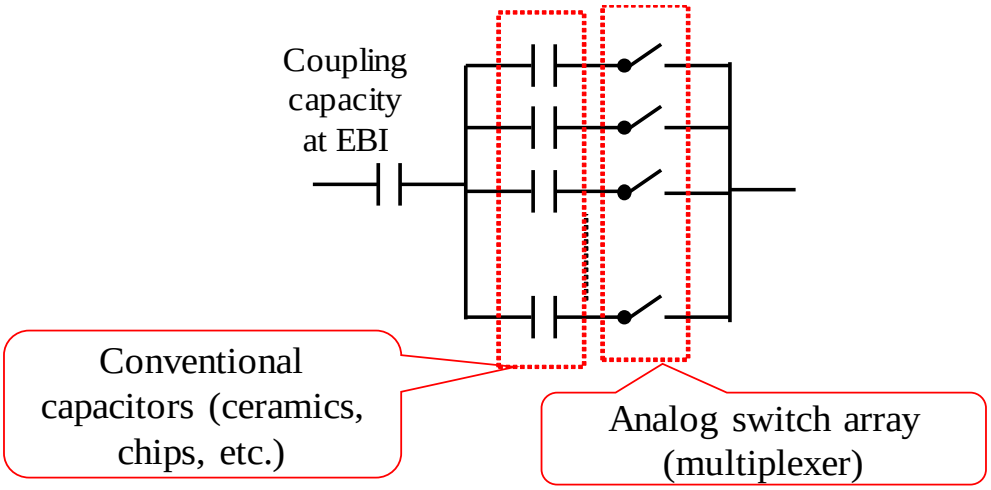

Fig. 3.15. Equivalent circuit of our originally designed DTC

the analog switch array, or multiplexer, to construct the structure shown in Fig. 3.15. The analog switch array that we employed consists of MOSFETs (metal-oxide-semiconductor field-effect transistor). When they work as an analog switch array, the level of gate voltage controls the current flow between source and drain, realizing a digitally controlled switch on or off operation. Because we connected a capacitor in series on each channel and combined all the inputs or outputs respectively, the capacitance value increases when the channel switch is on or decreases when it is off. A microcomputer was employed to implement the controlling part. The multiplexer reads in digital data from the microcomputer such that it can be digitally tuned.

3.4.2 Experimental evaluations

Fig. 3.16 shows the configuration of our evaluative board. It employs two DTCs and a microcomputer to monitor and cancel the EBI capacitance imbalance. The monitoring part in our system will be introduced in the next chapter. Fig. 3.17 is a picture of our evaluation board. We constructed the system shown in Fig. 3.16

on a universal board to experimentally evaluate the performance of our design.

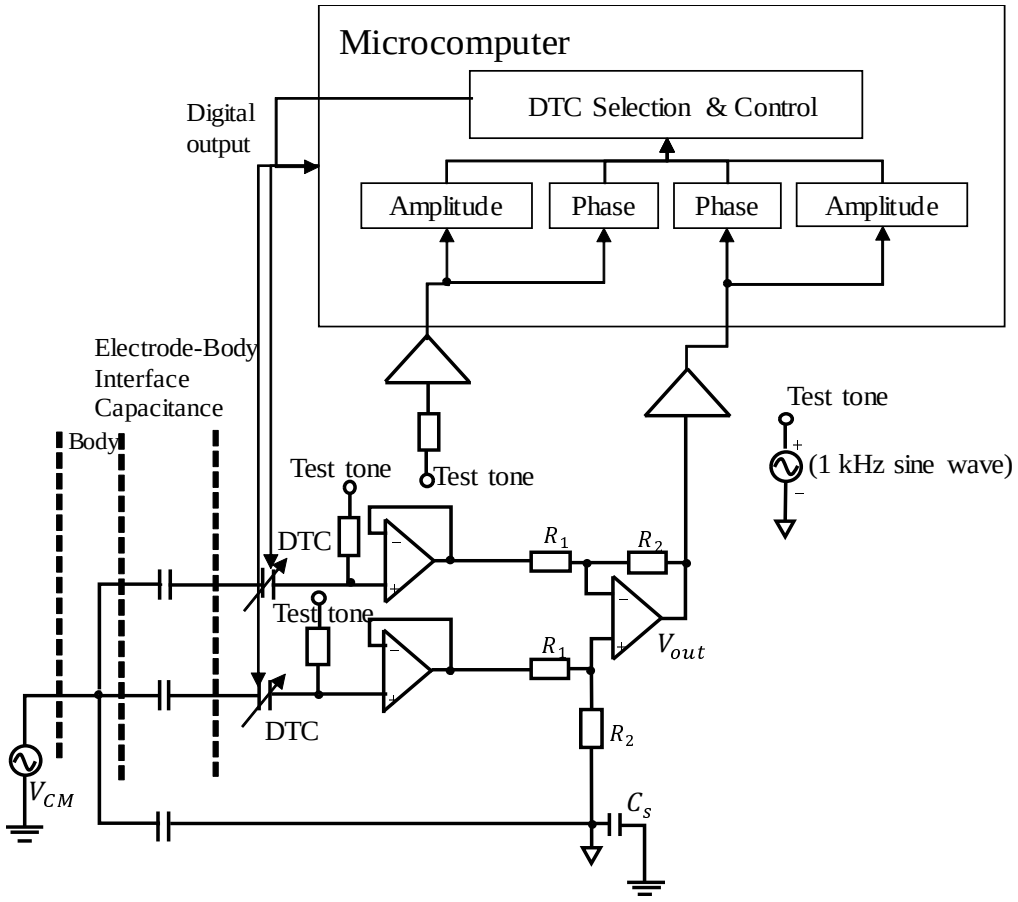

Fig. 3.16. Configuration of the evaluative board with a microcomputer

We use two sets of ceramic capacitors to simulate the EBI capacitance. A sine wave of 1 V, 60 Hz as a pseudo CM noise source V_{CM}, which was generated with a function generator. The chip capacitors in the DTCs are soldered on the backside of this board. We first used some ceramic capacitors, or we call them as "ordinary capacitors", instead of DTCs to exactly cancel the imbalance, to see how much the CM noise is reduced when our design works with no need to worry about the digitally tuning part.

Fig. 3.18 shows the CM noise reduction efficacy when ordinary capacitors are

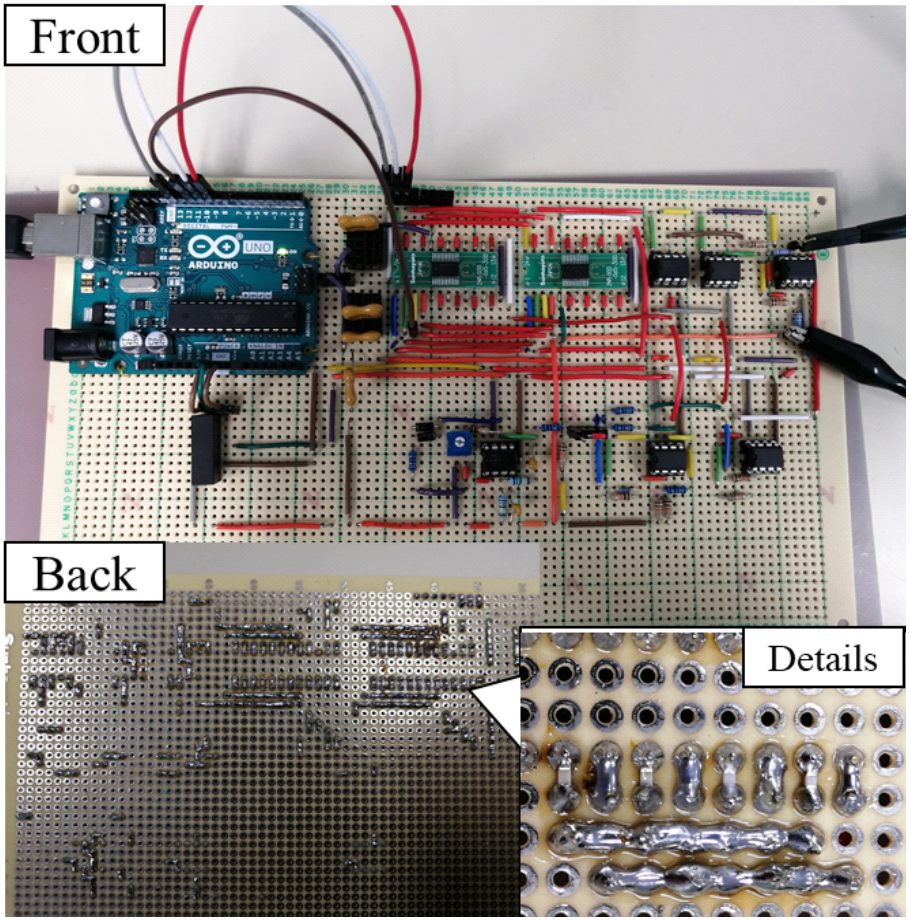

Fig. 3.17. Evaluation circuit on a universal board. We use two sets of ceramic capacitors to simulate the EBI capacitance. The chip capacitors for constructing the DTC are soldered on the back side of the board.

used to cancel the imbalance. We can see from this figure that when the imbalance is cancelled, the noise output from our evaluation board remains at a low level, around 60 mV. The noise level can be driven down by about 30 dB when the imbalance is as large as 200 pF. This result generally matches our simulation result, and the remaining noise voltage could be from the other parts of the circuit like the amplifiers.

Fig. 3.19 shows the experimental evaluation result of our originally constructed DTC. We have tried several kinds of analog switch array elements, among them

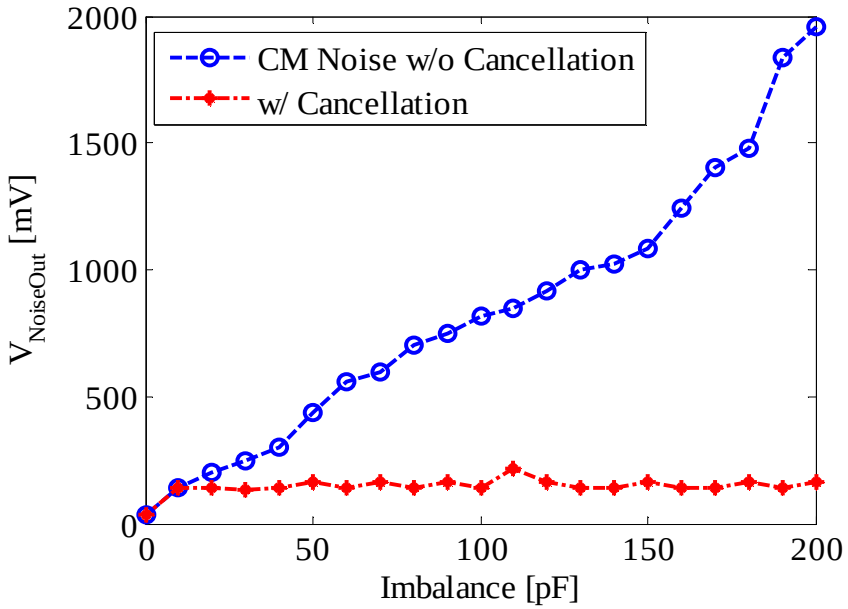

Fig. 3.18. Noise reduction efficacy of our approach. The noise source is a 1 V, 60 Hz sine wave. The blue circled line is the CM noise output when the imbalance is forced in the capacitors emulating the EBIs; the red dotted line is the result when the imbalance is overcame by means of appropriate selection of ordinary capacitors (manually).

ADG512 (Analog Devices) and MAX335EUG+ (Maxim Integrated) are chosen because their features fit our demands best. Parameters of the two chips are shown in Table 3.5. They can both run with ± 5 V voltage supply, and the channel number of ADG512 is 4 while MAX335EUG+ has 8 channels. The channel on-capacitance and channel off-capacitance are two important parameters, because during our test we found that they decide the equivalent capacitance of each channel. For example, the tuning step of the DTC using the ADG512 is about 24 pF, which is near to the difference between the channel on-capacitance and channel off-capacitance. The reason why it is smaller than (35 pF $-$ 24 pF) is because we connected a capacitor in serial with it, to make the circuit more stable. In a word, the structure of CMOS limited its tuning step range.

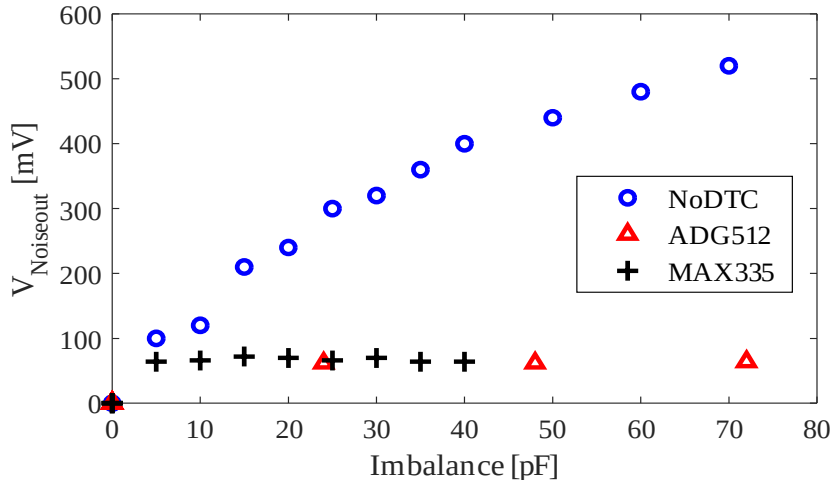

Fig. 3.19. Experimental result of noise reduction efficacy using DTCs. ADG512: 4 tunable steps, about 24 pF for each step; MAX335: 8 tunable steps, about 6 to 8 pF for each step.

Table 3.5. Parameters of ADG512 and MAX335EUG+

	ADG512	**MAX335EUG+**
Voltage Supply	±5 V	±5 V
Number of Channels	4	8
Channel On-Capacitance	35 pF	8 pF
Channel Off-Capacitance	9 pF	2 pF

From Fig. 3.19, we can see that the equivalent capacitance of each channel is about 24 pF when we use the ADG512 chip. The tunable range of DTC using ADG512 is up to 96 pF, approximately. However, as we used one of its channels as a switch (no capacitor connected to this channel), making the actual upper limit about 75 pF (approximately 3 × 24 pF). This value can change due to the circuit implementation and the chip capacitor we connected to it. On the other hand, MAX335EUG+ has 8 channels but the channel on-capacitance is about 8 pF. This makes the tunable range of our MAX335EUG+ version of DTC only able to be tuned up to around 50 pF. Because we used one of its channels as a switch, the

actual upper limit is about 42 pF (7 × 6 pF). According to our measurement, the equivalent capacitance of each channel is about 6 to 8 pF, which was hard to be exactly measured because it is quite a small value. Moreover, we can only give the results in tens of picofarads order in Fig. 3.19 in the same reason. The actual performance of our approach could still be significantly improved when better DTCs are employed in the circuit.

3.5 Conclusion and our contribution

Noncontact/capacitive biopotential sensing technology has a great future in medical treatment, healthcare and new applications with wearable technology. The disadvantages of the contact electrodes, about comfort and longevity, can be solved by insulated biopotential sensing technology, but common-mode noise rejection is still a challenging task for noncontact electrodes. In this work, we have presented an approach to reduce the CM noise output of a noncontact biopotential acquisition circuit (analog-front-end), which works through cancelling the imbalance of EBI capacitance with DTCs. At first, we provided a circuit model of noncontact biopotential acquisition, and analyzed our proposal through calculations and simulations. We clarified how much influence an imbalance in the EBI could have for a typical biopotential acquisition circuit, showing that our proposal is feasible by simulation results. We also made a comparison with another circuit design, showing the frequency sweep result of both circuits. Based on the simulation results, the first proposal we called as "DTC series" was our last choice. Secondly, we proposed the design that uses a microcomputer together with originally designed DTC to cancel the imbalance. The performance of this design was evaluated on a circuit board in experimental environments. When ordinary capacitors are used for evaluation, the result showed that the CM noise level can be driven down by about 30 dB when there is an imbalance of 200 pF, which

matches our simulations quite well. However, the tunable range and resolution of the DTC is still a problem.

It is a fact that some existing tunable capacitor elements has almost the same design as our DTC. However, the novelty of our design still lies in its advantages of realizing good digital tunability and availability in our EBI imbalance cancellation circuit. In the future, we expect that new design of DTC with better linearity, larger capacitance variation and better tunability can improve the performance of this design. Embedding a tunable capacitor to make a new type of noncontact electrode is also in our vision.

Asides, the analog-front-end of our design have very large input impedance and low current. The main energy cost is from the microcomputer, whose power consumption can be driven down to as low as 23 μA with 5V power supply, in power-down sleep mode. DC power supplies of the analog elements are all provided by the microcomputer.

In summary, we presented a novel approach to reduce CM noise for noncontact biopotential acquisition, which could help supporting long-term, comfort and precise applications of wearable devices, human-computer interface or IoT (Internet of Things).

Chapter 4

EBI Impedance Imbalance Monitoring Strategy

4.1 Overview

In last chapter, we showed that if the imbalance of EBI impedance is compensated or cancelled successfully, the noise output of a CM interference voltage will be rejected to very low level. In order to realize this, we need to detect how much imbalance exists at the EBI. Continuously monitoring scheme for EBI impedance imbalance can help making the acquisition circuit smarter, such that irregular change in EBI impedance can be cancelled in time. Therefore, good imbalance monitoring scheme can solve real-time using problems about longevity and stability. If these two problems are solved, further advance for healthcare or activity recognation applications, especially those with wearable sensing technologies, can be expected in near future. The real-time monitoring of the imbalance also helps in rejecting the artefacts, which will be discussed in the next chapter.

In this chapter, we introduce our EBI impedance imbalance monitoring strategy. Circuit analysis and simulations are performed to show the effectiveness of our approach. The digital processing part and DTC selecting algorithm, including how we process the DTC controlling in the microcomputer is also presented in this part. Experimental evaluation results revealed good precision and linearity of our approach.

4.2 Related previous studies

In [25], the input voltage at the EBI was employed to detect the CM voltage level. In their method, the two input voltages of a differential amplifier were separately monitored and the amplitude was use for both deciding whether the CM noise level is high enough and which impedance at the EBI is larger. One disadvantage of this method is that when the biopotential is high enough, the system will wrongly believe that the CM noise level is high, because in their approach a noise input cannot be separated from a DM signal voltage. We avoid this problem by using an independent injection sine wave signal. Because that the sine wave can be easily filtered from other voltage components, the interference from the biopotential can be avoided.

In [53] and [58], Degen and Chi et al. mentioned the relation between the CMRR, input impedance of amplifier and the EBI impedance imbalance. Looking the whole biopotential acquisition circuit as one amplifier, we can calculate the imbalance using the total CMRR and the input impedance. However, because a change in EBI impedance causes a change in CMRR, it is hard to calculate the CMRR unless we append another buffering electrode to get the approximate potential of the human body surface, which also brings an error to the result. The precision of input impedance calculation is another challenge. [63] proposed an approach to exploit an injection signal to track the capacitance change of EBI and restore the ECG signal through digital processing. Their approach inspired us of how to monitor the imbalance change at the EBI, but their work did not solve the CMRR loss problem caused by imbalances in other elements.

4.3 Circuit analysis

This section explains how we use an 1 kHz, 100 mV sine wave, which is also called as a "test tone", to monitor the EBI impedance imbalance through circuit analysis. Fig. 4.1 shows how the test tone is injected into the circuit. In this circuit we take the noncontact conditions, and the contact case can be derived easily from the result. Parameters of the circuit elements are the same as the parameters of DTC series in Chapter 3. The test tone is injected at the positive input of the buffer, passing a resistor R_T, whose resistance is 100 KΩ.

In this circuit, we can cut off the differential amplifying part behind the notes V_a and V_b and analyze the correlation between $\mid V_a - V_b \mid$ and the test tone, because $\mid V_a - V_b \mid$ linearly decides the DM voltage output converted from the CM noise source. After cutting off the amplifying part and ignoring C_{t1} and C_{t2} temporarily, equivalent circuit of this injection model becomes what is shown in Fig. 4.2.

In Fig. 4.2, V_T stands for the test tone voltage source. let

$$Z_a = R_T + \frac{1}{j\omega C_{ea}} \tag{4.1}$$

$$Z_b = R_T + \frac{1}{j\omega C_{eb}} \tag{4.2}$$

which are the two impedances at the two circuit branches. Using these two impedances we can express $V_a - V_b$ as

$$V_a - V_b = \frac{R_T(Z_a - Z_b)}{(Z_a + Z_b)\frac{1}{j\omega C_{ex}} + Z_a Z_b} V_T \tag{4.3}$$

Bring C_{ea} and C_{eb} back to (4.3) again and get the absolute value, we have

$$|V_a - V_b| = R_T V_T \frac{|j\omega(C_{ea} - C_{eb})|}{|\frac{1}{j\omega C_{ex}}[j\omega(C_{ea} + C_{eb}) - 2\omega^2 R_T C_{ea} C_{eb}] + 1|} \tag{4.4}$$

Under the parameters of the biopotential acquisition, (4.4) expresses an approximately linear correlation between $|V_a - V_b|$ and $|C_{ea} - C_{eb}|$. In order to confirm this fact, we

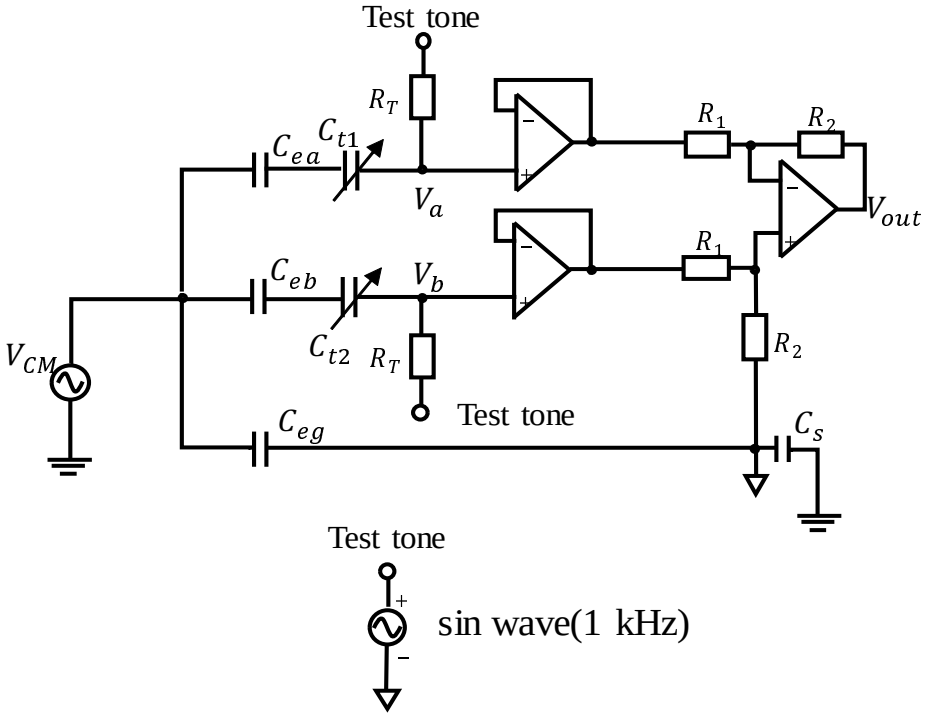

Fig. 4.1. Injection model of the test tone

make a comparison between the plot of $|V_a - V_b|$ from (4.4) and circuit simulation result of $|V_a - V_b|$ from the original circuit in Fig. 4.1 (V_{CM} is zero and C_{t1}, C_{t2} are not included). The result is shown in Fig. 4.3. We can see from Fig. 4.3 that the two results match quite well. This result reveals that $|V_a - V_b|$ can track the change of EBI impedance imbalance quite well. Therefore, we can read the output of the test tone at V_{out} and monitor the imbalance in good linearity.

4.4 Wien Bridge Oscillator

Considering about applying our design in a wearable device, it is not very convenient to inject the 1 kHz, 100 mV test tone from outside. In order to produce the test tone inside the circuit board, we designed a Wien Bridge Oscillator circuit. A Wien bridge oscillator is a type of electronic oscillator that generates sine waves. It can be used to generate a large range of frequencies. The circuit

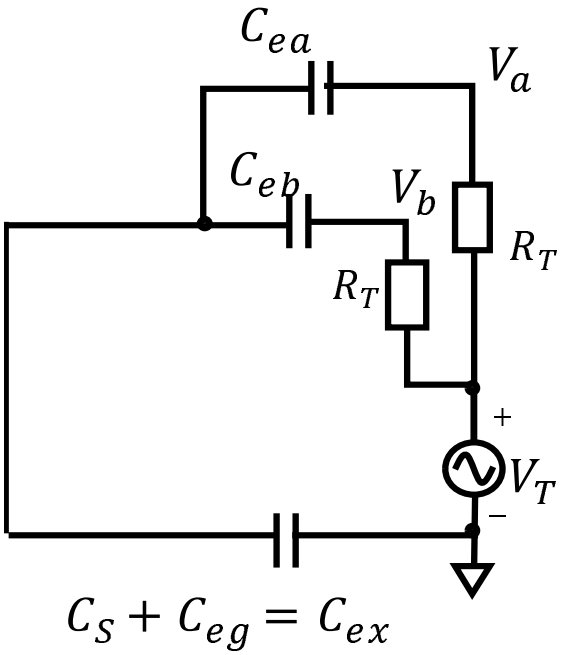

Fig. 4.2. Equivalent circuit of the injection model

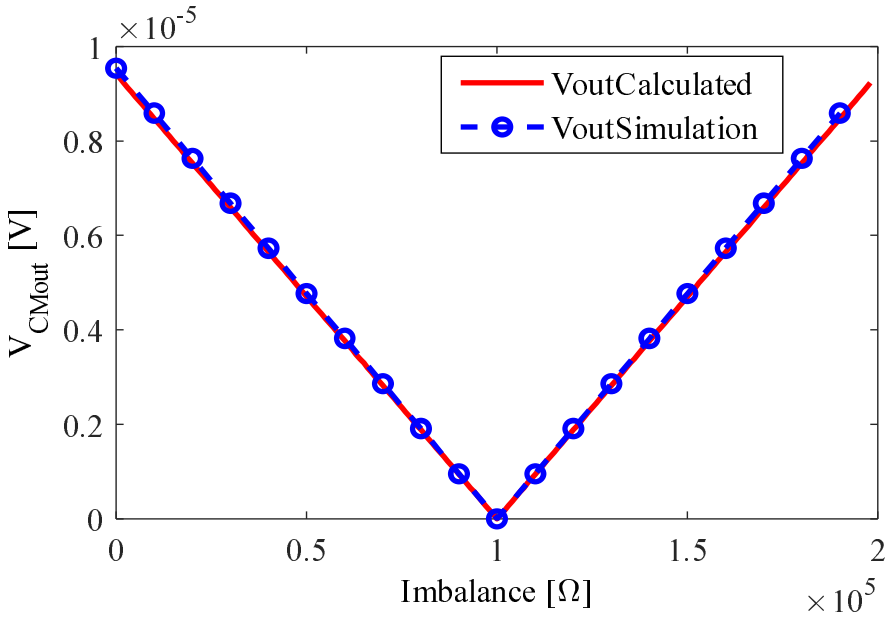

Fig. 4.3. Comparing the plot of $|V_a - V_b|$ from (4.3) and circuit simulation result of $|V_a - V_b|$ from the original circuit

design of our Wien Bridge Oscillator is shown in Fig. 4.4. Except for the stabilizing part, the bridge comprises four resistors and two capacitors. The oscillator can also be viewed as a positive gain amplifier combined with a bandpass filter that provides positive feedback. Automatic gain control, intentional non-linearity and incidental non-linearity limit the output amplitude in various implementations of the oscillator.

In Fig. 4.4, V_{out1}, V_{in1}, V_{out2} and V_{in2} has the following relation:

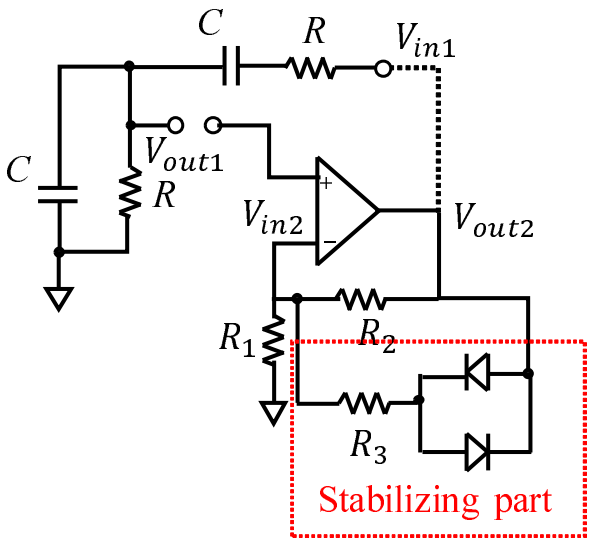

Fig. 4.4. Wien Bridge Oscillator circuit design

$$V_{out1} = \frac{1}{3 + j(\omega RC - \frac{1}{\omega RC})} V_{in1} \tag{4.5}$$

$$V_{out2} = \frac{R_1 + R_2}{R_1} V_{in2} \tag{4.6}$$

(4.5) and (4.5) explains how the Wien Bridge Oscillator makes a sine wave through the resonance of the RC circuit part and the amplifying part. By selecting proper values of R, C and R_1, R_2, we can get a 1 kHz, 100 to 300 mV tunable sine wave to be used as the test tone.

The stabilizing part denoted in Fig. 4.4 is significant to make the output stay at

a certain level. When the amplitude of the oscillated sine wave is too small, the two diodes can be seen as disconnected. On the other hand, if the amplitude is high enough, the diodes are turned on, making R_3 connected with R_2 in parallel, such that the amplitude is stabilized. Without this part, the Wien Bridge Oscillator could fail to work because of the error or deviation of the circuit elements' real value.

4.5 DTC controlling scheme in the microcomputer

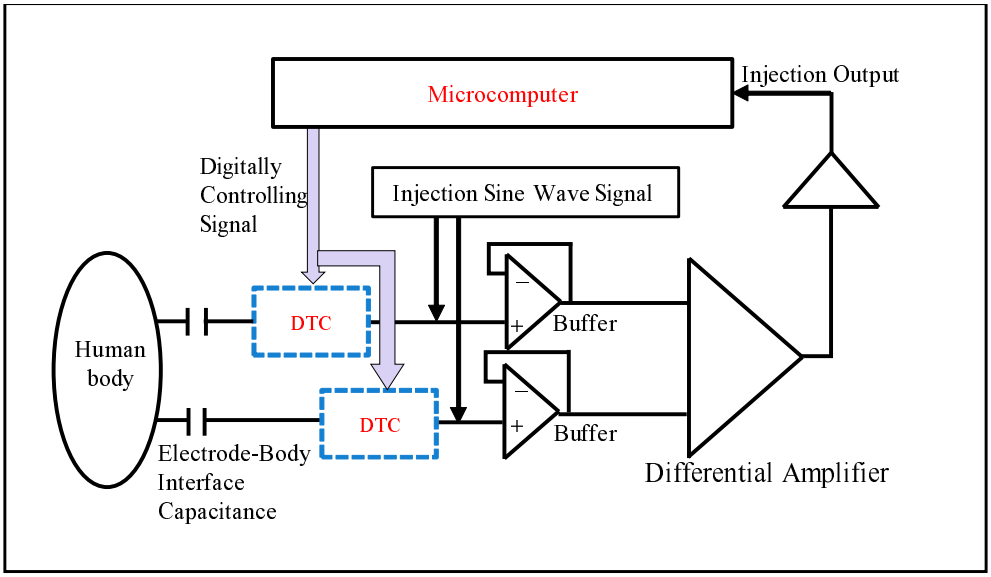

Fig. 4.5. DTC controlling scheme configuration

In Chapter 3, the configuration of our CM noise reduction system employing a microcomputer was presented. Fig. 4.5 is a clearer version of it to show the DTC controlling scheme. In the last section, we explained about reading the output of the test tone to track the imbalance change at EBI. Because that the output of the test tone is at 1 kHz, we can get this signal rightly by passive filtering. The signal is then read by the microcomputer after a shifting buffer, which shifts the signal to a range of 0 to 5 V linearly, such that the microcomputer can read it.

After that, the phase information of this signal is calculated by comparing with the input of the test tone. We can know which capacitance (C_{ea} or C_{eb}) is larger by comparing the phase, because it reverses by 180 degree depending on C_{ea} or C_{eb} is larger. Moreover, as we mentioned previously, the amplitude of the output tells us absolute value of the imbalance. Fig. 4.6 shows the flow chart of our imbalance

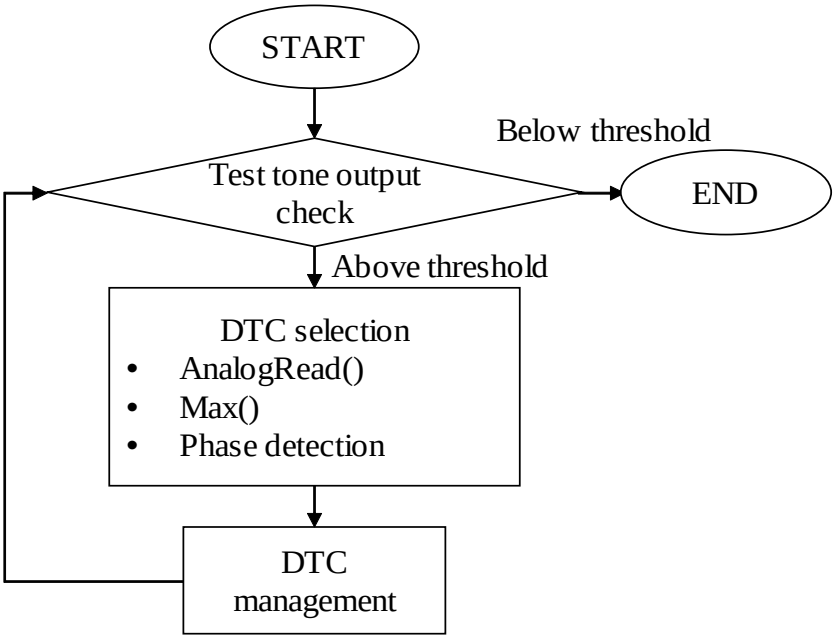

Fig. 4.6. Flow chart of the imbalance detection and DTC management algorithm

detection and DTC management algorithm. A threshold value of test tone output was used to trigger the DTC tuning operation. When the output of test tone signal increases to high level, the microcomputer reads in the input and output of the test tone, from the two ports of our biopotential acquisition circuit shown in Fig. 3.16. After that, values of the phase and amplitude are employed to help tuning the DTCs as we mentioned earlier. Lastly, we check the output of the test tone again to confirm that the imbalance cancellation is successful. This loop is supposed to be performed in the microcomputer continuously when actually used

because we expect that the CMRR can be restored automatically during actual use. Time cost of one detection loop is about 200 ms.

Specifically, at the "DTC selection" part, we figure out which EBI impedance is smaller. And then, we tune the DTC connected to the smaller one step by step, until the test tone output becomes smallest value at the "DTC management" part. The other DTC is also tuned in the same way. Calibrations can be performed before this process, because with the linear like correlation between the imbalance and the test tone output, the algorithm can function more accordingly.

4.6 Experimental evaluation

The experimental evaluation was performed on our evaluation circuit board. The 1 kHz, 100 mV test tone was produced by the Wien Bridge Oscillator, continuously flowing through the board. EBI impedance imbalance was changed step by step, and the output of the test tone was measured with an oscilloscope every time. Fig. 4.7 shows the result, the correlation between the imbalance and the output of the injection signal. From this figure we can see that they are almost linearly related in our experimental environments. When the absolute value of imbalance increases, the output voltage of test tone increases linearly. This property also matches our circuit simulation result. Because that some error always exists in the circuit elements, the plotted output voltage line is not so straight as our simulation result.

4.7 Conclusion and our contribution

To rightly and continuously monitor the EBI impedance imbalance is an important task. At this chapter we discussed the principles and performance of our EBI impedance imbalance monitoring scheme. Simulated and experimental results showed good linear correlation between the imbalance and the test tone output.

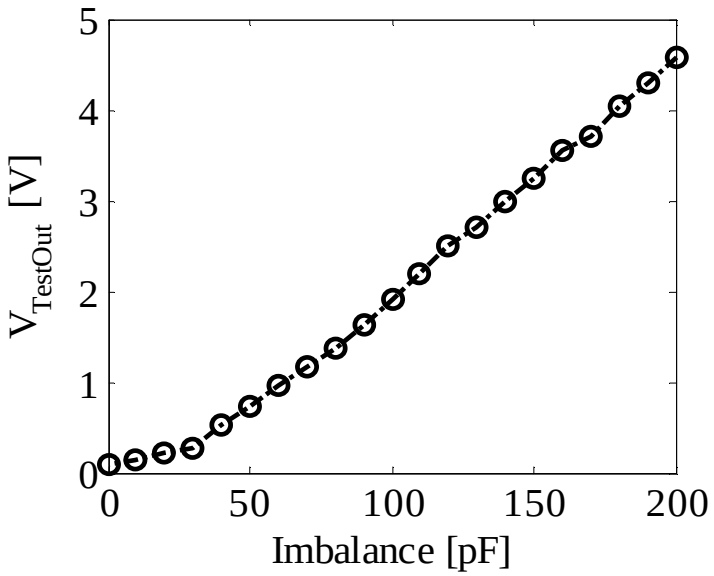

Fig. 4.7. Correlation between the imbalance and the output of the injection signal

A DTC selecting and controlling algorithm was also briefly described. Except for this approach, we have also considered about others that could be smarter and more effective, for example, completely analog circuit designing for monitoring and reacting to the EBI impedance change. However, pure analog design is quite challenging to achieve high precision and stability. Communication speed between the DTC and the microcomputer is limited by the DTC structure (depending on the interface). The microcomputer could also affect power consumption and the size of the circuit. The main contribution of this part's work lies in developing the injection signal based imbalance monitoring sheme. We hope that a more suitable DTC chip that meet all the terms for our application could emerge in future.

Chapter 5

An Advanced Ideology and Application: Imbalance Cancellation based Artefact Solution

5.1 Overview

In Chapter 1, we have introduced that the artefacts which are superimposed to the biopotential signal could happen for complicated reasons. Because that some kinds of artefacts causes EBI impedance change and the others do not, they can be analyzed in different approaches.

In this chapter, we will present that some artefacts have CM voltage component just like an external interference voltage. On the other hand, some other artefacts cause EBI impedance change and reduce the total CMRR of the acquisition circuit.

We firstly analyze the relation between the artefacts, CM noise and EBI impedance imbalance. We introduce our work on EOG artefact solution to reveal some principles and mechanisms about the EOG artefacts. The properties that EOG signal and ocular artefacts have would also help in explaining our idea about the relation between the artefact and the CM noise. In order to present the generalized principles, properties of ECG and EEG artefacts will also be briefly analyzed.

After introducing the properties of biopotential artefacts, we divide them into two types: artefacts that cause EBI impedance change and those do not. By

performing experimental evaluations, we explain our idea about suppressing the CM noise voltage caused by artefacts. Experiment verification was performed, and the result showed that our idea of imbalance cancellation based artefact solution is feasible.

5.2 Theoretical analysis using EOG artefacts

EOG artefacts were introduced in Chapter 1. In our work [29], detection algorithm based approaches to reject EOG artefacts was introduced, which could help achieving better eye movement detection for EOG-based HCI applications. Fig. 5.1 shows the configuration of our EOG acquisition system. Fig. 5.2 shows the arrangement of electrodes for acquiring the horizontal EOG signal (EOG_h). It can be acquired by the system through electrodes placed on either side of the eyes. The potential picked up by electrode is digitally modulated after A/D (analog-to-digital) conversion and sent to a PC through a 2.4 GHz wireless telemeter unit. In the PC, we have developed a data processing and recording program with NI LabVIEW 2012. A 0.1∼10 Hz band pass filter, with a sampling frequency of 128 Hz, was used to remove the Gaussian noise while achieving an AC acquisition [42] of EOG signal.

EOG waveform example is shown in Fig. 5.3. During the acquisition process, the subjects are instructed to conduct a set of specific eye motions which was composed with three visual actions: saccadic movement from center to target on right side at 10°, 20°, 30°, 40°, 50°; fixation on the target for about 1 second such that the amplitude returns to zero; backward saccade to the center position. We can see that the correlation between EOG amplitude and gaze angle is almost linear. Fig. 5.4 shows the fitting curves with the experimental data of 6 subjects. This result also reveals how the EOG amplitude changes when there is an eye movement.

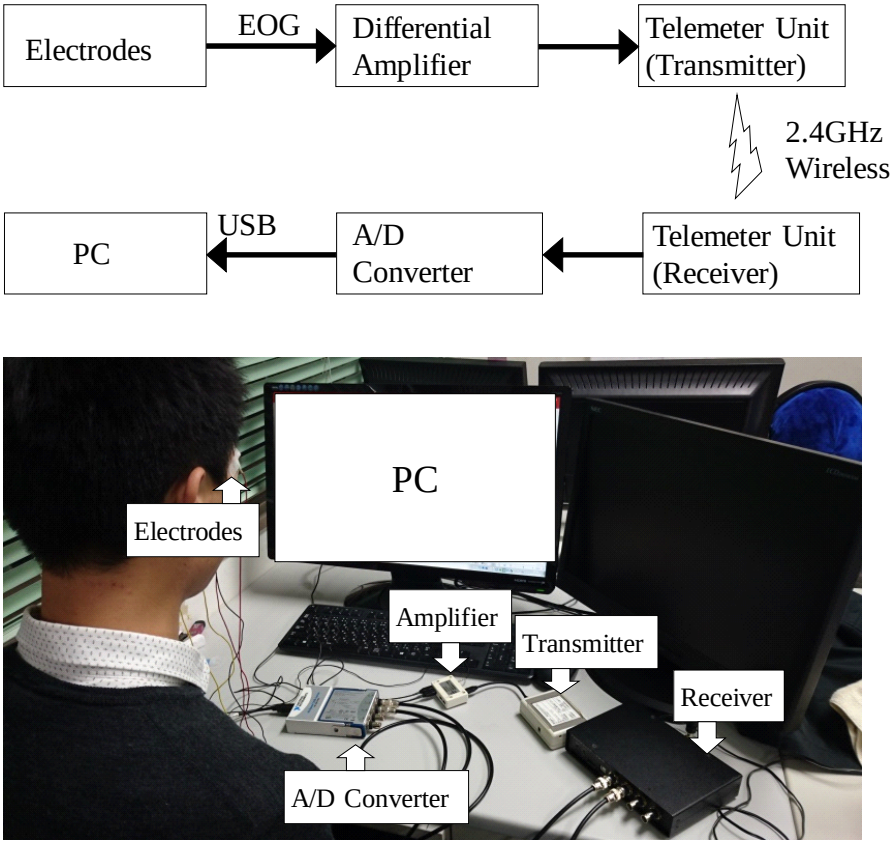

Fig. 5.1. EOG acquisition system

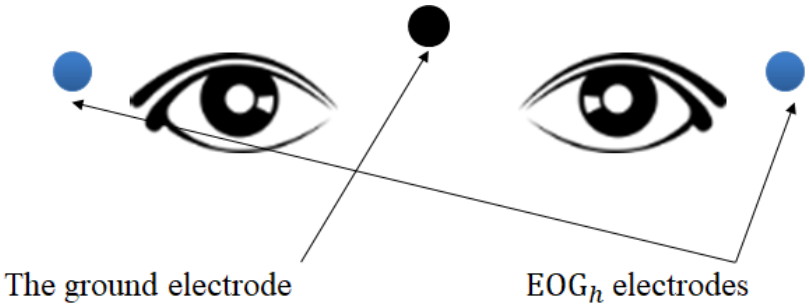

Fig. 5.2. Arrangement of electrodes

The acquisition process of EOG has some special properties. As is shown in Fig. 5.2, the electrodes are attached on each side of subject's head symmetrically. This property makes the EOG acquisition picks up almost the same shape of voltage

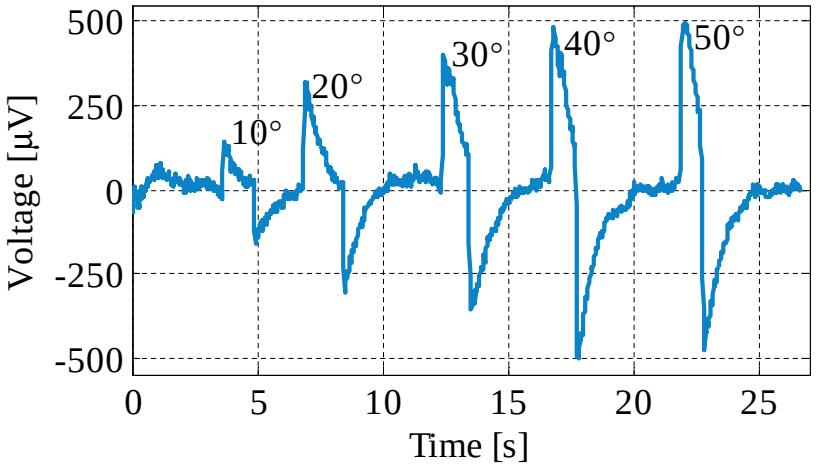

Fig. 5.3. EOG waveform of saccades (gaze angle: 10°, 20°, 30°, 40°, 50°)

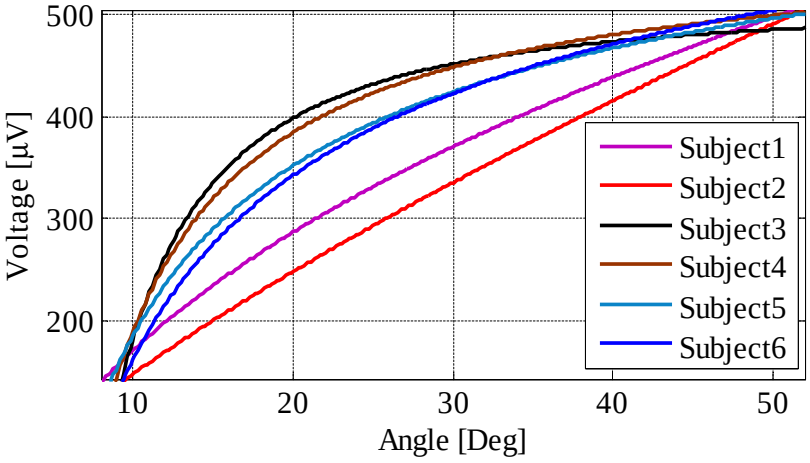

Fig. 5.4. 6 subjects' EOG amplitude vs. gaze angle fitting curves

waveform at each side. If we measure the EOG waveform on each side of the head separately, we can see that the EOG waveform looks quite alike, but one side is positive potential while the other side is negative. Fig. 5.5 shows the electrical model of an eyeball, which could be simply seen as a electrical bipolar. When a person looks left or right, the EOC electrode on the side of head can detect the potential change caused by the rotation of eyeball. This fact tells the reason of

why the EOG waveforms picked up by the single electrode on each side of the head are symmetrical.

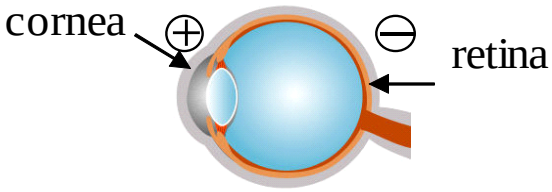

Fig. 5.5. Electrical model of an eyeball

According to the same reason, artefacts picked up by a single electrode on each side of the head could be almost the same. Fig. 5.6 shows two EOG artefacts caused by the eyelid muscles: one by eyelid fatigue, and the other by a blink after a saccade. These two artefacts have almost the same shape when superimposed on an EOG waveform due to the symmetrical arrangement of EOG electrodes, because the eyelid moves in vertical direction. In order to confirm this idea, we check the waveform separately on each EOG electrode.

Fig. 5.7 shows the arrangement of the electrode to respectively acquire the left and right EOG artefact in the confirming experiment. We paste one of the EOG electrodes on the left or right at one time, and the other electrode is pasted at almost the same place as the ground electrode. The subjects blink several times in each measurement, and Fig. 5.8 shows the waveforms we acquired. We can see that the shape of a blinking waveform looks like to others. The difference in amplitude is caused by the power use of the eyelid muscle. In this kind of case, the artefact can be seen as a CM voltage component, because it matches the conduction model of CM noise source. However, it is difficult to acquire the same waveform of artefact output, because there always exists some difference between the sensing conditions.

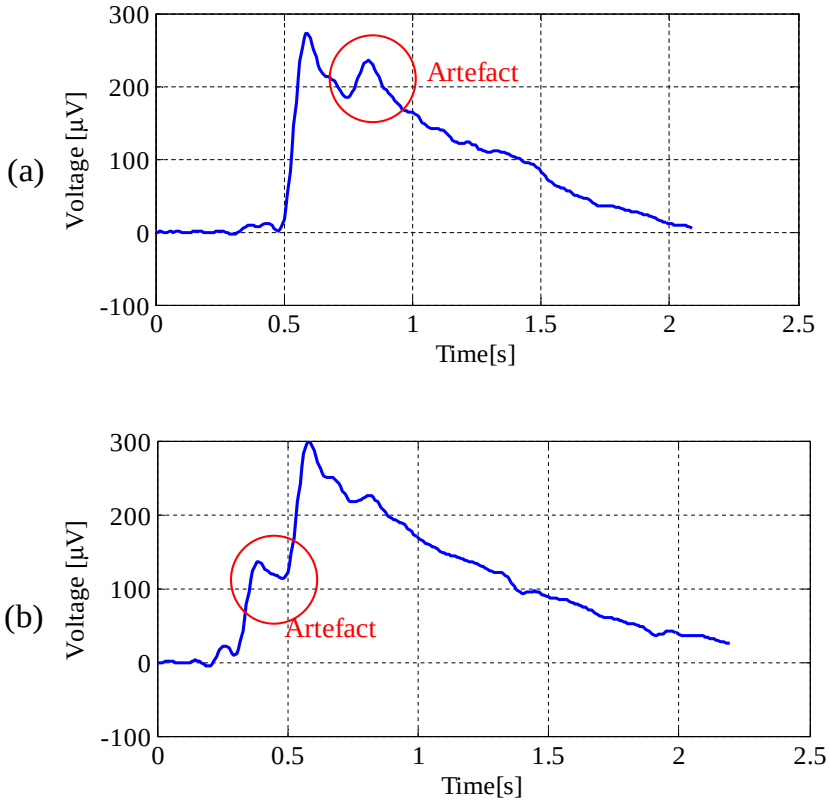

Fig. 5.6. Two EOG artefacts caused by the eyelid muscles. (a) eyelid fatigue, (b) a blink after a saccade.

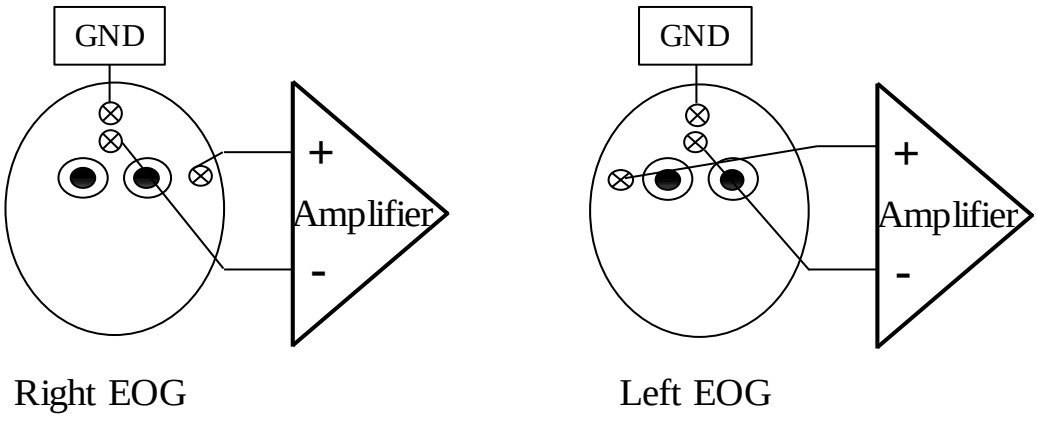

Fig. 5.7. Electrode arrangement for EOG artefact comparison

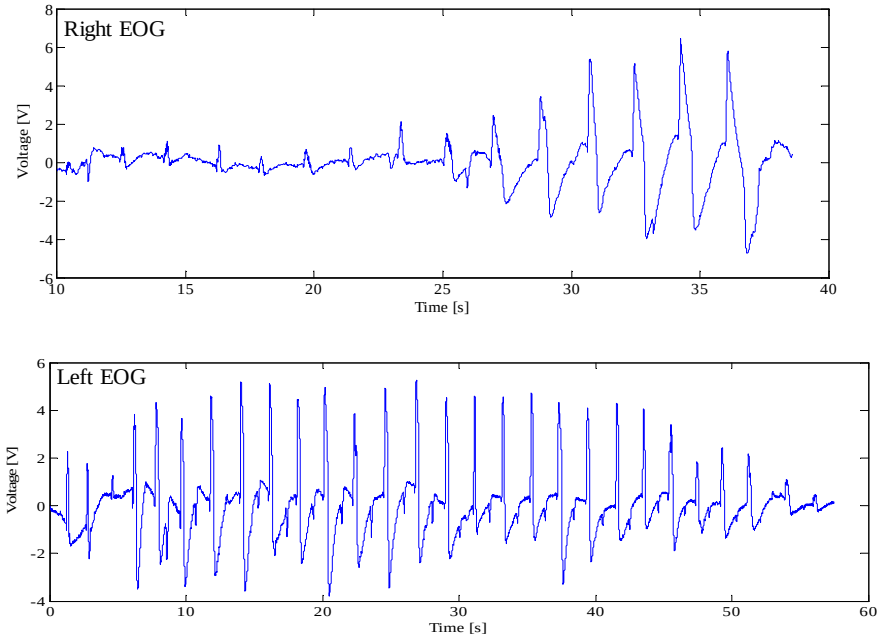

Fig. 5.8. Comparison of left and right EOG artefact

5.3 Dividing the artefacts

At the last part of last section, we proposed the idea that a blink can be regarded as having some CM voltage component. This property also exists in some other artefacts. For example, placement of the EEG electrode could also be symmetrical on the head. When a artefact like a body motion or ocular artefact happens, it could be superimposed to the EEG signal just like the blink in horizontal EOG. Theoretical this type of artefact can be rejected through our imbalance cancellation based CM noise reduction approach. However, we cannot separate the converted DM noise voltage component and the CM voltage at the output of biopotential amplifier, which makes it difficult to evaluate the practical efficacy of this idea.

The type of EOG artefact we discussed do not or only causes some minor change in EBI impedance. Another type of artefact causes significant impedance change. As is introduced in Chapter 1, artefact like a body motion that causes muscle stretching at the EBI could change the EBI impedance. As a result, the

imbalance between them also changes. Talhouet et al. [54] discussed the effect of stretching force to the EBI impedance. Degen et al. [53] tracked the EBI impedance imbalance change when a force is applied to the electrode. As we presented in Chapter 2 and Chapter 3, the noise output changes when the imbalance changes. For this reason, it is possible that this kind of artefact can be rejected by our imbalance cancellation design.

5.4 EBI impedance measurement

In this section, we measure the EBI impedance in experimental environment and confirm the influence of the artefact that causes impedance change. The impedance measurement is performed employing the approach of Spach et al. [65]. Equivalent circuit of this approach is given by Fig. 5.9. The electrode we used are common gel type (contact electrode). In this circuit, let Z be the impedance of the EBI in the center of the arm, we have the following equations which can help calculate Z:

$$Z = \frac{V_{t2} - E_{skin}}{I} \tag{5.1}$$

$$E_{skin} \approx V_{t1} \tag{5.2}$$

$$I = \frac{V_{t2} - V_{t3}}{10\ k\Omega} \tag{5.3}$$

According to [54], the skin surface and stratum corneum could affect the EBI impedance. For confirming the variation of impedance at different place of the skin, we measured different place on the arm, which is shown in Fig. 5.10. The measured impedance is shown in Table 5.1.

Table 5.1. Measured impedance value

Place	1	2	3	4	5	6	7
Impedance(kΩ)	44	6.6	10	12.5	13.2	20	18.6

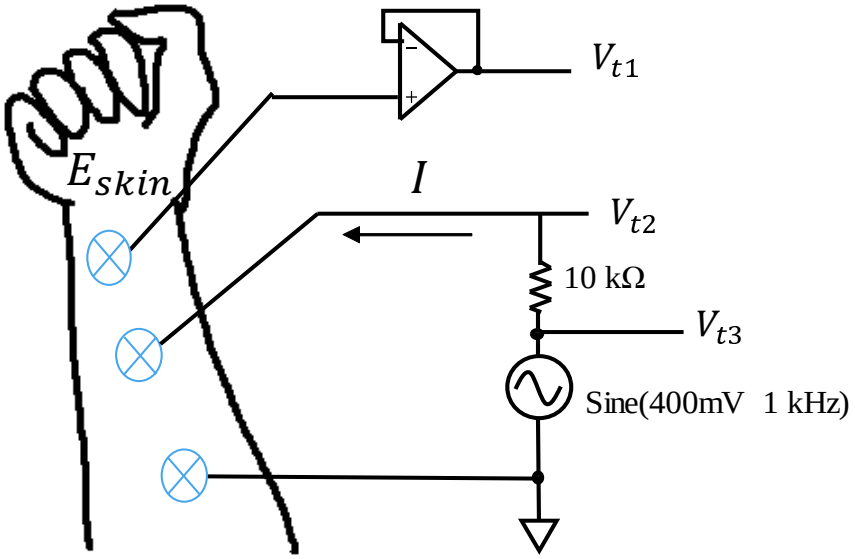

Fig. 5.9. Equivalent circuit of the EBI impedance measurement

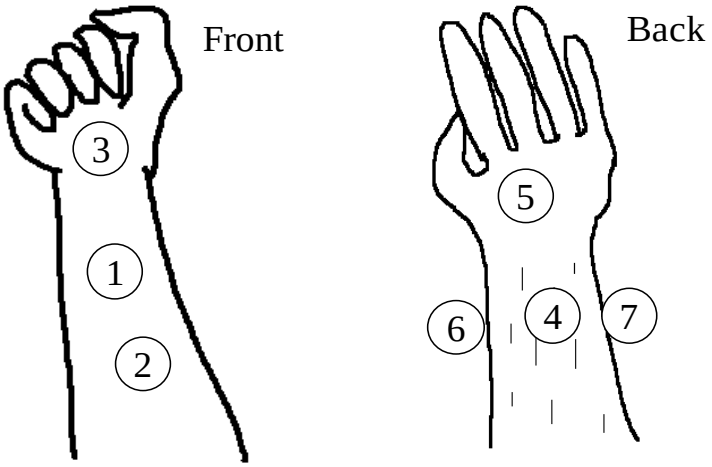

Fig. 5.10. Places for impedance measurement

We can see that the impedance value is about tens of kiloohms order, which is a reasonable range for wet gel electrodes. We also confirmed that sweat and evaporation of the gel has some influence on the results, as we mentioned in Chapter 1. After confirming the EBI impedance, next we try to directly calculate

the EBI impedance imbalance without measuring the impedance at each electrode. The equation for estimating the imbalance from CMRR is given by [53]. Fig. 5.11 shows the equivalent circuit. Let Z_{in} be the input impedance of the amplifier,

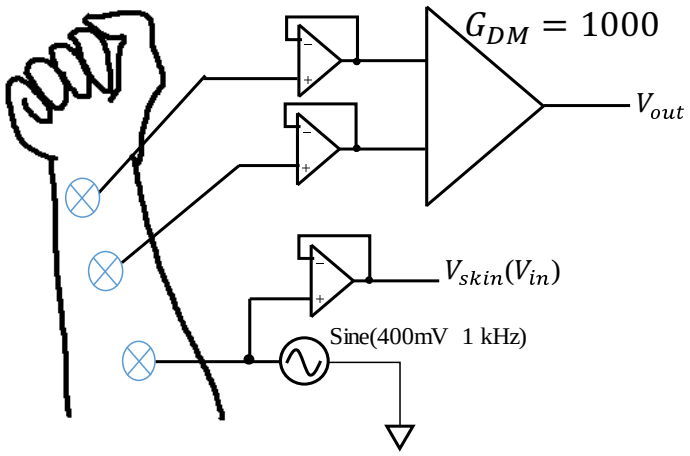

Fig. 5.11. Equivalent circuit of imbalance estimation

which can also be estimated with our previous circuit design for imbalance evaluation using the same equation, imbalance can be written as

$$Imbalance \approx \frac{V_{out} Z_{in}}{V_{in} G_{DM}} \tag{5.4}$$

We use this equation to estimate the imbalance change with or without artefact applied. By measurements, we got the following result shown in Table 5.2. During the experiment, we fix one biopotential electrode, and change the placement of the other one, or use some power to let it loose (Float 1 and Float 2).

From Table 5.2, we can see that when we change the place of one electrode from 1 to 5, there was no much change in the imbalance. This is because that the wet gel electrode has very good attachment, making the imbalance to be quite stable. Besides, the change of imbalance value is quite small. On the other hand, results of Float 1 and Float 2 in the table shows the imbalance change of bad attachment, or influence of a power that can significantly change the attaching

Table 5.2. Measured imbalance

Place	V_{in} (mV)	V_{out} (mV)	Imba. (kΩ)
1	384	44	14.89
2	384	44	14.89
3	384	50	16.92
4	384	46	15.57
5	384	48	16.25
Float 1	384	300	101
Float 2	384	600	203.13

condition. This kind of power or attaching condition could happen frequently for noncontact electrodes. The results revealed that the imbalance cancellation approach may have good performance in preventing CMRR loss caused by this kind of artefact.

5.5 Artefact monitoring with the test tone

Next, we examine if the test tone can be used to track the imbalance change caused by an artefact. Fig. 5.12 shows the equivalent circuit and experimental scenery of artefact monitoring with the test tone. We built the acquisition circuit on a bread board, used wet gel electrodes at the EBI, and checked the test tone output on a PC, where a digital FIR filter of 0.1 to 1000 Hz was applied. We applied 3 different types of artefacts to the electrode and confirm the change in output voltage. Fig. 5.13, Fig. 5.14 and Fig. 5.15 shows the test tone output when the 3 types of artefacts are applied to the EBI: shaking the arm, pushing the electrode with power and peeling the electrode (with light power, not completely peeled off). In Fig. 5.13, we can see that the artefact mainly appears as a DC drift, not causing much change in the amplitude of the sine wave. This is because of the good attachment of the wet gel electrode. In Fig. 5.14, a push to the electrode brings a gradually changing waveform at where the envelope of the output changed

obviously. In Fig. 5.15, because the peeling action made the electrode attachment become loose, a shift in the amplitude can be seen. When we attach the electrode back to the arm (same place), the amplitude maintains at a higher level, due to a change in EBI impedance imbalance. In conclusion, we confirmed from this set of waveforms that using the test tone can detect an artefact that changes the EBI impedance.

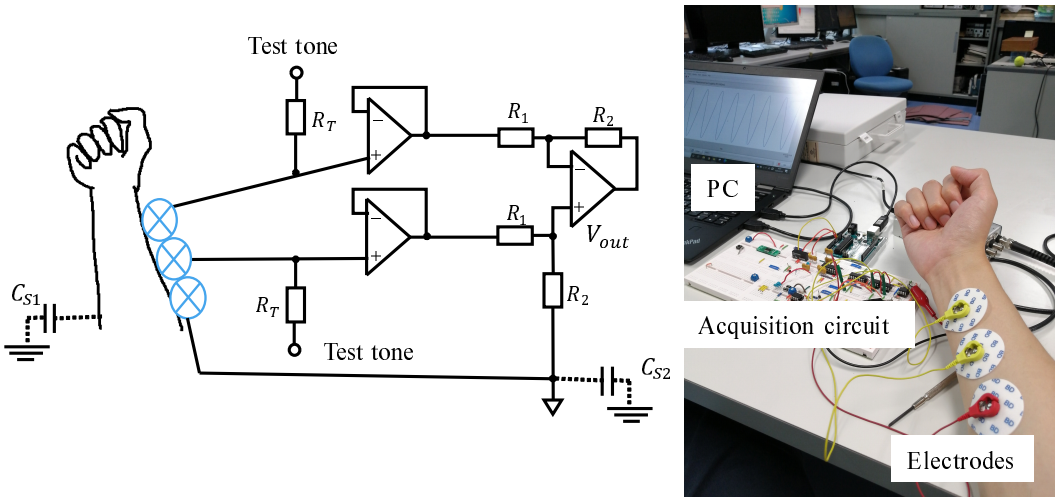

Fig. 5.12. Equivalent circuit and experimental scenery of artefact monitoring with the test tone

5.6 Experimental verification

In this chapter, we present the experimental verification of our idea: imbalance cancellation-based artefact solution. The artefact that we chose was the stretching and withdrawing of forearm. We have made metal electrodes for this verification, because they induce more capacitive component at the EBI than wet get electrodes. Tapes were used to attach the electrodes on the skin surface.

Fig. 5.16 shows the motion of forearm, the metal electrodes we made and their placement. Same as Fig. 5.12, we use the test tone to detect the change in

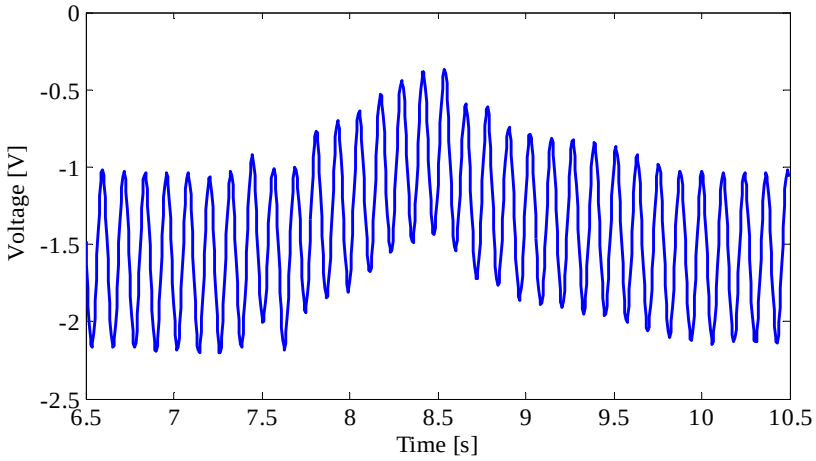

Fig. 5.13. Test tone output change when shaking the arm

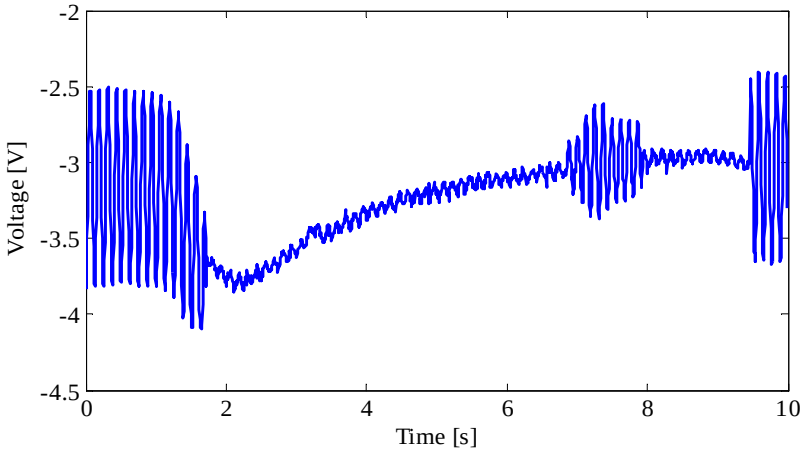

Fig. 5.14. Test tone output change when pushing the electrode

EBI impedance imbalance. When the artefact is applied to the arm, a change in the output of the test tone shows up like Fig. 5.17. We can see that when the forearm was stretched, amplitude of the output voltage became larger, and when the forearm was withdrawn, the amplitude became smaller. The amplitude change is revealing the imbalance change at the EBI, according to our analysis at this chapter.

In order to verify the effectiveness of our imbalance cancellation based idea, we

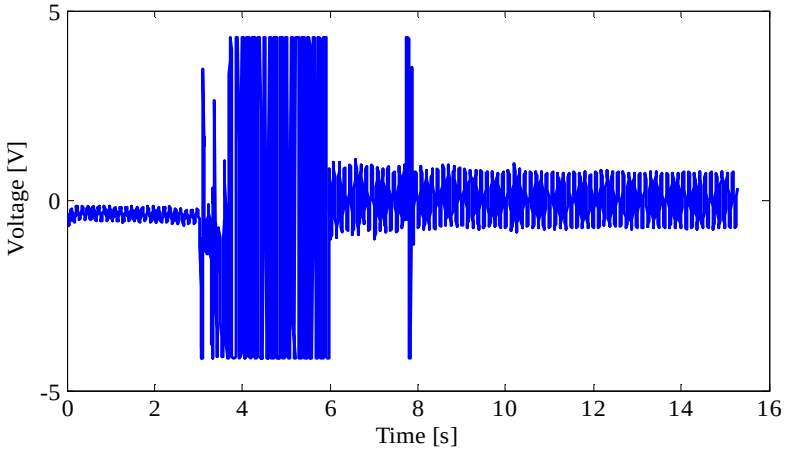

Fig. 5.15. Test tone output change when peeling off the electrode

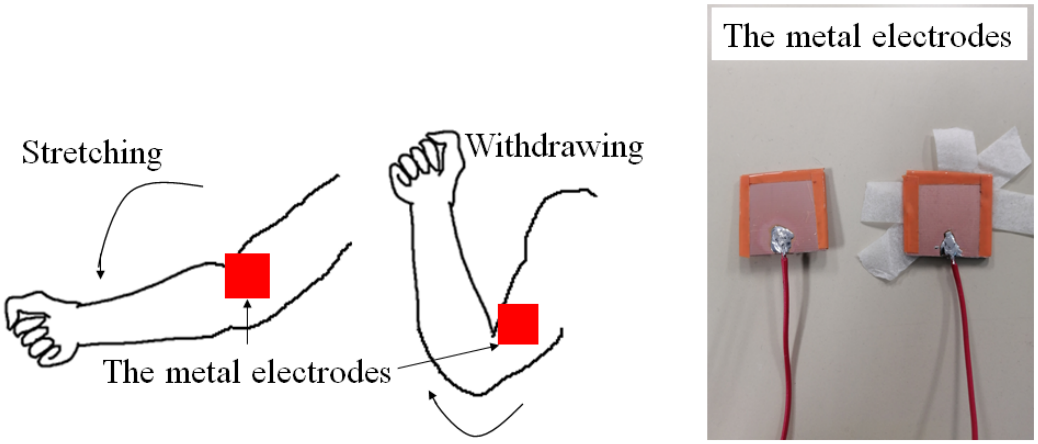

Fig. 5.16. The artefact of stretching and withdrawing of forearm and the metal electrodes

overcome the imbalance by means of appropriate selection of ordinary capacitors (manually) and check the change in test tone output. Fig. 5.18 shows the equivalent circuit of the Experimental setting.

Table 5.3 shows the experimental results. The 2nd and 3rd row shows the test tone output before or after the forearm was stretched, respectively. As we mentioned, this difference in test tone output $V_{testout}$ reveals different level of EBI

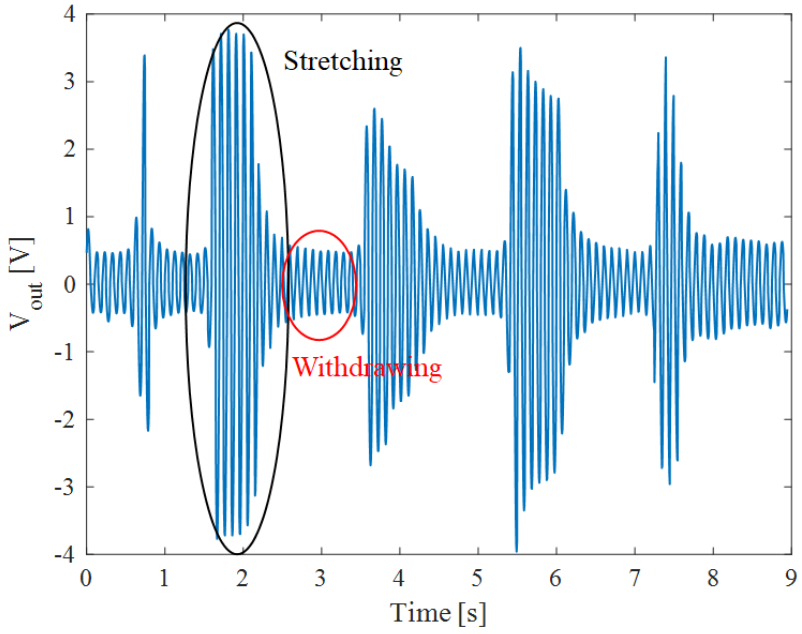

Fig. 5.17. Test tone output voltage change when stretching and withdrawing forearm

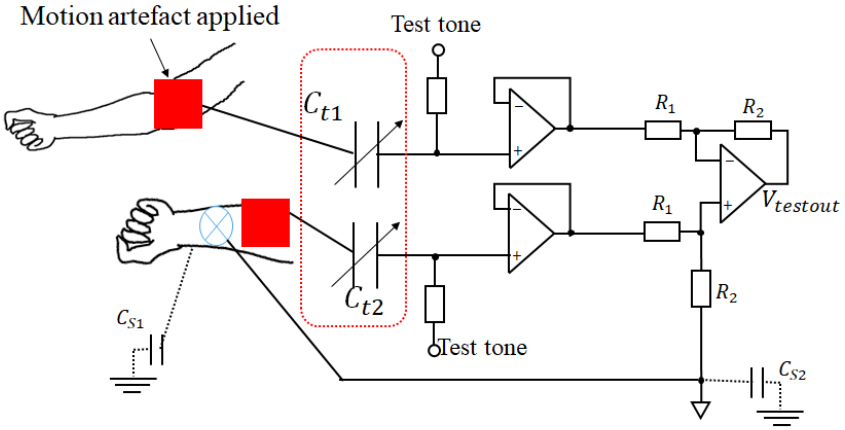

Fig. 5.18. Equivalent circuit of the experimental setting for verifying the imbalance cancellation based artefact solution

impedance imbalance. The 5th row is the amount of cancellation, i. e., difference between the selected capacitors C_{t1} and C_{t2} in Fig. 5.18, whose combination brings

Table 5.3. Experimental results of the verification

$V_{testout}$	Place 1	Place 2	Place 3	Place 4	Place 5
Before stretched	0.5 V	0.3 V	0.32 V	0.1 V	0.12 V
After stretched	3.7 V	1.5 V	1.7 V	0.26 V	0.44 V
After cancellation	0.16 V	0.12 V	0.048 V	0.1 V	0.24 V
Amount of cancellation	20 pF	10 pF	10 pF	5 pF	5 pF

a lowest level that we can achieve when changing the capacitance by every 5 pF. After the imbalance cancellation, the test tone output becomes what is shown in the 4th row. We can see that generally the amplitude of $V_{testout}$ became smaller after cancellation, which means that the imbalance cancellation was successful.

5.7 Conclusion

In this chapter, firstly EOG artefacts caused by eyelid were taken as examples to explain a typical scene in which the artefact can show up as a CM noise source. Secondly, we divide the artefacts into two general types by causing a change in EBI impedance or not. For the artefacts that cause a change in EBI impedance, we measured the EBI impedance and monitored the imbalance change. The results showed that for wet get electrodes, the impedance could be as small as in 10 kΩ order, as was measured by other researchers, and a slight change in contact EBI is hard to detect. However, if we use a power to loosen the electrode, a large imbalance of 100 kΩ to 200 kΩ was observed by our experiment. Thirdly, we evaluated the influence of 3 types of artefacts using the test tone: shaking the arm, pushing the electrode and peeling off the electrode. With a test tone of 400 mV, we succeeded to capture the imbalance change with a voltage output change of several volts. Lastly, we use self-made metal electrodes and performed an experiment to verify the effectiveness of our imbalance cancellation based artefact solution idea. The result showed that with our approach, the imbalance change

caused by a motion artefact can be overcame, such that the noise output can be rejected.

In future work, further evaluation and research on the effectiveness of EBI imbalance cancellation based artefact rejection are in our vision.

Chapter 6

Summary

As the aging society problem draws great attention, the sensing technology and monitoring scheme of biopotential signals has advanced tremendously over the years. The biopotential signals include electrocardiogram (ECG), electroencephalogram (EEG), electrooculogram (EOG) and many others. They are widely employed in medical and healthcare applications. For example, the body area network (BAN) with wearable sensing technologies can collect these signals as vital data for health-state monitoring, which is considered as an emerging solution to soaring healthcare costs and shortages of medical resources. The potential of biosignals is still to be exploited when sensing technologies advance further. In addition to medical treatment and healthcare, they could also be considered as an irreplaceable interface between human body and machines. In the literature, applications like activity recognition, driving assistance or human computer interface were mentioned by researchers.

Common-mode (CM) noise source like the power line, electromagnetic interference (EMI) and artefacts can severely interfere the detection progress of biopotentials. The imbalance of the EBI impedance allows the CM noise converting into a differential mode interference voltage. In this study, a core idea runs through all our works: EBI impedance imbalance cancellation-based CM noise and artefact solution for biopotential acquisition circuits. Contents of the thesis is as follows.

In Chapter 1, we introduced about applications of biopotential signals, noninvasive

electrodes, the two main problems during biopotential acquisition, related previous studies from our group and contents of the thesis.

In Chapter 2, we discussed EBI impedance imbalance cancellation based CM noise rejection for contact biopotential acquisition circuits. Circuit analyzation gave the exact noise rejection performance of a simple differential amplifying circuit, a DRL circuit and a proposed imbalance cancellation design employing digital potentiometers mathematically. Simulation evaluations were performed and the results showing that at 60 Hz our proposal can exceed the performance of a DRL circuit by more than 25 dB in rejecting the CM noise output when the imbalance of EBI impedance is 100 kΩ, and always perform better in an tunable imbalance range of 390.0 Ω to 200 kΩ, with better stability than DRL in biopotential frequency range.

In Chapter 3, CM noise rejection for noncontact biopotential acquisition circuit was discussed. Circuit analyzation and simulation evaluations were also performed, while this time we proposed two different circuit designs at the first place. Simulation results showed the effectiveness of both designs, driving down the CM noise output by more than 60 dB and 150 dB, respectively, when the capacitance imbalance was cancelled. Because that frequency change causes impedance change for capacitance, we evaluated the frequency domain characteristics for them. The results showed that the imbalance cancellation strategy always works well at 0.01 Hz to 10 kHz, which could be considered as a reasonable range for the biopotential signals. After that, we chose the proposal with better performance, built up an evaluating circuit board and performed experimental evaluation on it. The digitally tuned capacitors (DTC) for capacitive imbalance cancellation was originally designed, employing analog switch arrays. Our design realized two kinds of DTCs: one with a 0 to 76 pF end-to-end capacitance, a 24 pF resolution, the other with a 0 to 50 pF end-to-end capacitance and a 6 pF resolution. Both of our design has pure linearity

and digitally tunability. Experimental result showed that at 60 Hz, the CM noise output can be driven down by more than 20 dB when the imbalance is 200 pF, proving the effectiveness of our approach.

In Chapter 4, we proposed an EBI impedance imbalance monitoring method. Experiments are performed and the results showed that the 1 kHz injection signal can track the capacitance change of 0 to 400 pF with good linearity, and the detection process can avoid interferences from the biopotential signal and others.

In Chapter 5, we discussed about the relation between the EBI impedance and a couple of artefacts. Theoretically we analyze why they could be considered as a part of CM noise source and reduce the total CMRR of the biopotential acquisition circuit. Experiments on 3 kinds of artefacts were performed and a change of around 23 dB was observed when there is an interpreted imbalance change of 14 kΩ to 203 kΩ. Experiments to verify our imbalance cancellation based artefact solution idea was also performed. The results prooved that our methodology was practical and further applications in artefact solution could be expected.

To sum up, our main novelty or contribution lies in the following six points:

1) Proposing the comparitive evaluation system with DRL in CM noise reduction, considering fairness, especially influencies of circuit parameters, real acquisition conditions, etc.;

2) Proposing the EBI contact resistance cancellation design using DigiPOTs;

3) Developing of the injection signal based imbalance monitoring scheme, which can solve the interference problems caused by the biopotential, noise, etc.;

4) Expending the approach to noncontact sensing: Theoretiacal analysis, implementation and evaluations, Originally designing and implementing of DTC;

5) Analyzation and evaluation on the relation of artefacts and CM noise, proposing the imbalance cancellation based artefact solution approach.

In the future, we are looking forward to applying the EBI imbalance cancellation to wider range of acquisition scenes, especially for noncontact sensing systems.

References

[1] IEEE Std 802.15.6-2012, "IEEE Standard for Local and Metropolitan Area Networks - Part 15.6: Wireless Body Area Networks," IEEE, 2012.

[2] J. Wang, Q. Wang, *Body Area Communications*, Wiley-IEEE, 2012.

[3] P. Bonato, "Wearable sensors and systems - from enabling technology to clinical applications," *IEEE Eng. Med. Biol. Mag.*, vol. 29, no. 3, pp. 25–36, 2010.

[4] A. Bulling, J. A. Ward, H. Gellersen, G. Trösster, "Eye movement analysis for activity recognition using electrooculography," *IEEE transactions on pattern analysis and machine intelligence*, vol. 33, no. 4, pp. 741–753, 2011.

[5] B. Serkan, E. Sagbas, T. Hokimoto, "The usage of statistical learning methods on wearable devices and a case study: activity recognition on smartwatches," Advances in statistical methodologies and their application to real problems, pp. 259–277, 2017.

[6] R. Nopsuwanchai, Y. Noguchi, M. Ohsuga, Y. Kamakura, Y. Inoue, "Driver-independent assessment of arousal states from video sequences based on the classification of eyeblink patterns," *Intelligent Transportation Systems, 2008. ITSC 2008. 11th International IEEE Conference on*, IEEE, pp. 917–924, 2008.

[7] J. Schmidt, R. Laarousi, W. Stolzmann, K. Karrer-Gauß, "Eye blink detection for different driver states in conditionally automated driving and manual

driving using EOG and a driver camera," *Behavior research methods*, pp. 1–14, 2017.

[8] Z. Lv, X. Wu, M. Li, C. Zhang, "Implementation of the EOG-based human computer interface system," *in Proceedings of the 2nd International Conference on Bioinformatics and Biomedical Engineering (ICBBE'08)*, Shanghai, China, pp. 2188–2191, May. 2008.

[9] R. Barea, L. Boquete, M. Mazo, E. Lopez, "Wheelchair guidance strategies using EOG," *Journal of Intelligent & Robotic Systems*, vol. 34, no. 3, pp. 279–299, 2002.

[10] S. Venkataramanan, P. Prabhat, S. R. Choudhury, H. B. Nemade, J. S. Sahambi, "Biomedical instrumentation based on EOG signal processing and application to a hospital alarm system," *in Proc. IEEE ICISIP*, Chennai, India, pp. 535–540, 2005.

[11] X. Wang, et al., "Performance of Flexible Non-contact Electrodes in Bioelectrical Signal Measurements," *2019 IEEE International Conference on Real-time Computing and Robotics (RCAR)*, Irkutsk, Russia, pp. 17–179, 2019.

[12] M. Chen, et al., "A 400GΩ Input-Impedance, 220MVpp Linear-Input-Range, 2.8Vpp CM-Interference-Tolerant Active Electrode for Non-Contact Capacitively Coupled ECG Acquisition," *2018 IEEE Symposium on VLSI Circuits*, Honolulu, HI, pp. 129–130, 2018.

[13] C. -C., Hsu, B.-S. Lin, K. -Y., He, B. -S, Lin, "Design of a Wearable 12-Lead Noncontact Electrocardiogram Monitoring System," *Sensors*, vol. 19, 1509, 2019.

[14] A. Dabbaghian, T. Yousefi, P. Shafia, S. Z. Fatmi, H. Kassiri, "A 9.2-Gram Fully-Flexible Wireless Dry-Electrode Headband for Non-Contact Artifact-Resilient EEG Monitoring and Programmable Diagnostics," *2019 IEEE International Symposium on Circuits and Systems (ISCAS)*, Sapporo, Japan, pp. 1–5, 2019.

[15] [Online]. Available: `https://neuralink.com`.

[16] Y. M. Chi, T. P. Jung, G. Cauwenberghs, " Dry-contact and noncontact biopotential electrodes: Methodological review," *IEEE reviews in biomedical engineering*, vol. 3, pp. 106–119, 2010.

[17] P. Richardson, "The insulated electrode: A pasteless electrocardiographic technique," *20th Annual conference on engineering in medicine and biology*, vol. 9, pp. 15–17, 1967.

[18] S. Dong, et al., "Doppler Cardiogram: A Remote Detection of Human Heart Activities," *IEEE Transactions on Microwave Theory and Techniques* vol. 68, no. 3, 1132–1141, 2020.

[19] E. Cardillo, A. Caddemi, "Radar range-breathing separation for the automatic detection of humans in cluttered environments," *IEEE Sensor Journal*, 1–1, 2020.

[20] E. Cardillo, A. Caddemi, "A. A review on biomedical MIMO radars for vital sign detection and human localization," *Electronics*, vol. 9, 1497, 2020.

[21] S. Schellenberger, K. Shi, F. Michler, F. Lurz, R. Weigel, A. Koelpin, "Continuous In-Bed Monitoring of Vital Signs Using a Multi Radar Setup for Freely Moving Patients," *Sensors*, vol. 20, 5827, 2020.

[22] F. Michler, et al., "A Radar-Based Vital Sign Sensing System for In-Bed Monitoring in Clinical Applications," *2020 German Microwave Conference (GeMiC)*, Cottbus, Germany, pp. 188–191, 2020.

[23] W. Taylor, Q. H. Abbasi, K. Dashtipour, S. Ansari, S. A. Shah, A. Khalid, M.A. Imran, "A Review of the State of the Art in Non-Contact Sensing for COVID-19," *Sensors* vol. 20, 5665, 2020.

[24] S. Ha, C. Kim, Y. M. Chi, A. Akinin, C. Maier, A. Ueno, G. Cauwenberghs, "Integrated Circuits and Electrode Interfaces for Noninvasive Physiological Monitoring," *IEEE Transactions on Biomedical Engineering*, vol. 61, No. 5, pp. 1522–1537, 2014.

[25] M. Noro, D. Anzai, J. Wang, "Common-mode noise cancellation circuit for wearable ECG," *Healthcare Technology Letters*, vol. 4, no. 2, pp.64–67, 2017.

[26] [Online]. Available: `https://www.murata.com/~/media/webrenewal/products/emc/emifil/knowhow/26to30.ashx`.

[27] Y. Jiang, O. W. Samuel, X. Liu, X. Wang, P. O. Idowu, P. Li, F. Chen, M. Zhu, Y. Geng, F. Wu, S. Chen, G. Li, "Effective biopotential signal acquisition: comparison of different shielded drive technologies," *Applied Sciences*, vol. 8, no. 2, 276, 2018.

[28] W. Liao, J. Shi, J. Wang, "Electromagnetic interference of wireless power transfer system on wearable electrocardiogram," *IET Microwaves Antennas & Propagation*, vol. 11, no. 3, pp. 330–335, 2017.

[29] M. Chen, D. Anzai, J. Wang, T. Terado, G. Fischer, "Two Improving Methods of EOG-based Eye Movement Detection for HCI," *IEEJ Transactions on Electronics, Information and Systems (C)*, vol. 139, No. 12, pp. 1474–1480, Dec. 2019.

[30] H. Collewijn, A. J. Martins, R. M. Steinman, "Compensatory eye movements during active and passive head movements: fast adaptation to changes in visual magnification," *The Journal of physiology*, vol. 340, no. 1, pp. 259–286, 1983.

[31] A. Serteyn, R. Vullings, M. Meftah, J. M. Bergmans, "Motion Artifacts in Capacitive ECG Measurements: Reducing the Combined Effect of DC Voltages and Capacitance Changes Using an Injection Signal," *IEEE Transactions on Biomedical Engineering*, vol. 62, No. 1, pp. 264–273, 2015.

[32] J. Webster, "Interference And Motion Artifact In Biopotentials," *in Proc. IEEE Region 6th Conf. Rec.*, pp. 53–64, May 1977.

[33] A. Qayoom, W. Abdul, "Artifact Processing of Epileptic EEG Signals: An Overview of Different Types of Artifacts," *2013 International Conference on Advanced Computer Science Applications and Technologies*, IEEE, pp. 358–361, 2013.

[34] S. L. Kappel, M. L. Rank, H. O. Toft, M. Andersen, P. Kidmose, "Dry-Contact Electrode Ear-EEG," *IEEE Transactions on Biomedical Engineering*, vol. 66, No. 1, pp. 150–158, January 2019.

[35] S. Khatun, R. Mahajan, B. I. Morshed, "Comparative Study of Wavelet-Based Unsupervised Ocular Artifact Removal Techniques for Single-Channel EEG Data," *IEEE journal of translational engineering in health and medicine*, vol. 4, pp. 1–8, April 2016.

[36] J. Sakuma, D. Anzai, J. Wang, "Performance of human body communication-based wearable ECG with capacitive coupling electrodes," *Healthcare technology letters*, vol. 3, No. 3, pp. 222–225, 2016.

[37] Z. Lv, X. Wu, M. Li, and C. Zhang, "Implementation of the EOG-based human computer interface system," *in Proceedings of the 2nd International Conference on Bioinformatics and Biomedical Engineering (ICBBE'08)*, Shanghai, China, pp. 2188–2191, May 2008.

[38] R. Barea, L. Boquete, M. Mazo, and E. Lopez, "Wheelchair guidance strategies using EOG," *Journal of Intelligent & Robotic Systems*, vol. 34, no. 3, pp. 279–299, 2002.

[39] S. Venkataramanan, P. Prabhat, S. R. Choudhury, H. B. Nemade, and J. S. Sahambi, "Biomedical instrumentation based on EOG signal processing and application to a hospital alarm system," *in Proc. IEEE ICISIP*, Chennai, India, pp. 535–540, 2005.

[40] R. Nopsuwanchai, Y. Noguchi, M. Ohsuga, Y. Kamakura, and Y. Inoue, "Driver-independent assessment of arousal states from video sequences based on the classification of eyeblink patterns," *Intelligent Transportation Systems, 2008. ITSC 2008. 11th International IEEE Conference on*, IEEE, pp. 917–924, 2008.

[41] A. Bulling, J. A. Ward, H. Gellersen, G. Tröster, "Eye movement analysis for activity recognition using electrooculography," *IEEE transactions on pattern analysis and machine intelligence*, vol. 33, no. 4, pp. 741–753, 2011.

[42] M. Brown, M. Marmor, Vaegan, E. Zrenner, M. Brigell, M. Bach, "ISCEV Standard for Clinical Electro-oculography (EOG) 2006," *Documenta ophthalmologica*, vol. 113, no. 3, pp. 205–212.

[43] T. Haslwanter, A. H. Clarke, "Eye movement measurement: electro-oculography and video-oculography," *Handbook of Clinical Neurophysiology*, vol. 9, pp. 61–79, 2010.

[44] R. J. McPartland, D. J. Kupfer, "Computerised measures of electro-oculographic activity during sleep," *International journal of bio-medical computing*, vol. 9, no. 6, 1978.

[45] S. Puthusserypady, T. Ratnarajah, "Robust adaptive techniques for minimization of EOG artefacts from EEG signals," *Signal Processing*, vol. 86, no. 9, 2006.

[46] M. Toivanen, K. Pettersson, K. Lukander, "A probabilistic real-time algorithm for detecting blinks, saccades, and fixations from EOG data," *Journal of Eye Movement Research*, vol. 8, no. 2, 2005.

[47] F. Behrens, M. MacKeben, W. Schröder-Preikschat, "An improved algorithm for automatic detection of saccades in eye movement data and for calculating saccade parameters," *Behavior research methods*, vol. 42, no. 3, pp. 701–708, 2010.

[48] M. Vidal, A. Bulling, H. Gellersen, "Analysing EOG signal features for the discrimination of eye movements with wearable devices," *Proceedings of the 1st international workshop on pervasive eye tracking & mobile eye-based interaction*, ACM, pp. 15–20, 2011.

[49] K. Pettersson, S. Jagadeesan, K. Lukander, A. Henelius, E. Hæggström, K. Müller, "Algorithm for automatic analysis of electro-oculographic data," *Biomedical engineering online*, vol. 12, no. 1, pp. 110, 2013.

[50] E. Ianez, J. M. Azorin, C. Perez-Vidal, "Using Eye Movement to Control a Computer: A Design for a Lightweight Electro-Oculogram Electrode Array and Computer Interface," *PloS one*, vol. 8, no. 7, e67099, 2013.

[51] M. I. Posner, "Orienting of attention," *Quarterly journal of experimental psychology*, vol. 32, no. 1, pp. 3–25, 1980.

[52] B. Quinlivan, J. S. Butler, I. Beiser, L. Williams, E. McGovern, S. O'Riordan, R. B. Reilly, "Application of virtual reality head mounted display for investigation of movement: a novel effect of orientation of attention," *Journal of neural engineering*, vol. 13, no. 5, 056006, 2016.

[53] T. Degen and T. Loeliger, "An improved method to continuously monitor the electrode-skin impedance during bioelectric measurements," 29th Annual International Conference of the IEEE Engineering in Medicine and Biology Society, pp. 6294–6297, 2007.

[54] H. de Talhouet and G. Webster, J., "The origin of skin-stretch-caused motion artifacts under electrodes," in Physiological Measurement, May 1996.

[55] B. B. Winter, J. G. Webster, "Driven-right-leg circuit design," *IEEE Transactions on Biomedical Engineering*, vol. BME-30, no. 1, pp. 62–66, 1983.

[56] K. K. Kim, Y. K. Lim, K. S. Park, "Common Mode Noise Cancellation for Electrically Non-Contact ECG Measurement System on a Chair," *Proceeding of the IEEE 27th Annual Conference in Medicine and Biology*, Shanghai, China, 2005.

[57] T. Degen, H. Jäckel, "Enhancing interference rejection of preamplified electrodes by automated gain adaption," *IEEE transactions on biomedical engineering*, vol. 51, no. 11, pp. 2031–2039, 2004.

[58] Y. M. Chi, , "Ultra-High Input Impedance, Low Noise Integrated Amplifier for Noncontact Biopotential Sensing," *IEEE Journal on Emerging and Selected Topics in Circuits and Systems*, vol. 11, no. 3, pp. 330–335, 2017.

[59] [Online]. Available: `https://wispry.com/solutions/tunable-digital-capacitor-arrays/`.

[60] [Online]. Available: https://www.st.com/zh/emi-filtering-and-signal-conditioning/stptic-82c4.html.

[61] [Online]. Available: https://www.psemi.com/pdf/datasheets/pe64102ds.pdf.

[62] M. Chen, J. Wang, D. Anzai, G. Fischer, "Common-mode Noise Reduction Circuit Design for Biosignal Acquisition System–in Comparison with the DRL," *IEEJ Transactions on Fundamentals and Materials (A)*, Vol. 139, No. 12, pp. 657–662, Dec. 2019.

[63] A. Serteyn, R. Vullings, M. Meftah, J. M. Bergmans, "Motion Artifacts in Capacitive ECG Measurements: Reducing the Combined Effect of DC Voltages and Capacitance Changes Using an Injection Signal," *IEEE Transactions on Biomedical Engineering*, vol. 62, No. 1, pp. 264–273, 2015.

[64] J. S. Turner, "New directions in communications," *IEEE J. Sel. Areas Commun.*, vol. 13, no. 1, pp. 11–23, Jan. 1995.

[65] M. S. Spach, R. C. Barr, J. W. Havstad, and E. C. Long, "Skin-electrode impedance and its effect on recording cardiac potentials", Circulation, vol. 34, no. 4, pp. 649–656, 1966.

[66] P. Marchionni1, L. Scalise2, L. Antognoli1, S. Nobile1, VP. Carnielli1, "Non-contact procedure to measure heart and lungs activities in preterm pediatric patients with skin disorders," *Laser Florence 2017: Advances in Laser Medicine*, International Society for Optics and Photonics, vol. 10582, 105820F, 2017.

[67] L. Xing, J. Sun, "Conducted Common-Mode EMI Reduction by Impedance Balancing," *IEEE Transactions on Power Electronics*, vol.27, no.3, pp. 1084–1089, 2011.

[68] J. Kirchner, N. Roth, A. Meyer, G. Fischer, "ECG measurement by use of passive capacitively coupled electrodes," *2016 IEEE SENSORS*, IEEE, pp. 1–3, 2016.

[69] Bauer B, "Design Notes on the Resistance-Capacity Oscillator Circuit," *Parts I and II, Hewlett-Packard Journal*, Hewlett-Packard, November, 1949.

[70] M. Chen, I. D. Castro, Q. Lin, T. Torfs, F. Tavernier, C. V. Hoof, N. V. Helleputte, "A 400G Ω input-impedance, 220mVpp linear-input-range, 2.8Vpp CM-interference-tolerant active electrode for non-contact capacitively coupled ECG acquisition," *2018 IEEE Symposium on VLSI Circuits*, IEEE, pp. 129–130, 2018.

[71] W. H. Ko, "Active electrodes for EEG and evoked potential," *Proceedings of the 20th Annual International Conference of the IEEE Engineering in Medicine and Biology Society. Vol. 20 Biomedical Engineering Towards the Year 2000 and Beyond (Cat. No. 98CH36286)*, IEEE, vol. 4, pp. 2221–2224, 1998.

[72] M. Seo, J. S. Lee, S. W. Kim, et al., "Adaptive Noise Reduction of Multichannel Signals Obtained by Capacitive ECG Sensors," *2018 4th International Conference on Frontiers of Signal Processing (ICFSP)*. IEEE, pp. 39–43, 2018.

[73] T. Degen, S. Torrent, H. Jäckel, "Low-noise two-wired buffer electrodes for bioelectric amplifiers", *IEEE transactions on biomedical engineering*, vol. 54, no.7, pp. 1328–1332, 2007.

[74] M. Takano, A. Ueno, "Noncontact in-bed measurements of physiological and behavioral signals using an integrated fabric-sheet sensing scheme," *IEEE journal of biomedical and health informatics*, vol. 23, no.2, pp. 618–630, 2018.

[75] E. Jedari, R. Rashidzadeh, M. Mirhassani, et al., "Two-electrode ECG measurement circuit using a feed forward CMRR enhancement method," *2017 IEEE 30th Canadian Conference on Electrical and Computer Engineering*, IEEE, pp. 1–4, 2017.

[76] M. Metshein, "A device for measuring the electrical bioimpedance with variety of electrode placements for monitoring the breathing and heart rate," *2015 26th Irish Signals and Systems Conference*, IEEE, pp. 1–4, 2015.

[77] O. D. Lara, M. A. Labrador, "A survey on human activity recognition using wearable sensors," *IEEE communications surveys & tutorials*, vol. 15, no.3, pp. 1192–1209, 2012.

[78] Y. Zheng, X. Ding, C. Poon, et al. "Unobtrusive sensing and wearable devices for health informatics," *IEEE Transactions on Biomedical Engineering*, vol. 61 no. 5, pp. 1538–1554, 2014.

Acknowledgements

My heartfelt appreciation goes to Prof. Wang whose comments and suggestions were of inestimable value for my study. I am also indebt to Associate Prof. Anzai whose comments made enormous contribution to my work. I would also like to express my gratitude to the students in my laboratory and my family for their moral support and warm encouragement.

Besides, I would like to thank Prof. Kikuma Prof. Hirata and Prof. Xiao, for their insightful comments and heartful encouragements that inspired me to widen my research from various perspectives.

Many thanks to Prof. Georg Fischer, Dr. Jens Kirchner, and Friedrich-Alexander University of Erlangen-Nuremberg for their kind support during my research stay in Erlangen.

This study was supported in part by JSPS KAKENHI Grant Number 19H02139. The authors also gratefully acknowledge financial support for this work by the Deutsche Forschungsgemeinschaft under GRK2495/A.

Chapter 7

Publication lists

7.1 Paper

[1] M. Chen, D. Anzai, J. Wang, T. Terado, G. Fischer,"Two Improving Methods of EOG-based Eye Movement Detection for HCI," *IEEJ Transactions on Electronics, Information and Systems (C)*, vol. 139, No. 12, pp. 1474–1480, Dec. 2019.

[2] M. Chen, J. Wang, D. Anzai, G. Fischer, "Common-mode Noise Reduction Circuit Design for Biosignal Acquisition System–in Comparison with the DRL," *IEEJ Transactions on Fundamentals and Materials (A)*, Vol. 139, No. 12, pp. 657–662, Dec. 2019.

[3] Chen, M.; Wang, J.; Anzai, D.; Fischer, G.; Kirchner, J. Common-Mode Noise Reduction in Noncontact Biopotential Acquisition Circuit Based on Imbalance Cancellation of Electrode-Body Impedance. *Sensors* **2020**, *20*, 7140.

7.2 International Conference

[1] M. Chen, D. Anzai, J. Wang, G. Fischer, "Circuit Design for Common-mode Noise Rejection in Biosignal Acquisition based on Imbalance Cancellation of Electrode Contact Resistance," *EMC Sapporo and APEMC 2019*, Sapporo, Japan,

June 2019.

7.3 Oral Presentation

[1] M. Chen, D. Anzai, J. Wang, T. Terado, "Development of Input System Conctrolled by Vision Movement Using EOG and Study on Improving Method of Eye Movements Detection," *The 12th Annual Meeting of the Japan Association of IT Healthcare*, Kawasaki, Japan, June 2018.

[2] M. Chen, D. Anzai, J. Wang, G. Fischer, J. Kirchner, "A Study on Common-mode Noise Reduction in Noncontact Biosignal Acquisition Circuit," *EMCJ2019-11*, pp. 55–59, 2019.